

COO-3072-14

Princeton University
Elementary Particles Laboratory
Department of Physics

NEUTRON PROTON CHARGE EXCHANGE

SCATTERING FROM 8 TO 29 GEV/C

MICHAEL BRUCE DAVIS

TECHNICAL REPORT NO. 4

September 1972

Contract AT(11-1)-3072

NOTICE

This report was prepared as an account of work sponsored by the United States Government. Neither the United States nor the United States Atomic Energy Commission, nor any of their employees, nor any of their contractors, subcontractors, or their employees, makes any warranty, express or implied, or assumes any legal liability or responsibility for the accuracy, completeness or usefulness of any information, apparatus, product or process disclosed, or represents that its use would not infringe privately owned rights.

DISTRIBUTION OF THIS DOCUMENT IS UNLIMITED

leg

NEUTRON PROTON CHARGE EXCHANGE
SCATTERING FROM 8 TO 29 GEV/C

Michael Bruce Davis

A DISSERTATION
PRESENTED TO THE
FACULTY OF PRINCETON UNIVERSITY
IN CANDIDACY FOR THE DEGREE
OF DOCTOR OF PHILOSOPHY
RECOMMENDED FOR ACCEPTANCE BY THE
DEPARTMENT OF
PHYSICS

August, 1972

ABSTRACT

The differential cross sections for neutron proton charge exchange scattering were measured for incident neutron momenta between 8 and 29 GeV/c and for four-momentum transfers $|t|$ between 0.002 and 1.0 (GeV/c)². A neutron beam with a broad momentum spectrum was scattered from a liquid hydrogen target. The momenta and scattering angles of the forward-scattered protons were measured by a spark-chamber magnet spectrometer. The times of flight and scattering angles of the recoil neutrons were measured by a bank of thick scintillation counters. The efficiencies of the neutron counters were determined in a separate measurement. Absolute normalization of the data was obtained from a measurement of the diffraction dissociation of neutrons from carbon nuclei. Differential cross sections, based on ~ 23,000 events, are presented for 9 different momenta. The shape of the differential cross sections and the momentum dependence are examined in detail.

ACKNOWLEDGEMENTS

I would like to thank my advisor, Dr. Michael Kreisler, for his help and encouragement during all stages of this experiment and during the various crises in my life at Princeton and at Brookhaven. I also thank Dr. Longo of the University of Michigan for his guidance during the planning, setting-up, and data-taking phases of the experiment.

My special thanks go to Don O'Brien, who worked long hours on the experiment and who provided information on the neutron spectrum. My special thanks also go to Tom McCorriston, who wrote many of the on-line computer programs and who helped with the measurement of the total beam flux.

I thank Bruce Gibbard for his help in running the experiment, Tad Dobrowolski for many stimulating conversations, and Tim Toohig for his assistance in obtaining on-line computer facilities for the experiment.

I would like to thank the AGS staff for their assistance, especially Jack Detwiler, the liason engineer for this experiment. I would also like to thank Fred Schwarz, Bart Gibbs, and the many other people at Princeton, Michigan, and Brookhaven who helped build the equipment for this experiment. I thank the many people from Princeton and Michigan who helped to set up and run the experiment. I also thank Victor Bearg for his help in writing and debugging the analysis programs.

Finally, I would like to thank my parents for their support and encouragement throughout my undergraduate and graduate education.

TABLE OF CONTENTS

ABSTRACT	i
ACKNOWLEDGEMENTS	ii
LIST OF TABLES	v
LIST OF FIGURES	vi
CHAPTER I. INTRODUCTION	1
CHAPTER II. SUMMARY OF PREVIOUS EXPERIMENTAL AND THEORETICAL WORK	3
A. Experimental Data on n-p Charge Exchange	3
B. Theoretical Work	6
CHAPTER III. EXPERIMENTAL SET-UP	16
A. Beam Line	16
B. Liquid Hydrogen Target and Anticounters	19
C. Proton Arm	22
D. Neutron Arm	26
E. Electronics	33
CHAPTER IV. DATA TAKING AND ON-LINE ANALYSIS	40
A. Data Taking Procedure	40
B. On-Line Analysis	42
CHAPTER V. DATA ANALYSIS	44
A. Track Reconstruction	44
B. Kinematic Reconstruction and Selection of Elastics	53
C. Monte Carlo	66
D. Normalization	67

CHAPTER VI. PRESENTATION OF RESULTS	69
A. Cross Sections and Errors	69
B. Energy Dependence of the Cross Sections	89
C. Comparison with Models	95
D. Final Remarks	95
APPENDIX A. KINEMATICS	98
APPENDIX B. NEUTRON COUNTER EFFICIENCY MEASUREMENTS	103
APPENDIX C. MEASUREMENT OF TOTAL BEAM FLUX	109
APPENDIX D. MEASUREMENT OF INCIDENT NEUTRON MOMENTUM	
SPECTRUM	115
REFERENCES	124

LIST OF TABLES

Table	Page
3.1 Angular, energy, and TOF ranges for the neutron counters	29
4.1 Amount of data taken	41
5.1 Number of events eliminated by the cuts	48
6.1 np→pn differential cross section, 8 - 11 GeV/c	79
6.2 np→pn differential cross section, 11 - 14 GeV/c	80
6.3 np→pn differential cross section, 14 - 16 GeV/c	81
6.4 np→pn differential cross section, 16 - 18 GeV/c	82
6.5 np→pn differential cross section, 18 - 20 GeV/c	83
6.6 np→pn differential cross section, 20 - 22 GeV/c	84
6.7 np→pn differential cross section, 22 - 24 GeV/c	85
6.8 np→pn differential cross section, 24 - 26 GeV/c	86
6.9 np→pn differential cross section, 26 - 29 GeV/c	87

LIST OF FIGURES

Figure	Page
2.1 Meson exchange diagram	8
2.2 Helicity amplitudes	8
3.1 Beam line	17
3.2 Liquid hydrogen target	20
3.3 Experimental layout	21
3.4 Neutron counter	27
3.5 Measurement of pulse heights from neutron counter dynodes	30
3.6 Light pulser system	32
3.7 Simplified logic diagram	34
3.8 Digital electronics and computer interface	37
5.1 Coordinate system	46
5.2 Spark chamber inefficiencies for a typical pair of chambers	50
5.3 Comparison of the measured front and rear proton trajectories (magnet off)	52
5.4 $\Delta\theta$, $\Delta\phi$, ΔTOF distributions before cuts	57
5.5 $\Delta\theta$, $\Delta\phi$, ΔTOF distributions after cuts	58
5.6 Background determination for a typical counter	59
5.7 Background versus t	60
5.8 Up minus down digitime reading versus pulse area (for light pulser runs)	62
5.9 ΔTOF versus pulse area	64

Figure	Page
6.1 np→pn differential cross section, 8 - 11 GeV/c	70
6.2 np→pn differential cross section, 11 - 14 GeV/c	71
6.3 np→pn differential cross section, 14 - 16 GeV/c	72
6.4 np→pn differential cross section, 16 - 18 GeV/c	73
6.5 np→pn differential cross section, 18 - 20 GeV/c	74
6.6 np→pn differential cross section, 20 - 22 GeV/c	75
6.7 np→pn differential cross section, 22 - 24 GeV/c	76
6.8 np→pn differential cross section, 24 - 26 GeV/c	77
6.9 np→pn differential cross section, 26 - 29 GeV/c	78
6.10 Two exponential fit to two typical cross sections . . .	90
6.11 Parameters from the two exponential fit	91
6.12 Momentum dependence of $d\sigma/dt(t=0)$	92
6.13 Momentum dependence of $d\sigma/dt$ at $-t=0.05$ (GeV/c) ² and $-t=0.2$ (GeV/c) ²	93
6.14 n versus t, where $(d\sigma/dt)_{t=\text{const.}} \propto p_{\text{lab}}^{-n}$	94
6.15 Comparison of a typical cross section with two models .	96
A.1 Kinematics variables	99
B.1 Experimental set-up for neutron counter efficiency measurements	104
B.2 Efficiency of N ₁	105
B.3 Efficiency of N ₂	106
B.4 Efficiency of N ₃	107
B.5 Efficiency of N ₄ through N ₁₅	108
C.1 Total absorption spectrometer	110

Figure	Page
C.2 Experimental set-up for integral beam flux measurement	112
C.3 Monitor counts per pulse extrapolated to zero rate . .	113
D.1 Possible mechanism for diffraction dissociation of neutrons off carbon nuclei	116
D.2 Experimental set-up for diffraction dissociation measurement	118
D.3 t' distribution of diffraction dissociation events . .	120
D.4 $p\pi^-$ mass distribution	121
D.5 Neutron spectrum	123

CHAPTER I. INTRODUCTION

This paper describes an experiment done at the Brookhaven Alternating Gradient Synchrotron to measure the differential cross section for neutron proton charge exchange scattering,

$$n + p \rightarrow p + n ,$$

for incident neutron momenta between 8 and 29 GeV/c. Previous experiments⁽¹⁻³⁾ indicated that there was a forward peak* in the angular distributions which was much sharper than the peak in p-p scattering. This peak appeared in data with energies ranging from below the one-pion threshold up to the highest energies studied.† The distributions in t, the square of the four-momentum transfer between the incoming neutron and the outgoing proton, appeared to be essentially independent of energy, and the forward cross section decreased with increasing energy. (See Appendix A for definitions of the kinematic quantities.) The general shape of the differential cross sections could be described by⁽²⁾

$$d\sigma/dt = A e^{-B|t|} + C e^{-D|t|} ,$$

where $B \approx 50 \text{ (GeV/c)}^{-2}$, $D \approx 4 \text{ (GeV/c)}^{-2}$, and $A \approx C$.‡ B, the slope of the forward peak, was approximately equal to $1/m_\pi^2$ (m_π = mass of pion), implying that the forward peak was due to one pion exchange. However, a simple one pion exchange model predicts a dip at $t = 0$ rather than a peak. In order to explain the peak, more complicated models were suggested (see Chapter II-B). To check the predictions of these models, data at higher energy and larger values of $|t|$ became necessary.

* "Forward" n-p charge exchange scattering is equivalent to n-p elastic scattering at 180° in the center of mass.

† At the time this experiment was first proposed (1967), the only data above 2 GeV/c was that of Palevsky et al. (1,2) near 3 GeV/c and that of Manning et al. (3) at 8 GeV/c.

‡ The data of Mischke et al. (7) (0.6 to 2.0 GeV/c), which appeared about the time this experiment was being set up (1969) indicated, however, that perhaps there was an energy dependence of the shape of the differential cross sections.

This experiment was part of a general program to study neutron interactions at high energies⁽⁴⁾. The objectives of the present experiment were the following:

- (a) To study the energy dependence of the shape of the differential cross section for n-p charge exchange scattering; in particular, to determine whether or not there was "shrinkage" of the forward peak (see Chapter II-B).
- (b) To study the energy dependence of the absolute cross sections by taking measurements over a wide energy range at one time. Previous measurements⁽¹⁻³⁾ had indicated that the cross sections decreased with increasing incident neutron momentum as p_{lab}^{-2} to p_{lab}^{-3} . These measurements, taken over a wide energy range with consistent normalization, would give accurate information on the energy dependence of the absolute cross sections.
- (c) To extend measurements to larger four-momentum transfers and higher energies than previous experiments.

The method used in this experiment was as follows. A beam containing neutrons with momenta between 6 and 29 GeV/c struck a liquid hydrogen target. The momenta and scattering angles of the forward-scattered protons were measured in a wire-spark-chamber spectrometer. The recoil neutrons were detected by a bank of scintillation counters, and their times of flight and scattering angles were measured. By comparing the information from the two arms of the experiment, it was possible to determine which events were elastic and which were inelastic. The neutron flux was measured by another experiment in the same beam line.

Chapter II gives a summary of recent experimental and theoretical work in n-p charge exchange scattering. Chapter III describes the experimental apparatus. Chapter IV discusses the data-taking process and the preliminary on-line analysis. Chapter V describes the analysis of the data. Chapter VI presents the cross sections and compares them with theoretical predictions.

CHAPTER II. SUMMARY OF EXPERIMENTAL AND THEORETICAL WORK

The first part of this chapter summarizes the results of other neutron proton charge exchange experiments. The second part briefly discusses some of the theoretical models which have attempted to explain the shape and energy dependence of the cross sections.

A. Experimental Data on n-p Charge Exchange

Neutron proton charge exchange differential cross sections have been measured at high energies using the following three experimental methods.

- (a) In the double charge exchange method, a neutron is produced in a light metal target by elastic p-n charge exchange, and the neutron in turn undergoes an elastic n-p charge exchange scattering in a liquid hydrogen target. The final proton is detected and is required to have the full beam energy, ensuring that two successive charge exchange reactions have taken place. The final neutron is not detected. This method is sensitive to the angular distributions near $t = 0$. However, extremely good momentum resolution is necessary to separate the protons which have undergone double charge exchange scattering from those which are inelastically produced. Small angle scattering of the neutron or the proton in the hydrogen target, the spread in the momentum of the proton beam, and other such sources of momentum uncertainty lead to difficulties in eliminating backgrounds. In order to normalize the cross sections obtained by this method it is necessary to know the effective number of free neutrons contributing to the p-n charge exchange reaction in the primary target. This number is difficult to determine accurately.
- (b) In another method, a neutron beam with a broad momentum spectrum is used. The energies of the incident neutrons are determined from their times of flight, and the momenta

of the forward-scattered protons are measured. With this method it is not necessary to require double charge exchange; momentum resolution is therefore less critical than in the first method. A disadvantage of this technique is that it can be used only at low energies where the neutron energy can be determined from the time of flight, and only at accelerators such as the Princeton Pennsylvania Accelerator where good time of flight resolution is possible.

- (c) In a third method (the one used by this experiment), the momentum vectors of both particles in the final state are measured. Inelastic events are easily separated from elastics because the kinematics of each event is overdetermined. Since the incident neutron momentum can be calculated for the elastic events, a beam with a broad momentum spectrum can be used. In order to normalize the cross sections, this spectrum must be independently determined. A disadvantage of this method is that the efficiencies of the neutron counters must be determined. Because the efficiencies are low at neutron kinetic energies below 1 MeV, it is difficult to measure the differential cross sections for $-t < .002 \text{ (GeV/c)}^2$.

The first measurements of neutron proton charge exchange scattering above 2 GeV were made in 1962. Using the first method above (double charge exchange), Palevsky et al.⁽¹⁾ measured the cross section for n-p charge exchange scattering at kinetic energies of 2.04 and 2.85 GeV. The velocity of the final proton was measured in a threshold gas Čerenkov counter. Palevsky found that the distributions in transverse momentum $p_{\perp} = p_0 \sin\theta$ were the same for both energies; that the distributions were sharply peaked at zero momentum transfer, falling to half maximum at $p_{\perp} = 150 \text{ MeV/c}$; and that the forward cross sections were an order of magnitude smaller than the forward p-p cross sections.

In 1965, using the same technique, the same group⁽²⁾ measured

the differential cross sections at 3 GeV/c and the zero degree cross sections at 1.40, 2.35, and 2.55 GeV/c. They compared the shapes of their cross sections with the data of Larsen⁽¹²⁾ at 1.37 GeV/c and the preliminary data of Manning et al.⁽³⁾ at 8.15 GeV/c. The shapes appeared to be the same for all energies studied, with slight evidence for a narrowing of the peak at the higher energies. It was found that the angular distributions at 3 GeV/c could be fit rather well by the two-exponential form

$$d\sigma/dt \text{ [mb/(GeV/c)}^2\text{]} = 6.9 e^{-49|t|} + 4.1 e^{-4|t|} .$$

The logarithmic slope at small $|t|$, 49 (GeV/c)^{-2} , was much larger than that for p-p scattering ($\sim 7 \text{ (GeV/c)}^{-2}$) or \bar{p} -p scattering ($\sim 15 \text{ (GeV/c)}^{-2}$). At larger $|t|$, the cross sections decreased exponentially with a slope of approximately 4 (GeV/c)^{-2} . The $t = 0$ absolute cross sections (including the data of Larsen and the preliminary data from Manning et al.) were found to decrease with increasing incident momentum approximately as p_{lab}^2 . The data of Manning et al., however, seemed to indicate that the cross sections might be decreasing as rapidly as p_{lab}^{-3} .

In 1965, Wilson⁽⁵⁾ pointed out that the sharp forward peak observed by Palevsky et al. was also a feature of lower energy cross sections. He examined the t dependence of n-p charge exchange cross sections at energies from 91 MeV to 2.85 GeV and concluded that the momentum transfer distributions were essentially the same for all energies.

In 1966 Manning et al.⁽³⁾ published the results of a measurement of the n-p charge exchange cross section at 8 GeV/c, using the double charge exchange method. The proton momentum was measured in a spark chamber spectrometer system. Comparing their results with those at lower energies, they found that for small $|t|$, the shape of the cross sections seemed to be independent of energy. For $-t > 0.1 \text{ (GeV/c)}^2$, however, the ratio $[(d\sigma/dt)/(d\sigma/dt)_{t=0}]$ at constant t seemed to decrease with increasing energy. They also found that the $t = 0$ cross section continued to decrease rapidly with

increasing energy.

In 1969, Mischke et al.^(6,7) measured n-p charge exchange cross sections between 0.6 and 2.0 GeV/c, using the second of the three methods described above. The cross sections $d\sigma/dt$ showed a sharp change in slope around $-t = .01 (\text{GeV}/c)^2$. Near $t = 0$ the logarithmic slopes varied from approximately $100 (\text{GeV}/c)^{-2}$ at the lowest energies to approximately $30 (\text{GeV}/c)^{-2}$ at the highest energy, a more complicated behavior than had been previously observed. At larger values of $|t|$ ($> 0.02 (\text{GeV}/c)^2$), the slope was approximately $6.5 (\text{GeV}/c)^{-2}$, independent of energy.

In 1971, Miller et al.⁽⁸⁾ measured n-p charge exchange cross sections from 3 to 12 GeV/c, using the third method described above. They found that there was a sharp forward peak in the differential cross sections with a slope of approximately $50 (\text{GeV}/c)^{-2}$ and that there was a slower exponential fall-off at larger $|t|$ with a slope of approximately $5 (\text{GeV}/c)^{-2}$. The shapes of the cross sections were essentially energy independent. The $t = 0$ cross sections decreased with increasing energy as $p_{\text{lab}}^{-2.1}$.

In the same year, Engler et al.⁽⁹⁾ made measurements of n-p charge exchange differential cross sections at 8, 19.2, and 24 GeV/c, using the double charge exchange method. They found that the forward peak in the cross section persisted to 24 GeV/c and that the t dependence of the cross section did not change appreciably with energy. They also found that the $t = 0$ cross sections had an energy dependence consistent with p_{lab}^{-2} .

B. Theoretical Work

The observation of a sharp forward peak in n-p charge exchange cross sections, with a width approximately equal to m_{π}^2 , has led to many attempts to explain the peak in terms of a pion pole. In 1958 Chew⁽¹⁰⁾ pointed out that the real part of the n-p scattering amplitude should have a pole in the nonphysical region at $t = m_{\pi}^{2*}$. He

* In the physical region, $t \leq 0$. See Appendix A for definitions of the kinematic quantities.

suggested that the data from n-p scattering experiments (backward or forward scattering) could be extrapolated to the pion pole to determine the pion-nucleon coupling constant. Several groups⁽¹¹⁻¹⁴⁾ performed this extrapolation at energies between 300 and 800 MeV and found values for the coupling constant which agreed with the values found from π -N scattering. This result established that one pion exchange contributed to n-p scattering at small angles⁽¹³⁾.

Despite the fact that the pion-nucleon coupling constant can be calculated from n-p scattering data, the shape of the n-p charge exchange cross sections cannot be explained by a simple one pion exchange model. The cross section obtained from one pion exchange in the first Born approximation is⁽¹⁵⁾

$$\frac{d\sigma}{dt} = \frac{\pi}{p^2 s} \left(\frac{g^2}{4\pi} \right)^2 \left(\frac{t}{t - m_\pi^2} \right)^2$$

where g is the pion-nucleon coupling constant, $(g^2/4\pi) \approx 14$. This cross section obviously goes to zero at $t = 0$.

Since the observed forward peak cannot be explained by one pion exchange alone, it is possible that other particles are exchanged. Figure 2.1 shows the reaction $n + p \rightarrow p + n$ with the exchange of a meson M . Possible candidates for M which satisfy the necessary conservation laws at both vertices are the $\pi(1,0,-)$, $\rho(1,1,-)$, and $A_2(1,2,+)$, where the numbers in parentheses give the isospin, spin, and parity respectively of each particle.

When discussing high energy exchange processes it is convenient to use the amplitudes for scattering in particular helicity states⁽¹⁶⁾. Since each of the four particles can have either positive or negative helicity, there are 16 helicity amplitudes, which can be represented by*

$$\varphi = \sum_f p(\pm) n(\pm) | n(\pm) p(\pm) \rangle_i$$

where the (\pm) refer to the helicities of the particles, and the i and f refer to the initial and final states. These 16 amplitudes

* This notation and Figure 2.2 are taken from references 19 and 33.

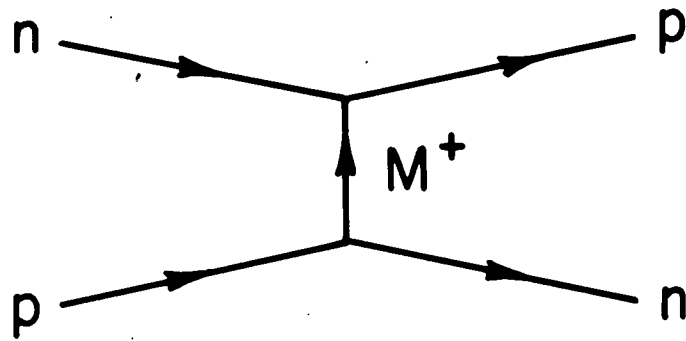
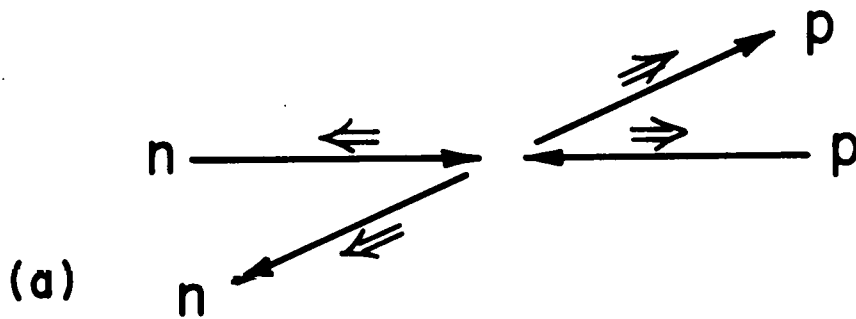


Figure 2.1

$$\phi_2 = \left\langle p(+)\ n(+)\ \left| \ n(-)\ p(-)\ \right. \right\rangle_i$$



$$\phi_4 = \left\langle p(+)\ n(-)\ \left| \ n(-)\ p(+)\ \right. \right\rangle_i$$

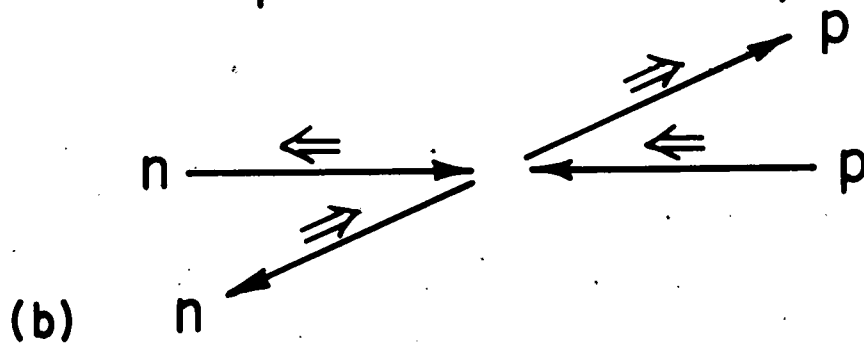


Figure 2.2

are not independent; their number can be reduced to 5 by applying the principles of parity conservation, time reversal invariance, and isotopic spin conservation⁽¹⁷⁾.

For one pion exchange, conservation of parity and angular momentum require that there be a spin flip at each vertex. Therefore only the two amplitudes

$$\varphi_2 = \int_{\mathbb{F}} p(+)\ n(+)\ | \ n(-)\ p(-)\rangle_{\mathbb{I}}$$

and

$$\varphi_4 = \int_{\mathbb{F}} p(+)\ n(-)\ | \ n(-)\ p(+)\rangle_{\mathbb{I}}$$

will be nonvanishing. Also, in the case of pion exchange, these two amplitudes are equal⁽¹⁸⁾. As can be seen in Figure 2.2*, the amplitude φ_4 involves a net helicity flip of 1 and must therefore vanish at $t = 0$, by conservation of angular momentum. Since $\varphi_2 = \varphi_4$, the entire π contribution must vanish at $t = 0$. The vanishing of the pion contribution at $t = 0$ can also be seen in the expression obtained for the scattering amplitudes for one pion exchange in the first Born approximation⁽¹⁵⁾:

$$\varphi_2 \sim \frac{1}{\sqrt{s}} \frac{t}{t - m_{\pi}^2} \quad (1)$$

Simple one pion exchange can therefore not explain the observed peak in the angular distributions at $t = 0$.

The above restrictions on the helicity amplitudes do not apply to mesons with nonzero spin. The ρ and A_2 can contribute to all 5 helicity amplitudes. However, since scattering near $t = 0$ corresponds to large impact parameters, it seems reasonable that small $|t|$ scattering should be dominated by the π , which is less massive than the ρ or A_2 and therefore has a longer range.

After the data of Palevsky et al.⁽¹⁾ at 3 GeV/c were published, there were several attempts to fit the data with simple π and ρ exchange models⁽²⁰⁻²²⁾. As discussed above, one pion exchange alone could not explain the shape of the cross sections, and it was

* This figure appears in references 19 and 33.

necessary to include other mechanisms. Bugg⁽²³⁾ gave a possible explanation for the peak in terms of the difference between diffraction scattering in the isotopic spin $T = 0$ and $T = 1$ channels. Phillips⁽²⁰⁾ showed that the sharp peak could be explained as the strong interference between a one pion exchange term and a slowly varying background from other processes (put in phenomenologically). Muzinich⁽²¹⁾ suggested the exchange of a Reggeized ρ . Islam and Preist⁽²²⁾ suggested the exchange of both ρ and π , where the sharp peak was due to a rapidly decreasing form factor for the ρ exchange. It was later shown⁽²⁴⁾, however, that ρ exchange alone could not explain simultaneously the energy dependence of the differential cross section $d\sigma/dt(t=0)$ and the magnitude of the cross section difference $\sigma_T(pp) - \sigma_T(np)^*$.

Some of the early papers^(20,13) had considered the interference of the pion pole term with the rest of the less rapidly varying scattering amplitude (chosen phenomenologically). Several theorists⁽²⁵⁻²⁷⁾ further developed this idea by including corrections for absorption effects caused by competing inelastic channels in the initial and final states. As Gottfried and Jackson⁽²⁸⁾ pointed out, competing inelastic channels would be most effective at small impact parameters (i.e., in low angular momentum states) and would there reduce the low partial wave amplitudes below the values given by the one particle exchange model, while leaving the higher partial wave amplitudes essentially unchanged. The result would be a reduction in the reaction cross section and collimation of the angular distributions in the forward direction.

Several theorists⁽²⁵⁻²⁷⁾ calculated simple π and ρ contributions to n-p charge exchange and then included corrections for absorption of each partial wave, based on the parameters found from p-p scattering. The one pion exchange model with absorption gave reasonable agreement with experiment for $-t < 0.01$ (GeV/c)² but predicted a secondary maxima in the cross sections which was not observed.

* Isospin dependence of N-N scattering, plus the optical theorem, gives $d\sigma/d\Omega(t=0) \geq (p/4\pi)^2 (\sigma_T(pp) - \sigma_T(np))^2$.

Another problem with absorption models was that they could not explain the fact that the forward peak persists to very low energies (below inelastic thresholds). However, it was pointed out⁽²⁹⁾ that perhaps the elastic unitarity requirement* modifies the lower partial waves at low energy in the same way that absorption does at high energy.

Another model combining one pion exchange with absorptive effects was the "coherent droplet" model of Byers and Yang⁽³¹⁾, which Byers applied to n-p charge exchange scattering. In this model, scattering in high angular momentum states (large impact parameters) was dominated by one pion exchange, while scattering at small impact parameters was pictured as the passage of one extended object through another, with resulting absorption. This model was able to fit the shapes of both $np \rightarrow pn$ and $\bar{p}p \rightarrow \bar{n}n$ cross sections.

There have been many attempts to explain the s and t dependence of the n-p charge exchange cross sections using Regge theory. The simple Regge model in which only one pole is exchanged has not been able to explain the t dependence of the cross sections. However, it is useful to consider the single Regge exchange model because it makes predictions about the energy dependence of the differential cross sections which are easily compared with measurements.

In the simple Regge model the amplitude for the exchange of a "Reggeized" pion can be written⁽³²⁾

$$\varphi_2 \propto \frac{1}{\sqrt{s}} \frac{t}{t-m_\pi^2} (1 + e^{-\pi\alpha(t)}) \left(\frac{s}{s_0}\right)^{\alpha(t)}, \quad (2)$$

where $\alpha(t)$ is the Regge trajectory, which has the value $\alpha(t=m^2) = J$ (m and J are the mass and spin of the exchanged particle, in this case a π). In the above equation, s_0 is a scale factor usually taken to be 1 GeV^2 ; $\alpha(t)$ can be parameterized as

$$\alpha(t) = \alpha(0) + \alpha' t \quad (3)$$

* This is essentially the requirement that the total rate of absorption in a state of given angular momentum cannot exceed the portion of the incident flux corresponding to that angular momentum⁽³⁰⁾.

where $\alpha' = d\alpha/dt(t=0)$ is approximately 1 (GeV/c)^{-2} . Approximate values of $\alpha(0)$ for π , ρ , and A_2 trajectories are 0, 0.5, and 0.5.

If we parameterize $\alpha(t)$ as in equation (3), equation (2) can be written

$$\varphi_2 \propto \frac{1}{\sqrt{s}} \frac{t}{t-m_\pi^2} (1 + e^{-i\pi\alpha(t)}) \left(\frac{s}{s_0}\right)^{\alpha(0)} e^{(\alpha' \ln(s/s_0))t}$$

This is essentially the one pion exchange term, equation (1), modulated by the exponential $e^{b(s)t}$, $b(s) = \alpha' \ln(s/s_0)$. Obviously this simple Regge model fails to predict the forward peak, since the amplitude vanishes at $t = 0$.

The differential cross section (at small $|t|$) for a process dominated by a single Regge exchange can be written⁽³³⁾

$$\frac{d\sigma}{dt} = F(t) \left(\frac{s}{s_0}\right)^{2\alpha(0)-2} e^{(2\alpha' \ln(s/s_0))t}$$

where $F(t)$ accounts for all the t dependence which is not included in the last term. This equation makes three predictions about the energy dependence of the cross section.

- (a) The last term predicts that the angular distributions will "shrink" (become more peaked in the forward direction) with increasing energy.
- (b) The second term predicts that at $t = 0$, the differential cross section will decrease with energy as s^{-2} if pion exchange ($\alpha(0) \approx 0$) dominates and as s^{-1} if ρ or A_2 exchange ($\alpha(0) \approx 0.5$) dominates.
- (c) The first term predicts that, apart from shrinkage, the t dependence (at small $|t|$) of the cross sections will be independent of energy.

The simple one Regge exchange model is successful in explaining the energy dependence of the n-p charge exchange cross sections, although present data indicates that there is no shrinkage. To explain the t dependence of the cross sections, however, more complicated models are necessary.

Before discussing more complicated models it is useful to list the features of n-p scattering data which, as Arbab and Dash⁽³⁴⁾ have pointed out, must be explained by any successful theory. These features are

- (a) the sharp peak in $np \rightarrow pn$, with width $\approx m_\pi^2$,
- (b) the fact that the peak persists to very low energies and is almost energy independent,
- (c) the large difference in the magnitudes of the cross sections for $np \rightarrow pn$ and for $\bar{p}p \rightarrow \bar{n}n$ at the same value of s and t (for $|t| > 0.02 \text{ (GeV/c)}^2$),
- (d) the energy dependence of the $\bar{p}p \rightarrow \bar{n}n$ data.

Parts (c) and (d) are important because the reactions $np \rightarrow pn$ and $\bar{p}p \rightarrow \bar{n}n$ are related by crossing symmetry and must be described by the same amplitude (see Appendix A). In addition to these items, the predictions of a successful theory must be consistent with the requirement $d\sigma/d\Omega(t=0) \geq (p/4\pi)^2 (\sigma_T(pp) - \sigma_T(np))^2$.

Because the pion contribution vanishes at $t = 0$, early Regge models did not include the pion trajectory. Using the ρ and A_2 trajectories, Ahmadzadeh⁽³⁵⁾ was able to explain simultaneously the energy dependence of $d\sigma/d\Omega(t=0)$ and the magnitude of $\sigma_T(pp) - \sigma_T(np)$; he made no attempt to determine the t dependence of the cross sections. Flores-Maldonado⁽³⁶⁾, using these same two trajectories, was able to fit the differential cross sections for $np \rightarrow pn$ and for $\bar{p}n \rightarrow n\bar{p}$ but was not able to satisfactorily explain requirement (c) above. There were several objections to models which did not include the pion trajectory. Arbab and Dash⁽³⁴⁾ pointed out, for example, that the small observed values of $\sigma_T(pp) - \sigma_T(np)$ are consistent with small contributions from the ρ and A_2 at $t = 0$ rather than with the large values required by the above models.

The fact that there was a forward peak with width $\approx m_\pi^2$ and that the pion-nucleon coupling constant could be calculated from n-p charge exchange scattering data was evidence that the pion played an important part in the scattering process. After the development of the

idea of "conspiracy"*(37), several mechanisms were suggested(32,34) through which the pion could cause a sharp peak in the cross section near $t = 0$. It was shown(32,34) that if there exists a conspirator to the pion, with the quantum numbers of the pion but with positive parity, then it is not necessary for all the pion amplitudes to vanish at $t = 0$. Phillips(32) and Arbab and Dash(34) used a pion conspirator and various other combinations of Regge trajectories (including the ρ and A_2) and were able to fit the $np \rightarrow pn$ and the $\bar{p}p \rightarrow \bar{n}n$ data (although the fits to the $\bar{p}p \rightarrow \bar{n}n$ data were not very good). Several other papers(39-41) have also used conspiracy in fitting n-p charge exchange cross sections.

There have been many objections to the conspirator model. One objection is that a conspirator to the pion is rather artificial, since no particle has been observed which would correspond to the pion conspirator. LeBellac(42) has also shown that the existence of a pion conspiracy leads to incorrect predictions about certain other reactions.

Recent Regge models(43-49) have considered the effects of absorption or rescattering (these show up mathematically as cuts). One such model is the "strong cut Reggeized absorption model"(45-47) (SCRAM), which has the following physical interpretation. Since the front part of a particle can shadow the rear part, the probability that a reaction will occur in which a particle is exchanged in a head-on collision is decreased from its value assuming no shadowing. If the strength of the shadowing is increased compared to estimates based on elastic scattering, there will be a strong suppression of reactions with small impact parameters, leading to diffractive effects. The SCRAM model superimposes these strong absorption effects on a smooth Regge pole amplitude(46).

In the Regge cut models(43-49), the forward peak in n-p charge exchange scattering is caused by the interference of a pion pole and one or more cuts. These cuts are generated in different ways by

* There are certain kinematic constraints in the helicity amplitudes at $t=0$. A set of Regge poles may "conspire" to satisfy these constraints collectively instead of each pole satisfying them separately (38).

the different models. All these models have been successful in fitting the shape and energy dependence of the cross sections at small $|t|$ but have had differing amounts of success at large values of $|t|$. More complicated models will probably be able to improve the fits at large $|t|$. The model of Gotsman and Maor⁽⁴⁸⁾, which suppresses the pion contribution for $-t \geq 0.2 \text{ (GeV/c)}^2$, gives rather good fits at both small and large $|t|$.

Two other recent fits to n-p charge exchange scattering data should be mentioned here. Schopper⁽⁵⁰⁾ was able to get reasonable fits to $np \rightarrow pn$ data and $\bar{p}p \rightarrow \bar{n}n$ data by considering the interference between a Reggeized pion and a phenomenologically chosen background. Lusignoli and Srivastava⁽⁵¹⁾ were able to get good fits to the n-p charge exchange cross section using a model in which the ρ and A_2 trajectories were exchanged in the t channel and a π was exchanged in both the t and the u channels.

The Regge cut models have been quite successful in fitting a large number of different reactions, including n-p charge exchange. Our data will be compared with some of these models in Chapter VI.

CHAPTER III. EXPERIMENTAL SET-UP

This chapter describes the experimental set-up for the n-p charge exchange cross section measurement. A neutron beam was derived at 0° from a Be target in the AGS slow extracted proton beam. The neutrons, with momenta between 6 and 29 GeV/c, bombarded a liquid hydrogen target. The forward-scattered protons from the charge exchange reaction were detected by three proton counters, and their scattering angles and momenta were measured in a spark-chamber magnet spectrometer. The recoil neutrons, with kinetic energies of 1 to 500 MeV, were detected by a bank of fifteen scintillation counters, and their scattering angles and times of flight were measured. Information about each event was recorded on magnetic tape, and was also transmitted to an on-line computer where a preliminary analysis was done.

Section A describes the neutron beam line; Section B, the liquid hydrogen target and the anticounters; Section C, the proton arm of the experiment, including the proton counters and the spectrometer; Section D, the neutron counters; and Section E, the logic and computer readout system.

A. Beam Line

During this experiment (AGS Experiment #411) the Brookhaven Alternating Gradient Synchrotron was run at an average beam momentum just prior to ejection of 28.5 GeV/c. The cycle time of the machine was three seconds; spill length in the slow extracted proton beam was 300 to 500 msec.

Figure 3.1 is a simplified drawing of the beam line. The slow extracted proton beam, containing about 2×10^{11} protons per burst, was steered onto a Be target (Target "A") 0.1 inches high by 0.2 inches wide by 7.1 inches long (0.6 collision lengths). A neutral beam was defined at 0° relative to the incident beam. Charged particles were swept out of the beam by dipole magnets D_1 , D_2 , D_3 and pitching

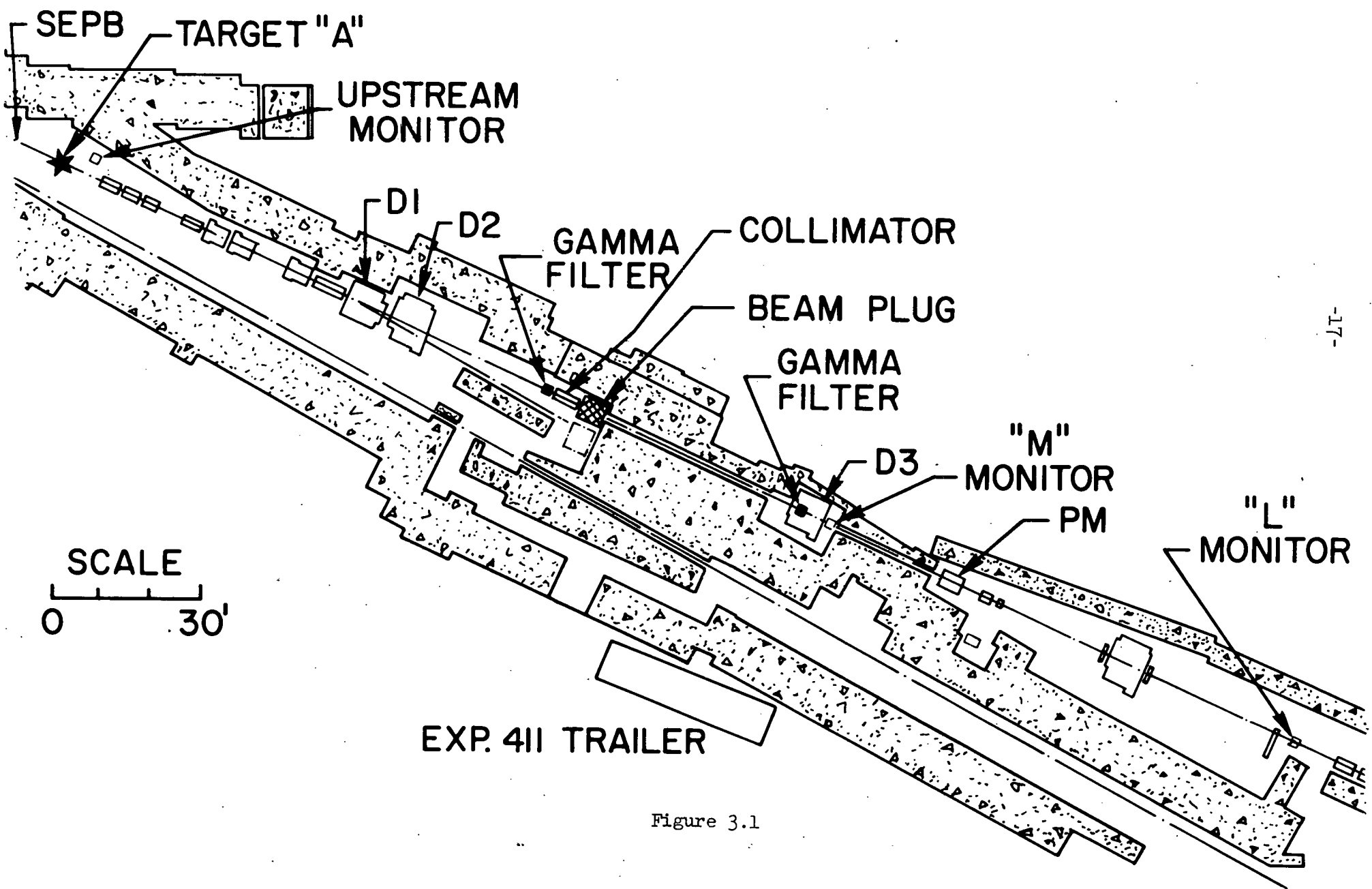


Figure 3.1

magnet PM. The proton beam was deflected to one side and was stopped by four feet of lead and approximately 100 feet of heavy concrete. Accidentals in the neutron counters from muon production by protons in the shielding turned out to be a problem but were reduced by deflecting the proton beam further away from the beam line. Gamma rays were converted by 1 inch of lead (4.2 radiation lengths); the charged particles produced in the lead were swept aside by magnets D_3 and PM. Contamination of the neutron beam by gammas was estimated to be less than one percent; contamination by kaons was negligible.

An indication of the uniformity of the beam intensity came from the "upstream monitor", which was placed several feet downstream from the target and several feet from the beam line. This monitor was a Čerenkov counter consisting of a one inch diameter by 8 inch long lucite rod attached to a 53 AVP photomultiplier tube. The output of this counter was displayed on a oscilloscope and was used to gate off the electronics during beam spikes (see Section E).

The size of the neutron beam was defined by a three foot long brass collimator with a 9/16 inch diameter hole, located 105 feet from the target. The beam halo was reduced by oversize collimators in magnets D_3 and PM. At the position of the liquid hydrogen target, 194 feet downstream from target A, the beam was circular, one inch in diameter, with negligible halo. To measure the position of the beam, a film holder containing a thin converter, a phosphorescent screen, and a Polaroid film was placed in a surveyed position in the beam line.

The beam subtended a solid angle of 1.55×10^{-7} sr at the production target and had a maximum divergence of 0.2 mrad. It contained approximately 10^6 neutrons per pulse over the momentum range of 6 to 29 GeV/c.

The beam flux was monitored by two telescope counters, M and L, one upstream and one downstream of the experimental area. Each telescope consisted of an anticounter M_1 (1/8 inch thick) followed by a 1/2 inch thick lucite converter and two more counters M_2 and M_3 (each 1/8 inch thick). A count was

defined as $M = \bar{M}_1 M_2 M_3$. The detection efficiencies were approximately 3% for neutrons and 4% for gammas. Accidentals, defined as $\bar{M}_1 M_2^{\text{delayed}} M_3$, were less than 1% at the highest beam fluxes. When corrections were made for the condition of the liquid hydrogen target (full or empty), the two counters M and L tracked to within 2% during the experiment.

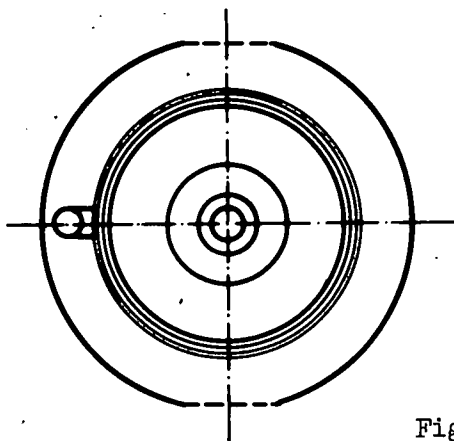
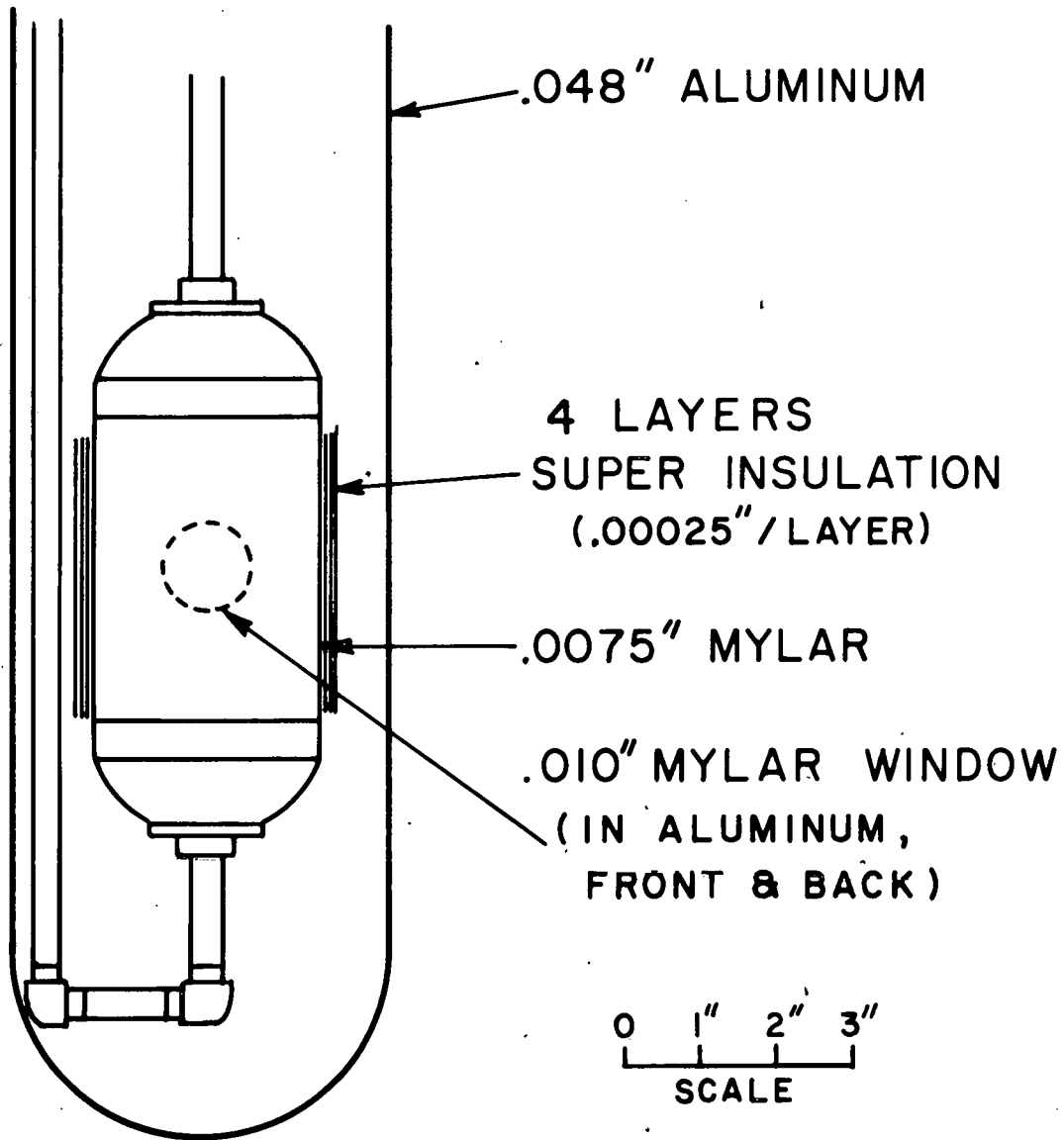
A total absorption spectrometer (TAS) approximately 250 feet downstream of the main experimental area was used to determine the number of neutrons per monitor count. Appendix C describes the TAS and the normalization procedure.

B. Liquid Hydrogen Target and Anticounters

The liquid hydrogen target (LH_2) shown in Figure 3.2, was a vertically mounted 3 inch diameter cylinder of 0.0075 inch mylar, wrapped with 4 layers of 0.00025 inch super insulation. The target was enclosed in a cylinder of 0.048 inch aluminum with 1.25 inch diameter mylar windows .010 inches thick for the beam. The neutron beam was attenuated by approximately 2% in passing through the target.

The layout of the anticounters surrounding the target can be seen in Figure 3.3. A_0 was a thin (1/16 inch) scintillation counter used to ensure that a neutral particle entered the target. A_1 ensured that a neutral particle left the target on the side of the neutron counters. A_0 and the side of A_1 facing the neutron counters were kept as thin as possible; they were sensitive only to charged particles. The rest of the anticounters consisted of alternate layers of scintillator and lead and were therefore sensitive to gammas as well. The "baffle" counters A_2 and A_3 were used to detect particles which escaped through the hole in the downstream end of the anticounter box surrounding the target.

The anticounters vetoed approximately 9 out of every 10 proton candidates. Approximately 5% of the good events were vetoed due to accidentals in the anticounters.



TOP VIEW

Figure 3.2

LIQUID HYDROGEN TARGET

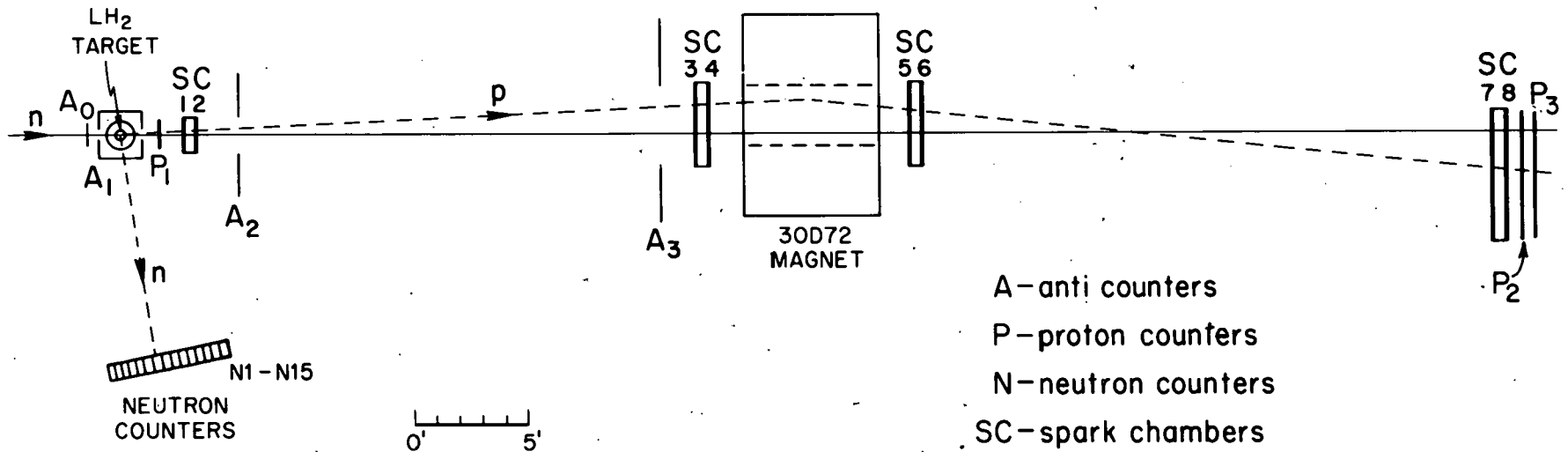


Figure 3.3

C. The Proton Arm

This section describes the proton arm of the experiment, which consisted of three proton counters and a wire-spark-chamber magnet spectrometer. The layout of the experimental area is shown in Figure 3.3.

There were three proton scintillation counters: P_1 , 30 inches downstream of the target, and P_2 and P_3 , approximately 5 inches downstream of the last wire chamber. Counter P_1 was thin ($1/8$ inch thick) to minimize interactions with the neutron beam. P_2 and P_3 were $3/8$ inch thick. The signal from P_1 set the timing for the event, and for that reason the signal was kept short by a clipping line 3 nsec long. In order to set the relative timing between the proton counters and the neutron counters, a nanosecond light pulser was attached to each of the counters. This system is described in Chapter III-D.

To minimize multiple coulomb scattering of the protons, a helium bag 210 inches long by 36 inches in diameter was placed between spark chambers SC2 and SC3, upstream of the magnet, and another helium bag 250 inches long by 55 inches in diameter was placed between SC6 and SC7, downstream of the magnet. The total material between the LH_2 target and the center of the magnet was 1.6 gm/cm^2 (0.039 radiation lengths) and the total material between the center of the magnet and the last spark chamber was 0.8 gm/cm^2 (0.016 radiation lengths). The angular uncertainty in the proton direction due to material in the hydrogen target and the first proton counter was approximately 0.05 mrad at 25 GeV/c.

The spectrometer consisted of eight wire spark chambers, four on each side of a 30 inch wide by 72 inch long magnet with a 6 inch gap. On each side of the magnet, the chambers were placed in two sets of two chambers each, with a separation between the sets of about 25 feet.

Each chamber consisted of orthogonal wire planes epoxied to opposite sides of a $3/8$ inch fiberglass frame. There were 24

aluminum wires (0.0071 inch diameter) per inch. A sheet of 0.003 inch mylar was glued over each side of the frame using RTV Silastic cement. A mixture of 90% neon and 10% helium flowed in the gap at a pressure slightly above atmospheric.

The chambers were attached to aluminum frames which supported them and contained the high voltage connections. Two chambers were attached to each 2 inch thick frame, one on each side. The inside planes were connected to the high voltage and the outside planes were connected to ground. One chamber in each set had wires running horizontally and vertically, and the other chamber had wires at 45° and 135° . The use of two chambers with different wire orientations helped to resolve ambiguities in spark positions when there was more than one spark in a chamber.

The chambers were pulsed at about 10 kV by a set of spark gaps and capacitors. A d.c. clearing field of 50 volts was applied to the chambers to sweep away ions produced by the discharge. A dead time gate of 25 msec after each trigger allowed the spark chambers to recover.

As has been pointed out by other authors⁽⁶⁾, a plane of parallel wires is not electrically equivalent to a conducting plane. Propagation of high voltage pulses in a wire spark chamber is slower than in a foil spark chamber, and wave reflection problems are more likely to occur. These problems were reduced in our case by placing a sheet of aluminum foil over the high voltage plane of each chamber and by connecting the foil to the high voltage. A sheet of mylar was then cemented over the foil with RTV, and the inside sheet of mylar was punctured to allow the gas to flow in the region containing the foil. A hole was cut in the foil at the position of the beam.

The active areas of the chambers were as follows: 7.0 inches by 11.75 inches for chambers SC1 and SC2, 9.5 inches by 32 inches for SC3 and SC4, and 16 inches by 46 inches for SC5, SC6, SC7, and SC8. The net mass per chamber was 0.042 gm/cm^2 .

Spark positions were determined using magnetostrictive delay lines attached to aluminum "wands" and a MIDAS digitizing system (Science Accessories Corporation)⁽⁵³⁾, which is described more fully in Section E of this chapter. The current flowing through the wire associated with a spark set up a disturbance in the magnetic domains of the delay line at the position where the wire crossed the delay line. The disturbance propagated down the delay line at the speed of sound and was detected at the end of the delay line by a pick-up coil connected to a pre-amplifier. The position of the spark was determined from the time difference between the signal from a spark and the signal from a fiducial in the spark chamber. A second fiducial in each chamber, at a known distance from the first, served as a reference of time versus position. Only signals above the reference level set on the comparators of the SAC scalars were detected; small noise pulses were thus eliminated. The MIDAS system could digitize two sparks for each of the sixteen delay lines (one delay line for each wire plane). Uncertainties in spark positions were less than ± 1 mm.*

It was found that when the magnet was turned on, there were fields of approximately 100 to 200 gauss in the vicinity of the chambers closest to the magnet. The magnetostrictive delay lines would not operate properly with these fields present, and it was necessary to shield the delay lines with 3/8 inch thick soft iron plates. With the shielding present, the magnetic fields had little effect on signals from the pre-amplifiers.

To eliminate certain kinds of noise from the delay line pre-amplifier outputs, especially "pre-fiducial noise" (which appeared after the usual noise from the discharge but before the first fiducial), it was necessary to put electrostatic shields around the pre-amplifier boxes and to run a ground strap from the spark gap boxes to the pre-amplifier boxes. The common ground reduced the noise pulses to 0.1 to 0.2 volts, compared to signal pulses of 0.5 to 1.5 volts.

The analyzing magnet was a 30D72 magnet supplied by Brookhaven

* Unless otherwise stated, quoted uncertainties are one standard deviation.

Laboratory. The current in the magnet was set using a potentiometer to measure the voltage across a low resistance shunt. After the current was set, it was monitored with a digital voltmeter connected across the shunt. The magnet was run at two different currents, 2020 amperes and 1340 amperes. The lower setting was used during part of the running because some of the lower momentum protons were deflected outside the range of the last spark chamber when the larger field was used.

A magnet of this type was mapped by the AGS Magnet Measurements Group, which supplied information on the central field versus current, on the field as a function of position, and on the field integral $\int B \cdot dl$ at various positions. At the time of the experiment, the field was measured at 200 points and at several different current settings, using a Hall probe which had been calibrated with a nuclear magnetic resonance probe. These measurements agreed to better than 0.5% with those taken by the Magnet Measurements Group. The fields at the center of the median plane were 17.998 KG and 12.222 KG at 2020 amperes and 1340 amperes respectively. The corresponding field integrals along the center line of the magnet were 1416.2 KG-in and 976.8 KG-in, with uncertainties of less than 0.5%.

Fringe fields extended into the region beyond the spark chambers closest to the magnet. The field integral in the region beyond the chambers was less than 0.1% of the total $\int B \cdot dl$, so no correction was necessary.

In order to check the alignment of the chambers, two kinds of special runs were made: runs with the center wires of the chambers shorted (using no beam), and "straight-through" runs with the magnet turned off. These runs are described in Chapter V-A. After small corrections were made, the scattering angles of the proton were determined to better than 0.2 mrad, which corresponds to a position uncertainty in each chamber of approximately 1 mm. The proton momentum was measured to better than 0.8% at 25 GeV/c.

The efficiency of the chamber system was approximately 98.5%. The procedure for determining the efficiencies of the chambers is described in Chapter V-A.

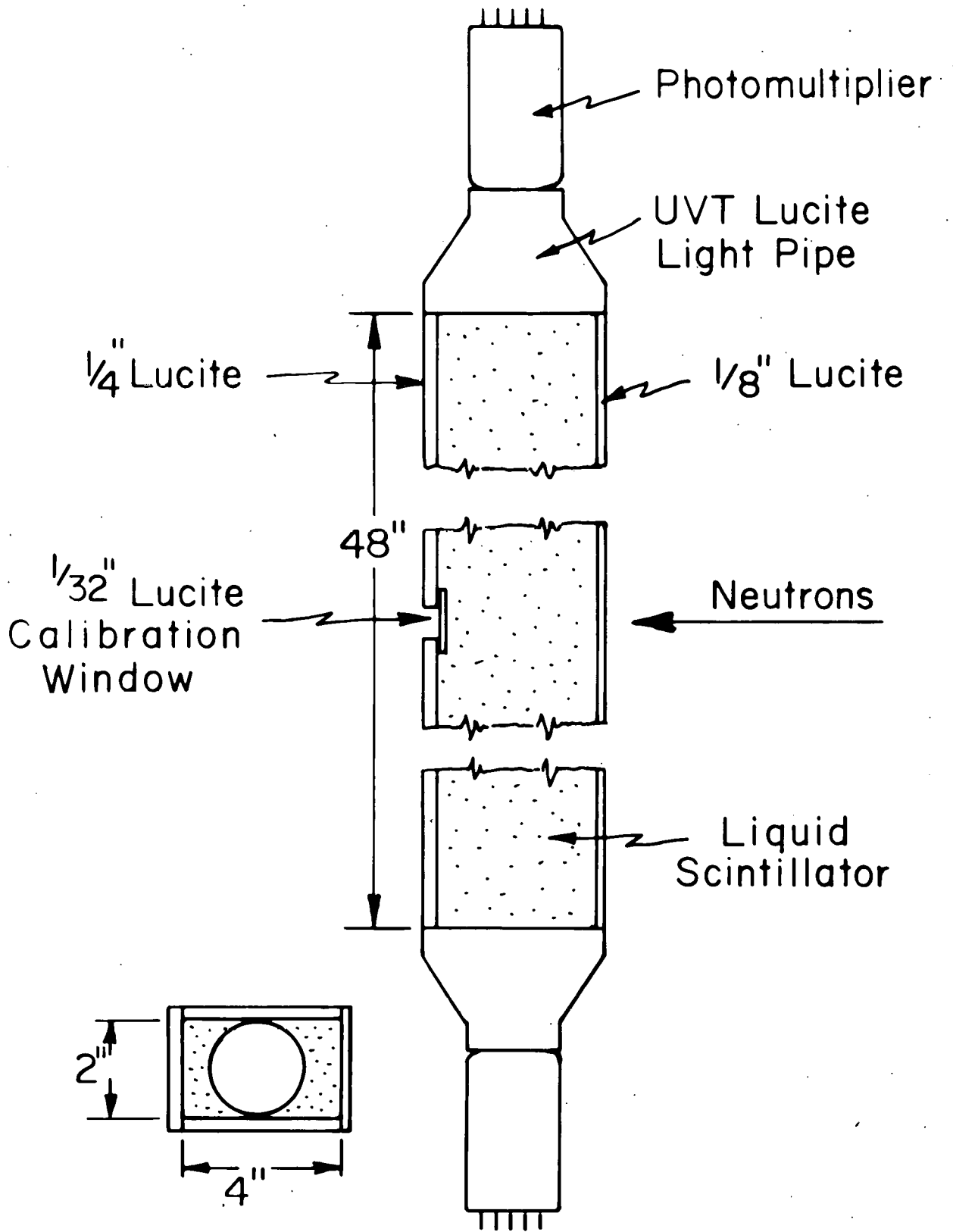
D. The Neutron Arm

This section describes the neutron counters, the procedure for setting and checking their thresholds, and the methods used for setting the timing and measuring the speed of light in the counters. A separate experiment to measure the efficiencies of the neutron counters is described in Appendix B.

The recoil neutrons, with energies of 1 MeV to 500 MeV, were detected by a bank of 15 scintillation counters, $N_1 - N_{15}$, which subtended the angular region from 60° to 90° with respect to the incident neutron beam. The neutron counters, shown in Figure 3.4, were lucite boxes 4 inches deep by 2 inches wide by 48 inches high, filled with a mixture of mineral oil and scintillator which is described elsewhere⁽⁵⁴⁾. It was necessary to have the counters as deep as possible to improve the detection efficiency but as thin as possible to improve the timing resolution; the depth of 4 inches was a compromise between these two requirements. The centers of the counters were approximately 94 inches from the target: uncertainties of ± 2 inches in the neutron interaction position because of the counter depth therefore caused uncertainties in the neutron time of flight of approximately 2%. Three sides of each counter were made of 1/4 inch lucite; the fourth side, the neutron entrance face, was of 1/8 inch lucite. The counters were mounted vertically, three inches apart center-to-center. They were in a straight line, with the center counter being 94 inches from the target. Each counter was rotated so that it faced the target.

The counters were wrapped with aluminum foil and black tape. Each counter was viewed by two RCA 8575 photomultiplier tubes coupled to the scintillator by 6 inch long UVT lucite light pipes. Relative timing between the two photomultipliers determined the position of the neutron interaction in a counter to approximately ± 2 inches.

The efficiency of each counter depended on the light collection threshold, which was a function of the light collection efficiency of the counter, the gain of the photomultipliers, and the discriminator levels. To facilitate setting and checking the thresholds, a 1/32 inch lucite window was provided on the back of each counter. A



LIQUID SCINTILLATION COUNTER

Figure 3.4

calibrated beta source (~ 100 μCi of Sr-90) was placed over the window and the singles rate of each photomultiplier was measured. Frequent adjustments (at least once per day) of the voltages of the photomultipliers were made to keep the singles rates (and therefore the gains) constant over the course of the experiment. Changes in gain corresponding to changes in the photomultiplier high voltage of less than one volt were corrected. Rate dependent fluctuations in gain were minimized by using high current bases (3ma) and by stabilizing the voltages on the last three dynodes of the photomultipliers with external power supplies.

Thresholds for the neutron counters were originally set by measuring the maximum pulse height observed in the counter from a Sr-90 source, which emits betas with a maximum energy of 2.2 MeV. The assumption was made that a beta produces five times as much light as a proton of equal energy,⁽⁷²⁾ and that a neutron would put most of its energy into protons in the scintillator. Using this assumption, an estimate was made of the pulse height required for the beta in order that the lowest energy neutron would produce a pulse height above 0.14 volts (the discriminator level). After the photomultiplier gain was set to the proper value, the singles rate was measured. An average value of the singles rate was used to set the gain of the counter in all future running.

It was necessary to keep the neutron counter gains as low as possible to reduce backgrounds. The gain required for each counter was determined by the energy of the lowest energy neutron in the angular range of that counter. Table 3.1 lists the angular, energy, and time of flight ranges of each of the neutron counters, as well as information on the threshold settings.

Since neutrons can produce a large range of pulse heights, it was useful to have pulse height information on each neutron interaction in order to improve timing resolution. The outputs of the last dynode of the photomultiplier on the bottom of each counter were "daisy chained" together in two groups, and the signals were sent to an analog-to-digital converter, as shown in Figure 3.5.

ANGULAR, ENERGY, AND TOF RANGES FOR THE NEUTRON COUNTERS

Counter	Scattering Angle with Respect to the Beam (degrees)	Neutron Kinetic Energy (MeV)	TOF (nsec)	Average TOF (nsec)	Minimum Energy β Detectable (MeV)	Counting Rate with Standard Sr-90 Source (KHz)
1	85.8 - 88.8	1 - 7	66 - 226	146	0.19	300
2	84.0 - 87.0	1 - 17	43 - 203	123	0.24	250
3	82.3 - 85.3	8 - 30	33 - 63	47	0.44	188
4	80.5 - 83.5	18 - 47	27 - 43	34	1.01	75
5	78.6 - 81.6	30 - 68	23 - 33	27	1.01	75
6	76.8 - 79.8	46 - 94	20 - 28	24	1.01	75
7	75.0 - 78.0	64 - 123	18 - 24	20	1.01	75
8	73.2 - 76.2	88 - 157	16 - 21	18	1.01	75
9	71.4 - 74.4	115 - 196	15 - 18	16	1.01	75
10	69.5 - 72.5	146 - 234	14 - 17	15	1.01	75
11	67.7 - 70.7	190 - 290	13 - 15	14	1.01	75
12	65.9 - 68.9	230 - 350	12 - 14	13	1.01	75
13	64.1 - 67.1	270 - 400	12 - 13	12	1.01	75
14	62.4 - 65.4	320 - 470	11 - 12	11	1.01	75
15	60.6 - 63.6	400 - 540	11 - 12	11	1.01	75

Table 3.1

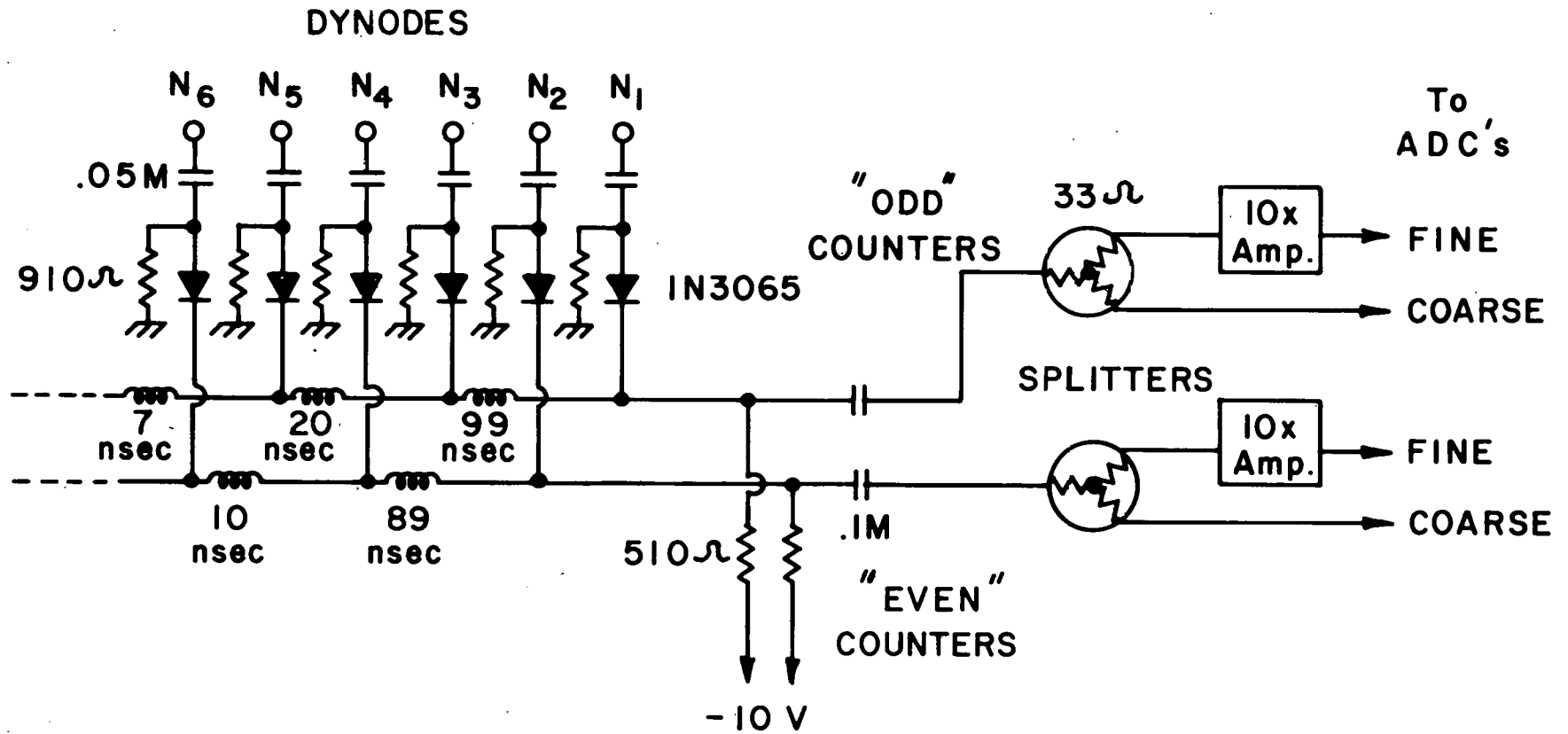


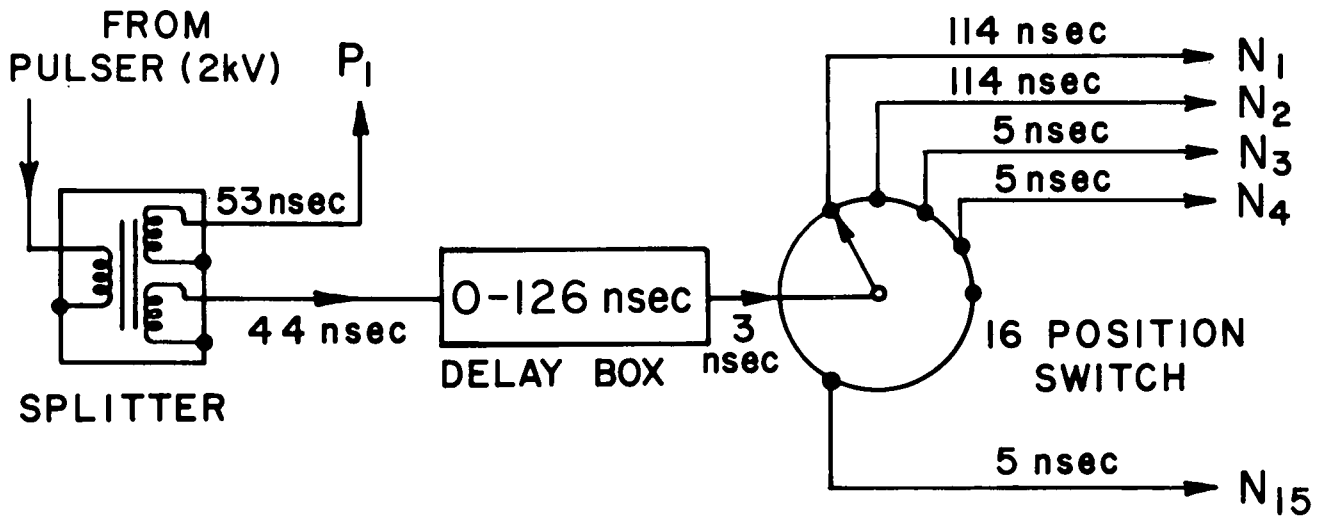
Figure 3.5

Delays between counters ensured that all signals would arrive at the ADC's at approximately the same time. Diodes prevented the feeding of the signal from one photomultiplier into another.

Because of the long distance between the experimental area and the electronics trailer, the shortest cables were more than 100 nsec long. In order to preserve timing and pulse height information, it was necessary to use low attenuation cable. Therefore the signal cables for the neutron counters and for proton counter P_1 were low-attenuation RG-8 or RG-9 cable. All other signal cables (anticounters, spark chamber pre-amplifiers, etc.) were RG-58 cable.

It was necessary to shield the neutron counters from thermal neutrons in the AGS experimental area. The neutron counter array was enclosed on all sides except the side facing the target by several feet of concrete, lead, and paraffin. The neutron counter cave had a roof of concrete blocks several feet thick.

In order to set the timing of the neutron counters relative to the proton counters and to set the timing of the upper end of each counter relative to the lower end, a nanosecond light pulser, made by Pek Labs,⁽⁵⁵⁾ was attached to each proton counter and to the center of each neutron counter. Figure 3.6 is a simplified diagram of the pulser system. A 2 kV pulse was sent to a splitter, which sent the pulse to the first proton counter P_1 and to the neutron counter determined by the switch box. The pulse to the neutron counter was delayed by the average time of flight of neutrons in that counter (see Table 3.1). The timings determined in the Pek lamp runs were used as references against which the timings of real events were measured. Pek lamp runs were taken frequently during the experiment to check for drifts in timings, and appropriate corrections were applied to the data. After these corrections were made, uncertainties in neutron time of flight were approximately ± 2.5 nsec for counters N_1 and N_2 and approximately ± 1.5 nsec for counters $N_3 - N_{16}$. Uncertainties in timing between the two ends of a counter were less than 1 nsec, giving up-down position uncertainties of approximately ± 2 inches.



DELAYS ON DELAY BOX

N_1	24nsec	N_7	9nsec	N_{13}	1nsec
N_2	0	N_8	7	N_{14}	0
N_3	36	N_9	5	N_{15}	0
N_4	23	N_{10}	4		
N_5	16	N_{11}	3		
N_6	13	N_{12}	2		

Figure 3.6

Several types of measurements were made with the Pek lamps. A rough calibration was made of digital pulse area reading (from the last dynode) versus anode pulse height for each counter, as observed on an oscilloscope. Timing differences between the ends of each counter were measured as a function of pulse height; as expected, pulse height had little effect on these timing differences. Because of the limited range of pulse heights available from the Pek lamps, it was not possible to use the lamps to study the dependence of the measured time of flight on the neutron counter pulse height. Chapter V-B describes a method for determining pulse height corrections to time of flight using the data from the cross section measurements.

In order to find the relationship between the position of an interaction in a neutron counter and the timing difference between the ends of the counter, a series of runs was made using a special counter. A 48 inch long $1/2$ inch diameter scintillation counter was placed one inch behind the neutron counter array at various heights. A block of parafin was placed in the beam line at the position of the hydrogen target to produce charged particles. The elements required in the trigger were the counter A_1 between the target and the neutron counter array, both ends of a neutron counter, and the special counter. By measuring the timing difference between the two ends of a counter as a function of the position of the interaction, it was possible to determine the speed of light in each counter. The measured speed of light in the counters varied from 14.3 mm/sec to 15.7 mm/nsec.

E. Electronics

The electronic circuitry for this experiment was located in a trailer approximately 100 feet from the experimental area. The electronics consisted of the logic circuitry for selecting events, the digital converters for converting timing and pulse height information into binary numbers, and the data box for storing the digital information until it could be written on magnetic tape and sent to the on-line computer.

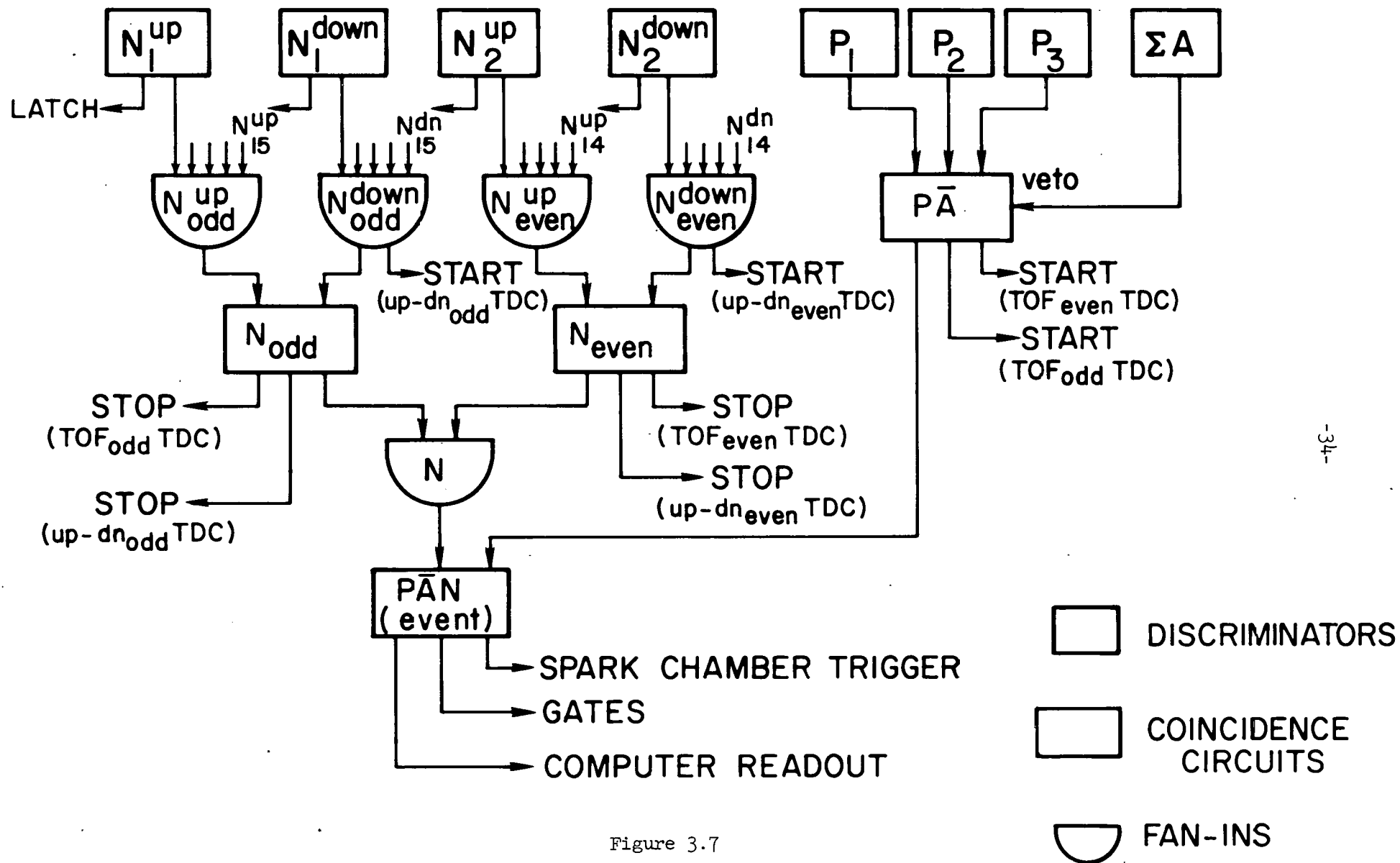


Figure 3.7

SIMPLIFIED LOGIC DIAGRAM

A simplified block diagram of the logic is shown in Figure 3.7. Signals from the anodes of the photomultipliers at each end of the fifteen neutron counters were brought to Chronetics 101 discriminators through voltage limiters which limited the discriminator inputs to 0.7 volts. One output of each discriminator went to a neutron counter latch. The neutron counters were grouped into two banks, the "odd" counters, N_1, N_3, N_5 , etc. and the "even" counters, N_2, N_4 , etc. The neutron counter part of the trigger was satisfied if the upper end of any odd counter was in coincidence with the lower end of any odd counter (not necessarily the same counter), or similarly for the even counters. Since the logic for even and for odd counters was independent, it was possible to have a count in both an odd counter and an even counter and not lose any information on the event. If there was a count in more than one counter in a bank, however, the timing and pulse height information in that bank was lost.

The signals from the eighteen photomultipliers on the anti-counters were fanned together and brought into anticoincidence with the signals from the three proton counters. The output of the $P\bar{A}$ coincidence, with P_1 timing, was used to start the neutron time of flight time-to-digital converters (TDC's or "digitimes"). The outputs of the N^{down} fanouts were used to start the digitimes for up minus down timing. The outputs of the $N^{\text{up}}N^{\text{down}}$ coincidence circuits, with N^{up} timing, were used to stop the up minus down digitimes and the neutron time of flight digitimes.

An event consisted of a count in all three proton counters, no counts in any of the anticounters, and a count in one or more neutron counters. A signal from the event coincidence $P \cdot \bar{A} \cdot N_1^{\text{up}} \cdot N_j^{\text{down}}$ triggered the spark chambers; enabled the digital electronics, including the neutron counter latches, digitimes, and pulse area ADC's; initiated the reading of the data into the data box by the SAC Master Control (described below); gated off the fast electronics for the duration of the read-out cycle; and started a delay gate of 25 msec to allow the spark chambers to recover.

Not shown in the figure are sixteen TSI scalers, the outputs of which were digitized in BCD form and read into the data box memory. Also not shown is the beam gate. A 1 kHz signal from the AGS machine, which was synchronized with the AGS machine cycle, was used to generate "start of burst" and "end of burst" signals. The start of burst signal enabled the electronics and triggered the oscilloscope which was used to monitor the beam spill. The end of burst signal instructed the data box to dump its contents into the computer and onto the magnetic tape if the data box was full. The electronics was gated off during beam spikes by a signal from the upstream monitor counter.

Figure 3.8 is a simplified block diagram of the digital electronics and computer interface. A SAC 1204 Master Control (Science Accessories Corporation)⁽⁵³⁾ read the digital information on spark coordinates, pulse heights, latches, and timings into a memory, the "data box". From the data box the data was written onto magnetic tape and sent to an on-line computer.

The SAC 1148 Enenkontakaihhex Scaler accepted pulses from the pre-amplifiers on the sixteen magnetostrictive delay lines of the spark chambers. Typical signals were 0.5 to 1.5 volts, and the comparator levels were approximately 0.35 to 0.45 volts. The leading edge of the front fiducial pulse started two scalers which counted pulses from a 20 MHz clock; one scaler was stopped by the center of the pulse from the first spark and the second scaler was stopped by the center of the pulse from the second spark (or second fiducial).^{*} If no spark was present, the second fiducial stopped the first scaler, and the second scaler overflowed, setting a scaler overflow bit. If more than two sparks were present, a spark overflow bit was set. For each delay line, there were two 14 bit scaler readings, plus scaler overflow and spark overflow bits. With a 20 MHz clock, each scaler count corresponded to approximately 0.25 mm.

* For more details on the method used for finding the center of the pulses, see reference 53.

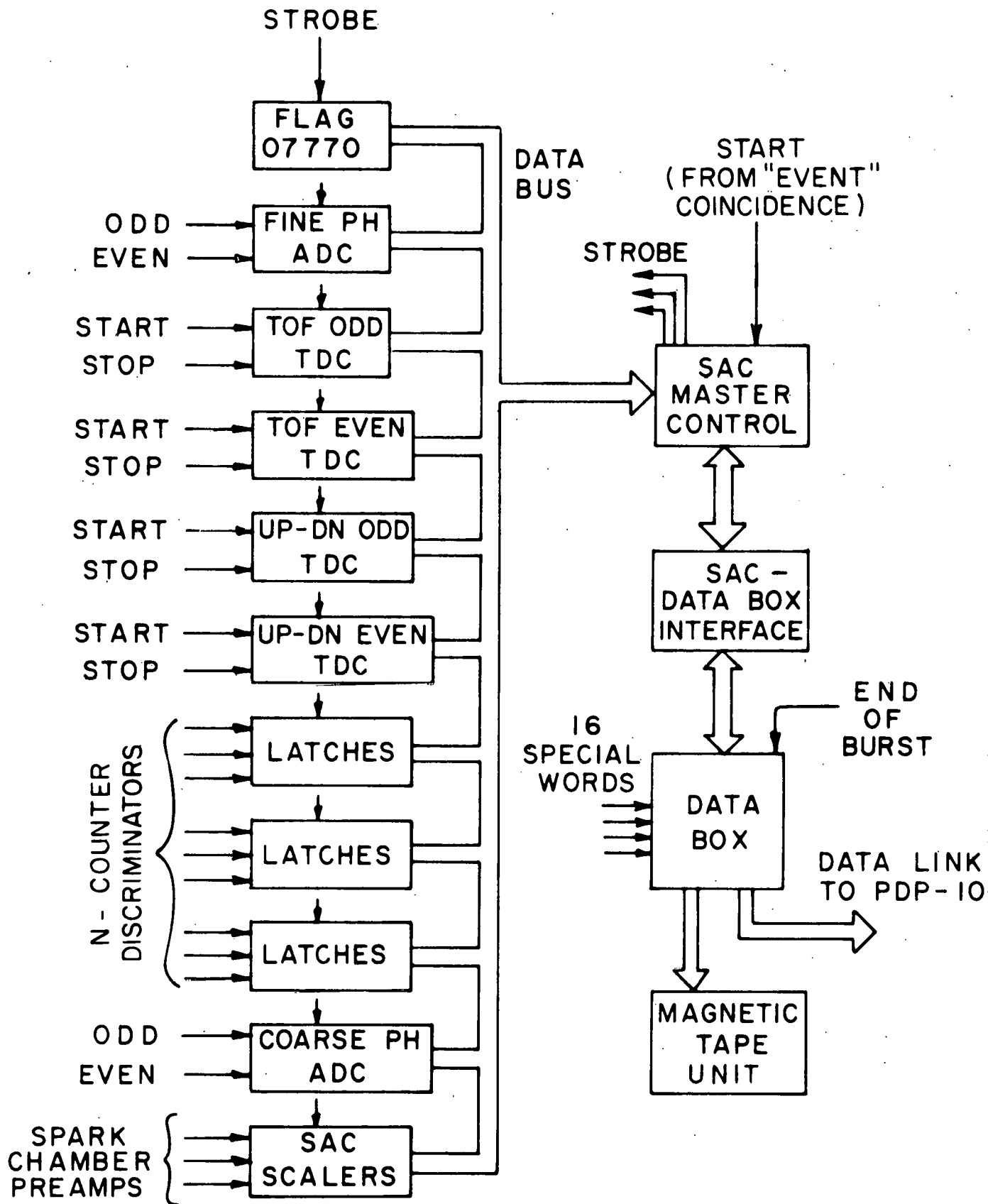


Figure 3.8

The analog to digital converters (PPA Quad ADC's)⁽⁵²⁾ converted the dynode pulse areas into 6 bit binary numbers. There were four ADC's, for even and odd counters and for coarse and fine pulse heights. Full scale readings were obtained from photomultiplier pulses of approximately 10 volts. The "fine" ADC's were preceded by 10x amplifiers.

The time to digital converters (PPA Digitimes) digitized the timing differences between the proton (P_1) signal and the neutron (N^{up}) signal, and the timing differences between the signals from the two ends of a neutron counter. There were two digitimes for neutron time of flight (odd and even counters) and two digitimes for up minus down timing. Each digitime generated a 12 bit word. One count in the time of flight digitimes corresponded to approximately 0.1 nsec; one count in the up minus down digitimes corresponded to approximately 0.01 nsec or 0.7 mm.

The latches (EG&G strobed coincidence circuits C146/N) recorded which neutron counters were involved in an event. Both ends of fifteen neutron counters were latched, for a total of 30 bits. The information was put into three 12 bit words.

In addition to the data, a fixed data flag word, 077770_8 , was read in to mark the beginning of each event.

A SAC 1204 Master Control coordinated the transfer of data between the data modules and the data box. Upon receiving a signal from the "event" coincidence circuit, the Master Control applied signals in sequence to the strobe inputs of the various data modules, gating their contents onto the data bus one at a time. This information was packed into 36 bit words by the SAC-data box interface and was stored in the data box memory. The Master Control scanned the ten data modules and then the 1148 scaler with its 32 spark chamber scalers.

The data box, supplied by the Brookhaven On-Line Data Facility, consisted of a Varian 4096 word x 36 bit memory and the necessary control logic for reading from the SAC-data box interface and for writing onto the magnetic tape unit and onto the data link to the

PDP-10 computer. The data box stored the digital information until it contained a preset number of words. At the next end of burst signal the data box stored the 16 special words (which in this case were TSI scalars and some fixed data) and the "last word" (which contained the word count and some fixed data), and then wrote the contents of the memory onto magnetic tape and sent it to the computer.

The magnetic tape unit was a 7 track 556 bpi Potter unit. There was no communication between the tape drive and the computer.

The on-line PDP-10 computer, supplied by the Brookhaven On-Line Data Facility, was used on a time-sharing basis to do a preliminary analysis of the data and to monitor the performance of the spark chambers and neutron counters. Instructions were given to the computer via a model 35 Teletype located in the experimental trailer. Output from the computer was printed on the Teletype or displayed on a Tektronix display scope. The on-line programs are described in the next chapter.

CHAPTER IV. DATA TAKING AND ON-LINE ANALYSIS

Part A of this chapter describes the data taking phase of the experiment, including some of the routine checks that were made on the equipment. Part B describes the on-line data analysis program.

A. Data Taking

The data presented in this paper were taken from May 23, 1970 to July 5, 1970. Data on the neutron beam flux were taken during July 1970 and are described in Appendices C and D.

Data were taken at two different magnet settings, 18.00 and 12.22 KG (central field). For each magnet setting, runs were taken with a full and with an empty target. The usual procedure was to take 3 or 4 runs of 1 to 4 hours each with the target full and then to take one run with the target empty. After several such sets, the magnet field would be changed. Table 4.1 gives the amount of data taken under various conditions.

The data were written on magnetic tape (556 bpi, 7 tracks) in blocks of 10 to 20 events (200 to 400 words). Approximately 2/3 of a 2400 foot tape was used each day to record 6 to 10 runs with approximately 2×10^4 triggers. Every day a new tape was mounted and the old tape was immediately copied and checked for parity errors. Thirty-one tapes were used (26 excluding light pulser runs and other special runs).

Several times a day, special runs were made to check the performance of the neutron counters, spark chambers, proton counters, and anticounters. Some of these runs were recorded on magnetic tape and some were not. Among the special runs were the following.

- (a) Timing and performance checks of the neutron and proton counters were made by pulsing the Pek lamps mounted on the centers of the neutron counters and on the proton counters. Histograms were made of the timing; any changes in timing between two runs were investigated.

Table 4.1

AMOUNT OF DATA TAKEN

	Target Full		Target Empty	
	<u>18 KG</u>	<u>12 KG</u>	<u>18 KG</u>	<u>12 KG</u>
Number of runs	91	40	29	11
Number of monitor counts (millions)	6241	2846	1299	515
Number of triggers (thousands)	222	108	28	12
Number of events surviving all cuts	16107	7391	137	59
Total events surviving all cuts	23498		196	

- (b) The gain of each neutron counter was checked and adjusted at least once a day using a beta source (see III-D).
- (c) Each individual anticounter was placed in coincidence with the first proton counter, and the ratio P_1A/P_1 was checked; changes in the ratio were investigated.
- (d) Signals from each magnetostrictive delay line were examined using an oscilloscope and adjustments in pre-amplifier gain or comparator level were made as necessary. For these tests, the anticounters were removed from the trigger requirement to increase the trigger rate. Histograms of spark distributions for each wand were made.

B. On-Line Analysis

The on-line PDP-10 computer was an extremely valuable tool during the tuning up stage of the experiment and was very useful in monitoring the performance of the equipment during the actual running. The on-line program occupied approximately 25K words of core. A preliminary analysis was done on each event, and messages were printed for certain kinds of failures. Among the problems, which generated error messages were incorrect BCD data from the TSI scalers; no neutron latch; and spark chamber problems such as no fiducial or fiducial out of tolerance. These error messages were very useful for detecting equipment failure.

Any of 90 different histograms could be displayed on the scope on command from the experimenter. Among the histograms were

- (a) spark distributions for each magnetostrictive delay line ("wand") as a function of position; these displays were valuable for detecting edge sparks and breakdowns.
- (b) the number of sparks per event (0, 1, >1) for each wand; a large number of zeros or greater-than-ones would indicate trouble in a chamber.

- (c) horizontal and vertical target projections; gross beam alignment problems would show up in these displays.
- (d) the number of events at each end of each neutron counter; too high or too low a rate for a given counter relative to other counters would indicate a problem in that counter.
- (e) the time of flight, up minus down timing, and pulse height distributions for each counter; these displays checked the general performance of each counter.
- (f) the results of the preliminary analysis, such as the fourth momentum transfer and the calculated incident neutron momentum.

At the end of each run, a run summary was printed on the Teletype. Each run summary contained information on the total number of failures of various kinds which occurred during the run, such as the number of events with no neutron counter latch or with no second fiducial. It also listed the ratios of various TSI scalers, such as triggers per monitor and $N^{\text{up}}/N^{\text{down}}$. The ratios were checked carefully from run to run and any significant changes were investigated.

CHAPTER V. DATA ANALYSIS

This chapter describes the off-line data analysis, done on the Princeton IBM 360/91 computer. The analysis consisted of the following procedure. Each proton track through the spectrometer system was reconstructed and the vector momentum of the proton was calculated. Using information from the neutron arm, the time of flight and the scattering angles of each neutron were calculated. Since the vector momenta of both particles in the final state, as well as the direction of the incident neutron, were known, there were three constraints on the kinematics of each event. These three constraints were used as follows. Assuming that each event was elastic, the measured proton vector momentum was used to calculate the expected neutron angles and time of flight. These calculated* parameters were compared with the measured* ones and loose cuts were made on the three differences. Those events which survived all three cuts were taken as the elastic sample. The number of elastic events as a function of t and p_{lab} was divided by the acceptance of the apparatus (from a Monte Carlo calculation), yielding relative cross sections. A separate measurement of the neutron beam flux was used to normalize the cross sections.

Part A describes the track reconstruction; part B describes the kinematic reconstruction of events and the selection of the elastic events; part C describes the Monte Carlo acceptance program; and part D describes the normalization procedure.

A. Track Reconstruction

The first stage of the analysis consisted of reading the raw data tapes, converting the spark coordinates into proton trajectories through the magnet, and writing the partially analyzed events on a secondary data tape.

* In this chapter, the "measured" values of the neutron angles and time of flight are those measured by the neutron counters; the "calculated" values are those calculated from the spark chamber information, assuming that the event is elastic.

The coordinate system used in all the analysis programs is shown in Figure 5.1. The coordinate system was a right-handed system with its origin at the center of the hydrogen target. The positive z axis pointed down the beam line, the positive y axis pointed directly downward, and the positive x axis pointed to the right as one looked downstream. The laboratory scattering angles of the proton and the neutron, θ_p and θ_n , were measured with respect to the positive z axis. The azimuthal angles of the proton and the neutron, ϕ_p and ϕ_n , were defined as the angles between the positive x axis and the projections of the proton and neutron trajectories onto the x-y plane.

The raw data tapes were read and the spark coordinates for each of the magnetostrictive delay lines ("wands") were examined. Using the current value for the scaler reading of the second fiducial of each wand, the wand was checked for fiducials out the tolerance, noise before the first fiducial, and no second fiducial (unless there were two sparks). (It should be noted that these problems were rare, occurring in less than 0.5% of the triggers.) To minimize the effects of drifts, a new value for the fiducial separation was calculated every 50 events. There were no measureable drifts in most of the wands; in two wands the drift over the course of the experiment was 4 counts, corresponding to approximately 1 mm. Using the latest fiducial value, the position of each spark along a wand was calculated. At least one spark was required in each of the four pairs of chambers; otherwise the event was considered to be an accidental trigger and the event was rejected. Approximately 50% of the triggers were eliminated for this reason. Since the chambers were approximately 98% efficient, few elastics were eliminated in this step.

Using the surveyed positions of the center wires of each chamber, the x, y and z coordinates of all possible sparks (including "ghosts"*) were calculated. Ghosts were eliminated whenever possible by

* Ghosts are false spark coordinate pairs which arise when there are two or more sparks in a chamber. In the case of two sparks at positions (x_1, y_1) and (x_2, y_2) , there would be ghosts at positions (x_1, y_2) and (x_2, y_1) .

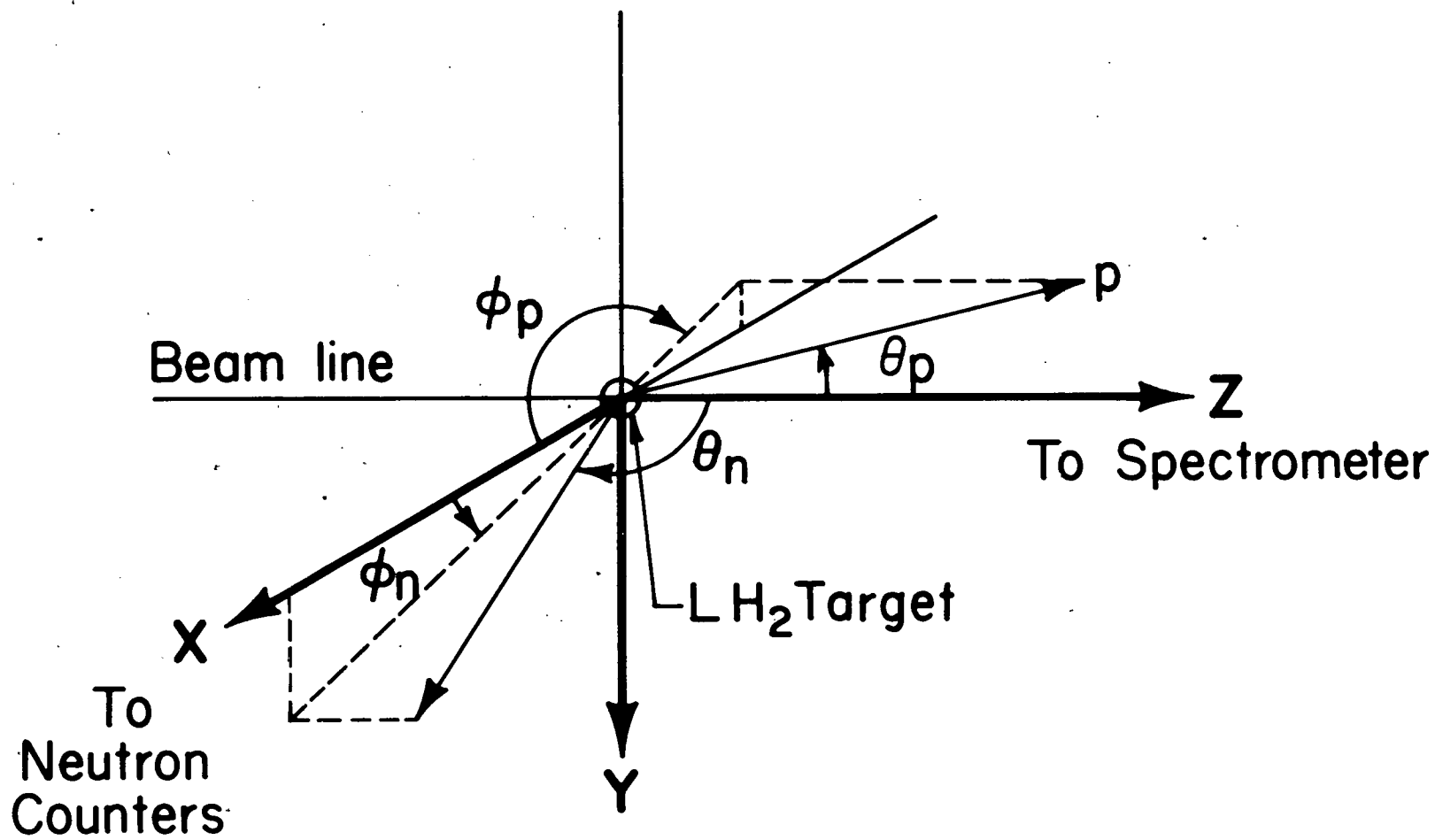


Figure 5.1

comparing the spark coordinates in the two chambers of a set. On each side of the magnet all possible track segments containing 4, 3 or 2 sparks were found. Each track was fit to a straight line. A spark was included in a track if it fell within 6 mm of the line defined by two other sparks in the track.

After all possible track segments on each side of the magnet were found, the front tracks were projected upstream to the target and downstream to the magnet aperture; those tracks missing the target by more than 5 mm or the magnet aperture by more than 15 mm were eliminated. The rear tracks were projected upstream to the magnet aperture and those tracks missing the aperture were eliminated. Both front and rear tracks were then projected to the center of the magnet. The two tracks were required to lie within $\Delta x = 20$ mm and $\Delta y = 20$ mm of each other. The difference in y slope, dy/dz , between the two lines was required to be less than 0.02, and the change in x slope, dx/dz , was required to be of the proper polarity for a positively charged particle.

Approximately 60% of the events survived the above cuts. Of these events, 98% had one complete trajectory through the spectrometer, 9% had two tracks, and 1% had three or more tracks. Information on the fitted tracks (including multiple solutions) was written on a secondary data tape along with all the neutron counter data for each event. All 1.1×10^5 events fit on one 2400 foot tape, written at 1600 bpi.

Table 5.1 lists the number of events eliminated by the various cuts, including the cuts described in the next section.

A modified version of the track reconstruction program was used to calculate the efficiency of each spark chamber. The runs were divided into three groups in order to study the time dependence

Table 5.1

NUMBER OF EVENTS ELIMINATED BY THE CUTS

(TARGET FULL RUNS ONLY)

	Number Eliminated (thousands)	Remaining Events (thousands)
Proton Arm (Chapter V-A)		
		330 (Triggers)
Too few sparks	156	174
Track segment in front of magnet misses target	13	161
Track segment in front of magnet misses magnet aperture	2	159
Track segment in rear of magnet misses magnet aperture	5	154
$y_{\text{front}} - y_{\text{rear}}$ at magnet center too large	35	119
$x_{\text{front}} - x_{\text{rear}}$ at magnet center too large	19	100
$(dy/dz)_{\text{front}} - (dy/dz)_{\text{rear}}$ at magnet center too large	0.2	100
$(dx/dz)_{\text{front}} - (dx/dz)_{\text{rear}}$ at magnet center too large	0.2	100
Neutron Arm (Chapter V-B)		
Too many neutron counters	3.5	96.5
No complete neutron counters	1.5	95.0
$\Delta\theta$ too large	41.0	54.0
$\Delta\phi$ too large	21.5	32.5
ΔTOF too large	7.5	25.0
$p_{\text{lab}} < 8 \text{ GeV}/c$ or $p_{\text{lab}} > 29 \text{ GeV}/c$	1.5	23.5 (Elasticity)

of the efficiencies. Only those events with a complete track through the whole spectrometer system and with three or more sparks in the track segment on the side in question were examined. As a function of position, the program counted the number of times a track passed through a given chamber without producing a spark. The inefficiency was defined as (number of misses) divided by (number of misses + number of hits). The inefficiency of the spark chamber system as a whole was

$$I = I_1 I_2 + I_3 I_4 + I_5 I_6 + I_7 I_8$$

where I_i is the inefficiency of chamber i , and $I_i I_{i+1}$ is the inefficiency of the chamber pair $(i, i+1)$. A plot of inefficiency versus position for a typical spark chamber pair is shown in Figure 5.2. The inefficiency increased with time for several of the chambers.

Despite the time and position dependence of the efficiencies of some of the chambers, the efficiency of the system as a whole was high and rather constant, because there were twice as many chambers as necessary. Under the worst conditions, the efficiency varied by 1% as a function of position. The overall efficiency for the three sets of runs was 99%, 98.5% and 98%. For purposes of normalization, the efficiency of the spark chamber system was taken to be $98.5\% \pm 1.5\%$.

As mentioned in Chapter III-B, two kinds of runs were made to check the alignment of the chambers: runs in which the center wires of the chambers were shorted, and runs in which the field in the spectrometer magnet was zero. A modification of the above program was used to analyze these runs.

In order to determine the exact relationship between the scaler readings of the second fiducial and of the center wire (which was surveyed and served as a position reference), a set of runs was made in which the center wire of each plane was connected to the center wire of the orthogonal plane and the chambers were pulsed. Since the scalers started at the leading edge of the first

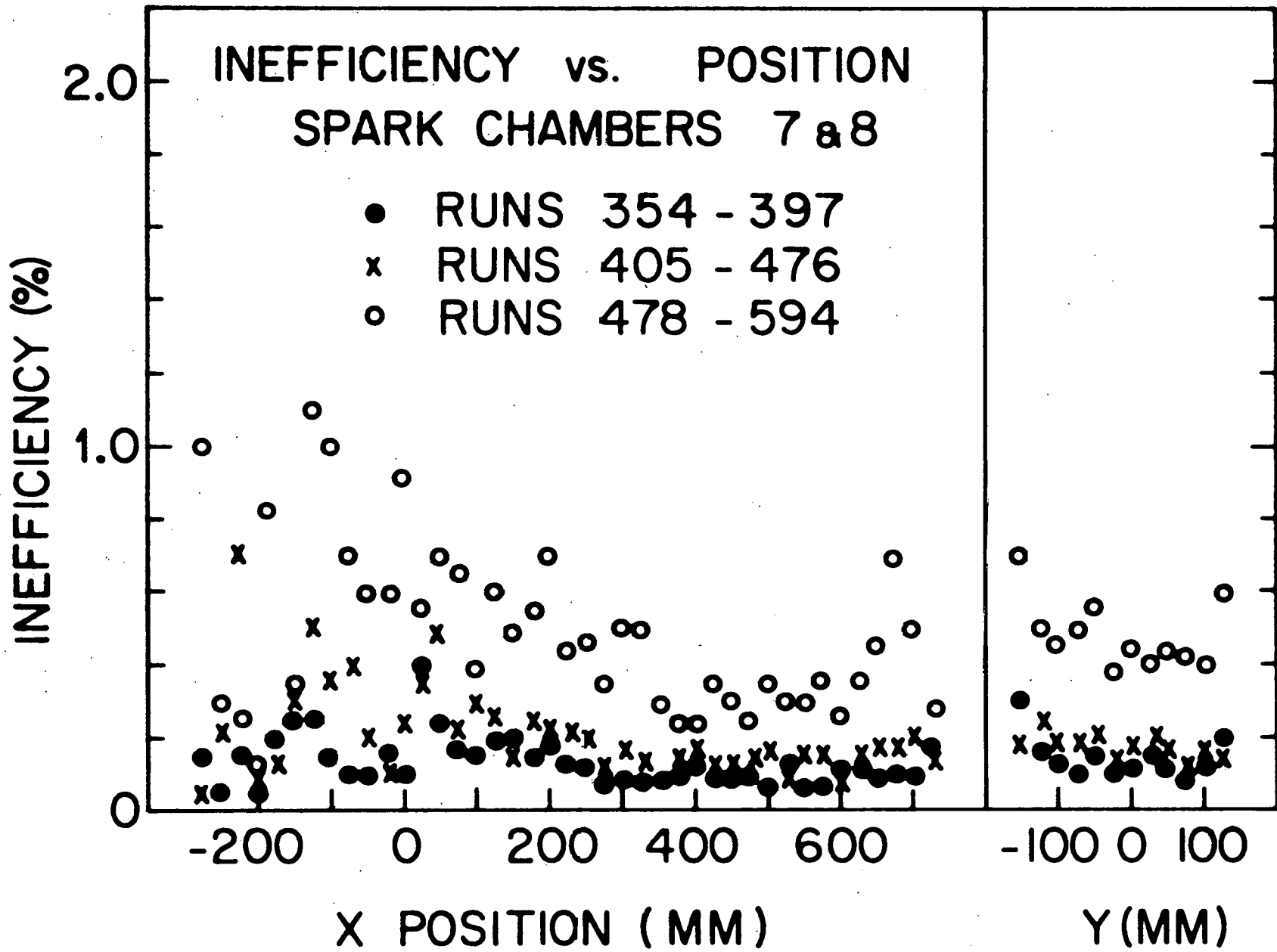


Figure 5.2

fiducial but stopped at the centers of the spark pulses and the second fiducial, the scaler reading of the center wire was expected to be slightly more than half the scaler reading of the second fiducial, the difference depending on the pulse widths (in this case, ~ 400 nsec, or 8 counts on a 20 MHz clock) and on the comparator levels. On the average, the center wire had a scaler reading which was 3.6 scaler units more than half the second fiducial scaler reading. Uncertainties due to varying pulse sizes were ± 2 units, or ± 0.5 mm.

A series of "straight through" runs were made using the beam to trigger the system in the usual way, but with the analyzing magnet turned off. If the chamber alignment was correct, all tracks should have been straight lines. The analysis program required at least three sparks (out of a possible four) in a track on each side of the magnet and then looked at the intersections of the front and rear tracks at the center of the magnet. The results for the front track minus the rear track are shown in Figure 5.3. Central values were $\Delta x = 0.5$ mm, $\Delta y = 1.5$ mm, $\Delta(dx/dz) = -.05$ mrad, and $\Delta(dy/dz) = .25$ mrad. The differences in x and y are not unexpected, since the surveying was good to at best ± 1 mm and possibly only ± 1.5 mm in the first set of chambers. The error in bending angle was sufficiently small that no correction was necessary when calculating the proton momentum in normal runs.

Chamber alignment was also checked during normal (magnet on) runs by examining the residuals for each chamber. A residual is the difference (x or y) between the measured position of a spark in a chamber and the fitted line from all the sparks on a track (for tracks with a spark in all four chambers on a given side of the magnet). Residuals in x varied from 0.1 mm to 0.6 mm; residuals in y varied from 0.2 mm to 1.3 mm. These residuals are of approximately the same size as the values of Δx and Δy obtained from the "straight through" runs and indicate that there were small errors (~ 1 mm) in the placement of some of the chambers. These errors were corrected by the methods described at the end of the next section.

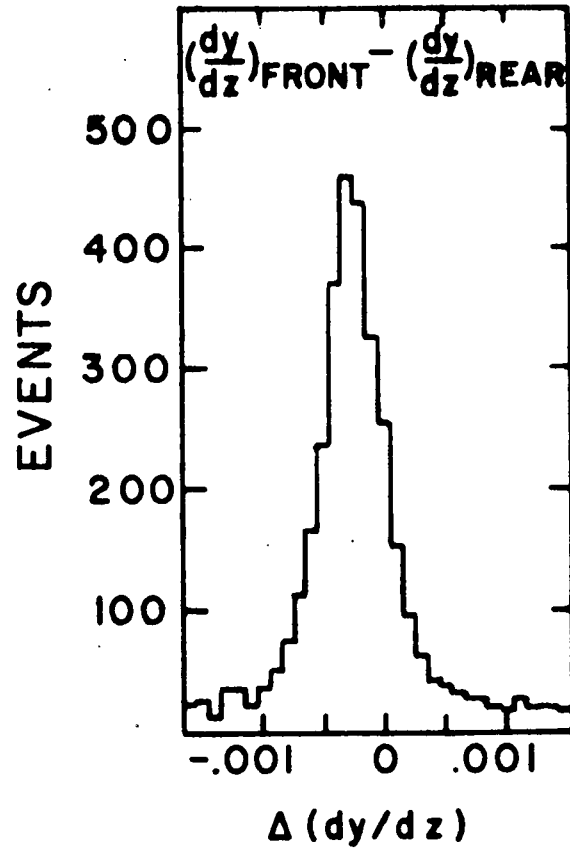
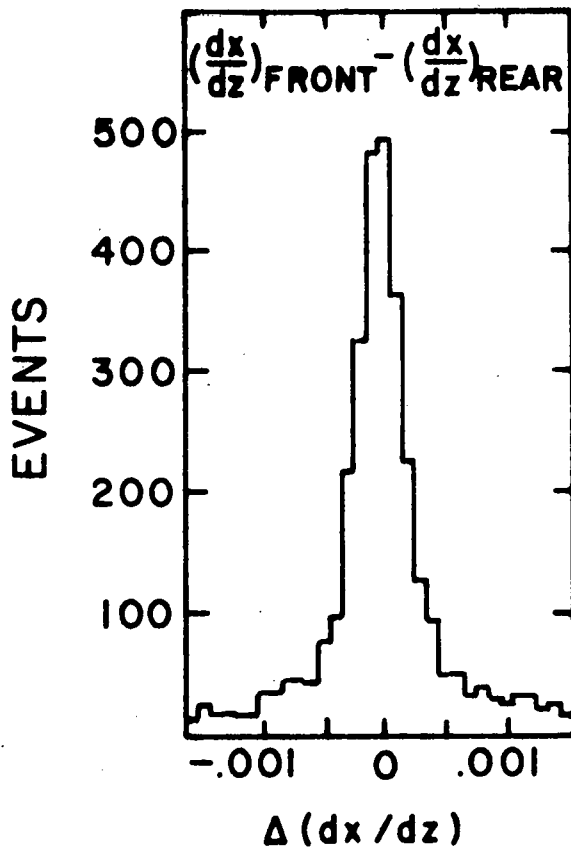
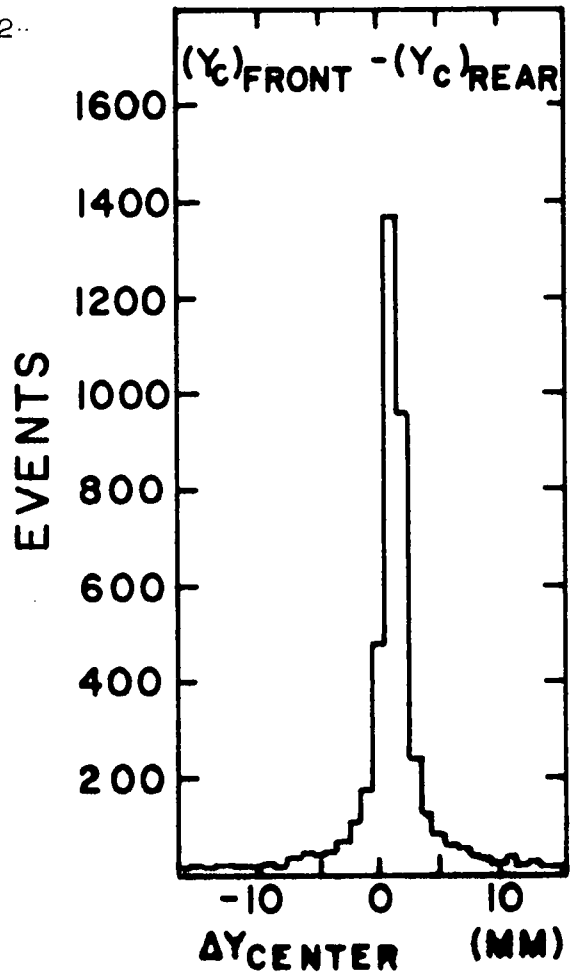
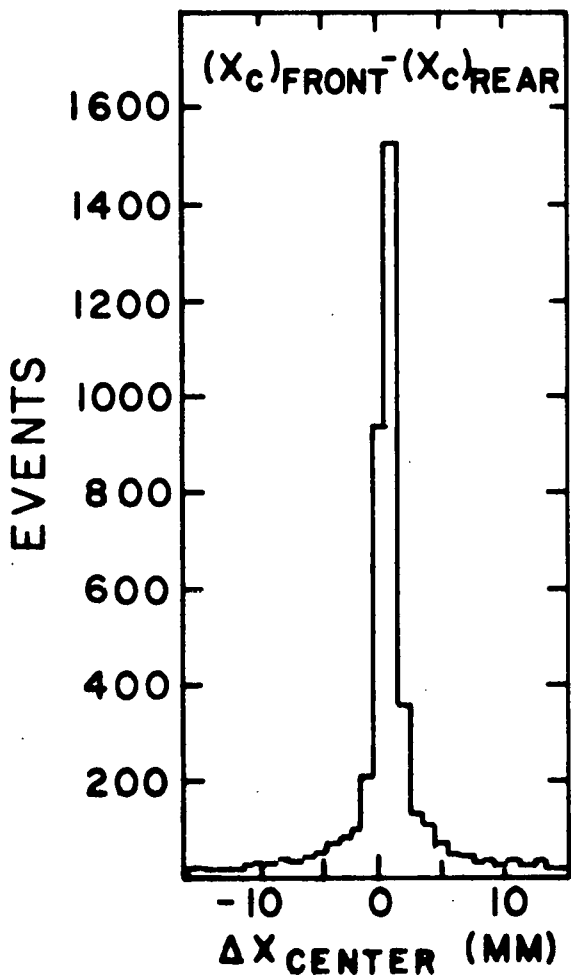


Figure 5.3

B. Kinematic Reconstruction and Selection of the Elastic Events

In the second stage of the analysis, the kinematics of each event was calculated from the information on the secondary data tape. A comparison of the information from the proton and the neutron arms of the experiment indicated whether each event was elastic. Various small corrections were applied to the data, as discussed at the end of this section.

The first step was to determine which neutron counter fired and whether the neutron counter information was analyzable. The latches for the two ends of each counter were examined, and the following criteria were used to choose the proper counter.

- (a) If both ends of only one counter fired, that counter was chosen.
- (b) If both ends of two counters fired (an odd and an even), the event was accepted, but the counter was chosen later, based on the proton information.
- (c) If more than one counter in a bank fired, that bank was rejected, since the timing and pulse height information for that bank was destroyed.
- (d) If both ends of several counters fired, but either the even or the odd bank had only one counter firing, that bank was chosen.
- (e) If there were no complete counters firing (both ends), the event was rejected.

If there were one or more useable neutron counters, the proton information was then examined. If there was more than one possible proton trajectory, each was treated separately. Small corrections were applied to the angles of the proton trajectories, as described later in this chapter. The positions and angles of the tracks on the two sides of the magnet were used to calculate the momentum of the proton,

$$p = \frac{e}{c} \frac{\int \vec{B} \cdot d\vec{l}}{\cos\psi (\sin\alpha_f - \sin\alpha_i)}$$

where ψ was the angle between the proton trajectory and the x-z plane; the angles α_i and α_f , measured in the x-z plane, were the initial and final angles of the trajectory with respect to the z axis ($\tan\alpha_i = (dx/dz)_{\text{front}}$, $\tan\alpha_f = (dx/dz)_{\text{rear}}$); and $\vec{B}(x,y,z)$ was the magnetic field. The field integral $\int \vec{B} \cdot d\vec{l}$ was approximated by its value along the line $x = y = 0$, and small corrections (typically less than 0.1%) were made to the momentum calculation based on a knowledge of $\Delta B/B_0$ (B_0 was the central field) as a function of x and y. Under the assumption that the event was elastic, the proton vector momentum was used to calculate the four-momentum transfer squared t, the neutron scattering angle θ_n , the neutron azimuthal angle ϕ_n , the neutron time of flight TOF, and the momentum of the incident neutron p_{lab} .

The program then used the neutron counter information to calculate θ_n , ϕ_n , and TOF. If there were two acceptable counters, as in case (b) above, the program calculated these quantities for both counters. There was one acceptable counter in 91% of the events and two acceptable counters in 4% of the events. In the other 5% of the events, there were either no complete neutron counters or too many counters.

The azimuthal angle of the neutron was $\phi_n = (y - y_t)/(x - x_t)$, where x and y were the coordinates of the neutron interaction in the neutron counter, and x_t and y_t were the coordinates of the interaction in the hydrogen target (obtained by projecting the proton back to the $z = 0$ plane in the target). The x coordinate in the counter was the perpendicular distance between the beam line and the center of the counter. The y coordinate was determined from the timing difference between the upper and lower photomultipliers of the counter:

$$y = (\tau - \tau_0) \cdot c/2 \quad ,$$

where τ was the timing difference for the event, τ_0 was the timing difference corresponding to $y = 0$ (measured in the light pulser runs described in Chapter III-D), and c was the speed of light in the counter (measured in the special counter runs described in Chapter III-D). Since τ_0 varied slowly with time, its value in the program was adjusted from run to run, as described later in this chapter.

The scattering angle θ_n of the neutron was essentially the average angle of the neutron counter (see Table 3.1), with a small correction based on the value of y . Since part of counter N_1 was outside the allowed angular range for elastic events, a smaller value of θ_n , corresponding to a point 1/4 of the distance across the face of the counter, was used for that counter.

The neutron time of flight TOF was determined by the timing difference between P_1 and the upper neutron counter photomultiplier, with corrections for the distance of P_1 from the target, the position of the interaction in the neutron counter, and the neutron counter pulse height. The time of flight was

$$\text{TOF} = (T - T_0) + (\text{TOF})_{\text{av}} - (\tau - \tau_0)/2 ,$$

where T was measured timing difference between P_1 and N_1^{up} for the event; T_0 was the measured timing difference corresponding to an "average" event from the light pulsers (see Chapter III-D); $(\text{TOF})_{\text{av}}$ was the time delay between the light pulser on P_1 and the light pulser on the center of the neutron counter for the "average" event (see Table 3.1); and τ and τ_0 were the up minus down timing differences as defined above. Small corrections to the time of flight are described later in this section.

For some events there was more than one possible proton track or more than one possible neutron counter. For those events, the best proton track and neutron counter were chosen by comparing the values of θ_n , ϕ_n , and TOF calculated from the proton information with the values measured by the neutron arm, for each possible combination of proton and neutron solutions. A χ^2 value was calculated, based on $\Delta\theta_n$,

$\Delta\phi_n$, and ΔTOF , and on estimated widths for these distributions; the set of proton and neutron solutions with the lowest χ^2 was chosen.

Elastic events were selected by the following procedure. The values of θ_n , ϕ_n , and TOF measured by the neutron counters were compared with the values calculated from the proton vector momentum assuming an elastic event. Figure 5.4 shows histograms of the differences in the three quantities, for counters N_1 through N_{15} combined. Histograms such as these were examined for each counter separately, and appropriate widths for loose cuts were determined. The three cuts were applied to each event, and those events surviving all three cuts were taken as the elastic sample. This sample contained some backgrounds.

Figure 5.5 shows the distributions of Figure 5.4, where the data in each distribution has been cut on the other two quantities. In order to determine the background as a function of t , distributions such as these were examined for each individual counter and for several ranges of t . Backgrounds were determined using the coplanarity ($\Delta\phi$) distribution, since it had the largest backgrounds.

Figure 5.6 shows the background determination for a typical neutron counter, N_5 . The cuts on $\Delta\phi$ are indicated by arrows. A flat background was assumed, with a value equal to the average number of counts per bin outside the cuts. The background for N_5 is indicated by a dashed line; the number of background counts inside the cuts is approximately 2.5% of the total events inside the cuts.

Figure 5.7 shows the backgrounds as a function of t . The backgrounds are largest at small $|t|$ because the slow neutrons corresponding to small $|t|$ require longer timing gates and higher neutron counter gains than the neutrons at larger $|t|$. Backgrounds increase at large $|t|$ ($\geq 0.6(\text{GeV}/c)^2$) because the number of inelastics increases as the angle with respect to the beam decreases and because the fast neutrons corresponding to large $|t|$ are difficult to separate from the inelastics by time of flight measurements.

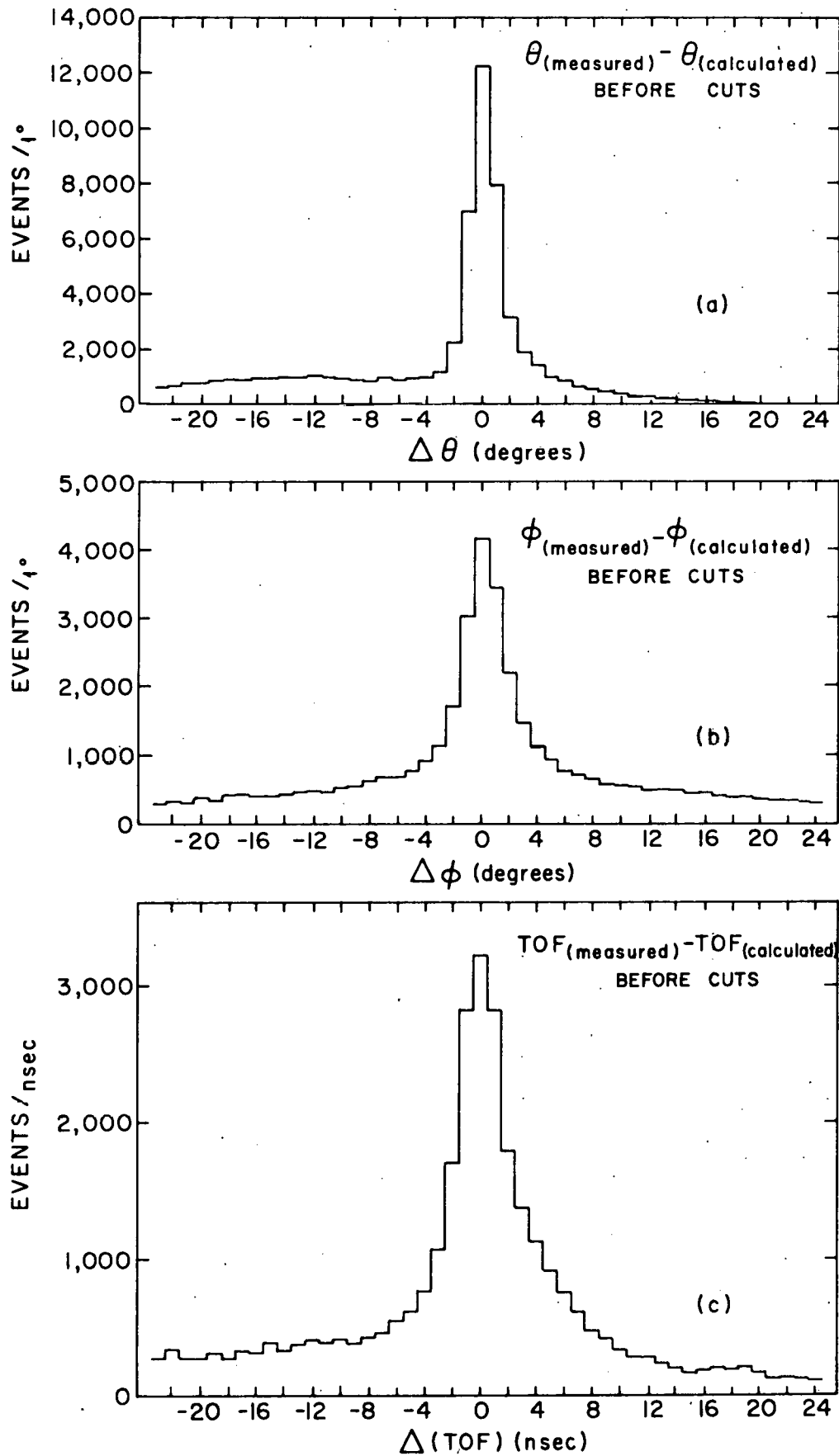


Figure 5.4

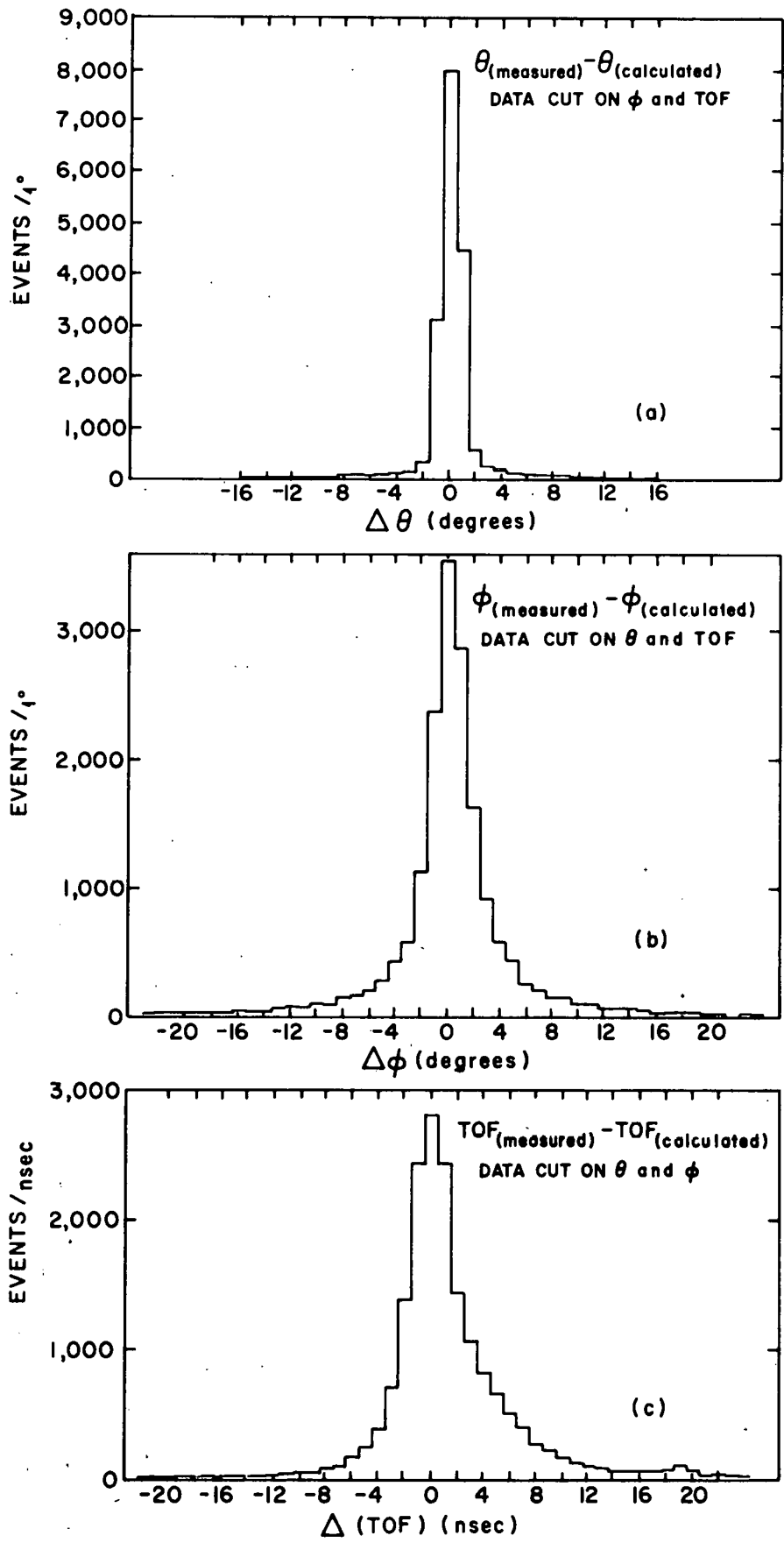


Figure 5.5

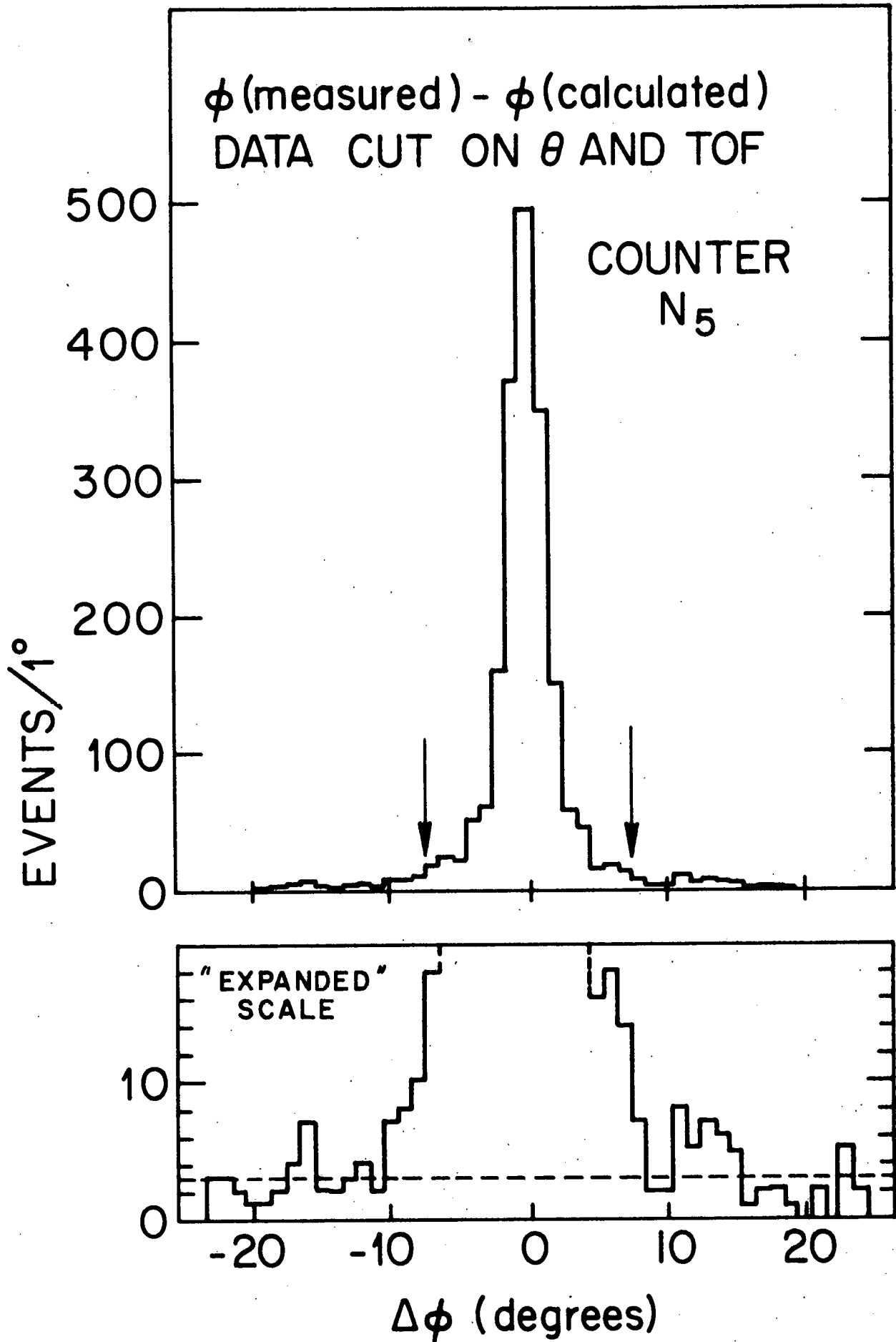


Figure 5.6

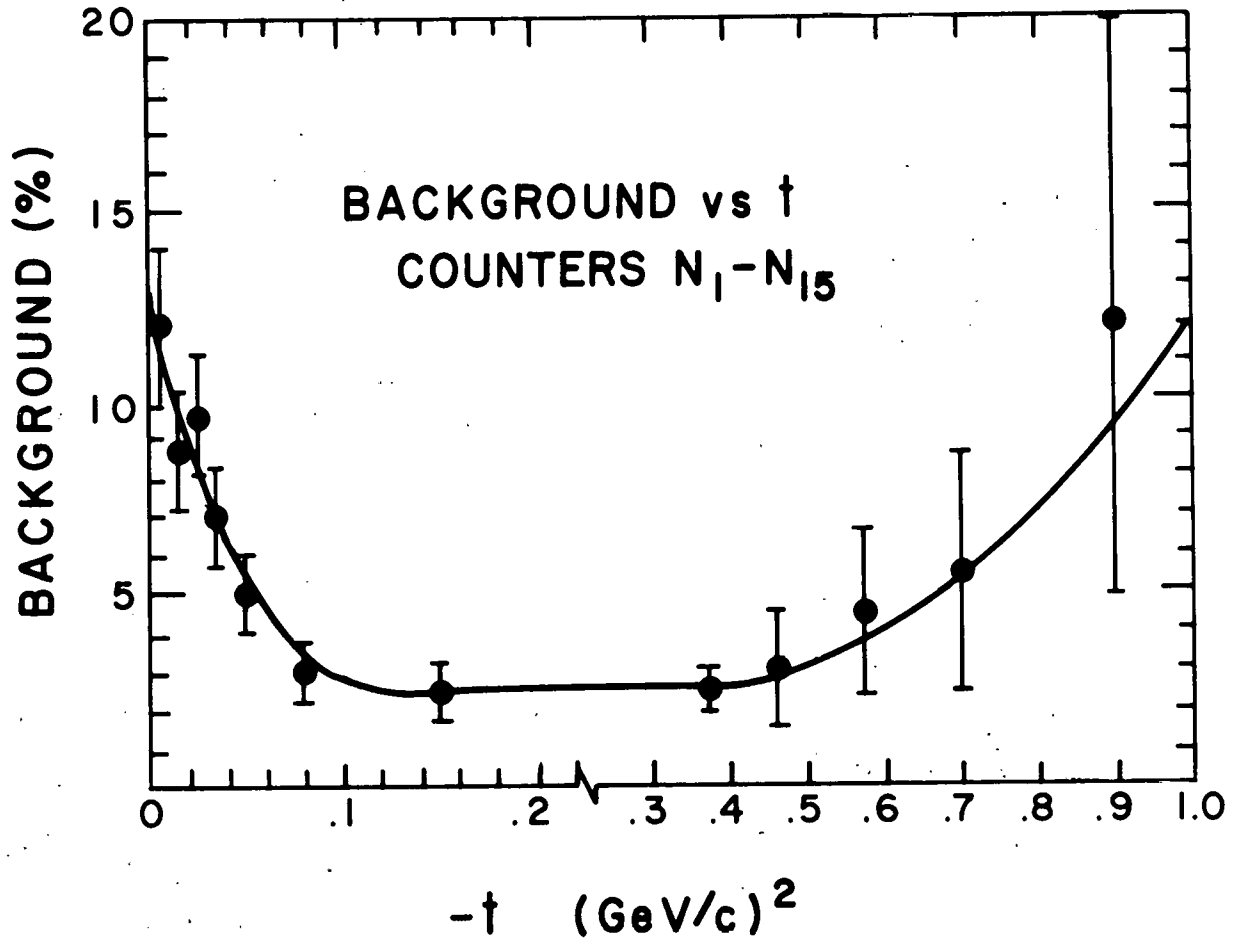


Figure 5.7

During the kinematic reconstruction several small corrections were made for the following systematic effects: (1) drifts in the up minus down timing over the course of the experiment; (2) a dependence of the measured neutron times of flight on neutron counter pulse height; (3) errors in the assumed lengths of some of the cables used as delays in the light pulser runs; (4) small errors in the assumed positions of the spark chambers. These corrections will now be discussed in more detail.

- (1) Up minus down timing: As described previously, a light pulser was placed at the center of each neutron counter. The up-down timing difference τ_0 corresponding to an interaction at the center of the counter was determined by pulsing the lamp. The values for τ_0 determined by this method were found to change slowly with time. Typical drifts over the several months of the experiment were 0.5 to 1 nsec. Corrections were made for these drifts.

After corrections were made for timing drifts, the dependence of up minus down timing (for the Pek lamp runs) on pulse height was examined. As can be seen in Figure 5.8., only N_1 had any significant dependence. Pulse height corrections to up minus down timing were made only for counter N_1 .

- (2) TOF versus pulse height: Neutron times of flight were measured relative to the Pek lamp runs described previously. The light pulsers had too small a pulse height range to provide a direct calibration of the pulse height corrections to TOF. It was therefore necessary to use the n-p scattering data to determine these corrections.

Pulse height corrections to the time of flight were determined by looking at the distributions in TOF (measured by the neutron counters) minus TOF (calculated from the proton vector momentum) as a function of pulse height.

UP MINUS DOWN DIGITIME READING

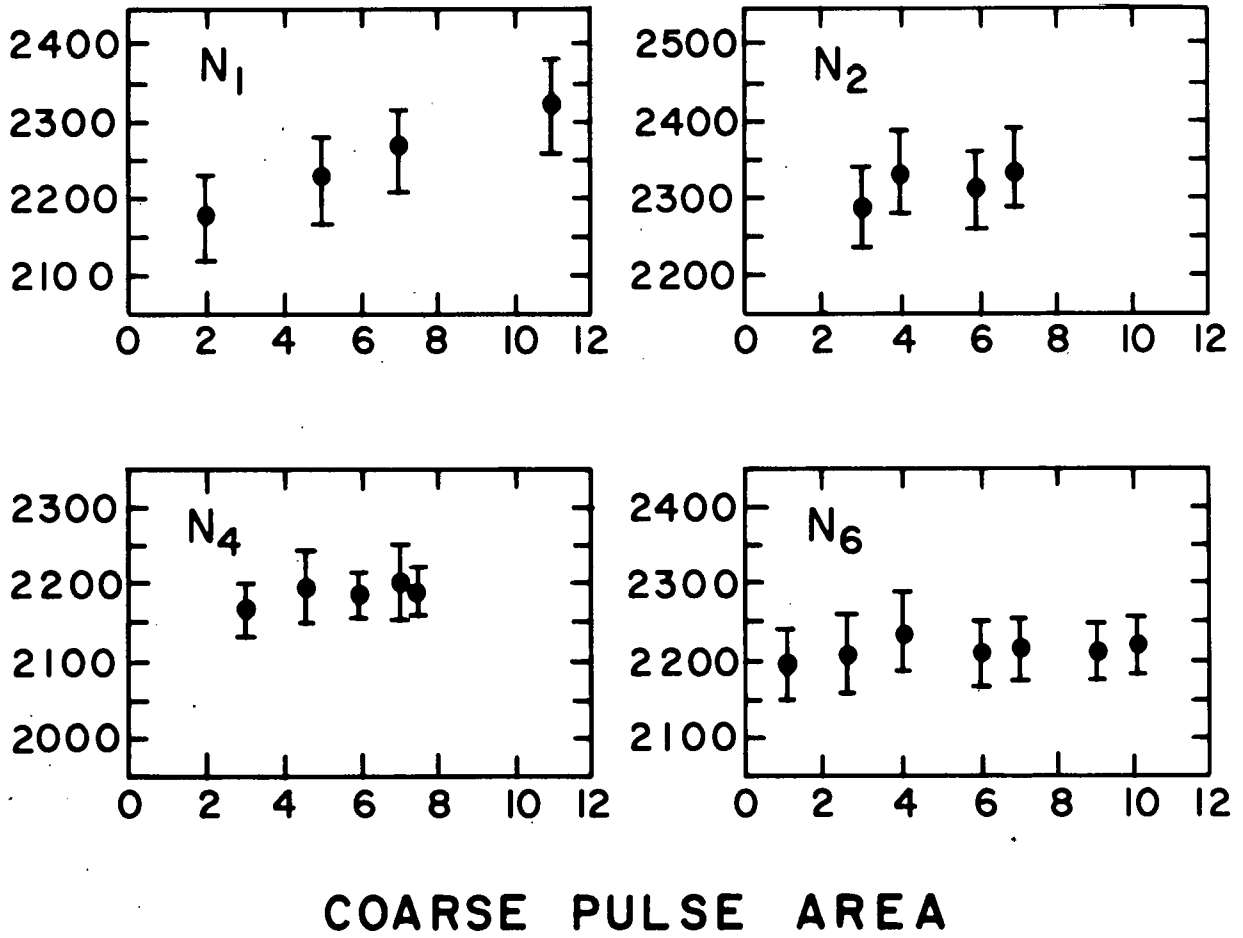


Figure 5.8

Since TOF (calculated) is independent of pulse height, the quantity Δ TOF will have the same pulse height dependence as TOF (measured). We can therefore determine the pulse height corrections to TOF (measured) by looking at the dependence of Δ TOF on pulse height. Figure 5.9 shows Δ TOF versus pulse height in various pulse area intervals (note that the pulse area is plotted on a logarithmic scale). The arrows show the average pulse height for the Pek lamp run which served as the time of flight reference. For counters N_3 through N_{15} , Δ TOF was approximately zero at the reference pulse height, as expected; for counters N_1 and N_2 , however, there was a discrepancy of several nanoseconds. The slopes of the Δ TOF versus pulse height curves were approximately the same for counters N_3 through N_{15} ; for counters N_1 and N_2 , however, the slopes were somewhat steeper.

The fact that counters N_1 and N_2 have nonzero values of Δ TOF at the reference pulse height has two possible explanations. One explanation is that there is a systematic timing error in the first two counters, probably due to an error in the length of the cables used in the Pek lamp timing runs. Another explanation is there is an error in the value of TOF (calculated) because of a small spark chamber misalignment. These two possibilities were investigated, as described in parts (3) and (4) below.

Pulse height corrections were made to each measured time of flight, based on the difference between the pulse area of the event and the reference pulse area for the neutron counter. As shown in Figure 5.9, the corrections were approximately linear in the logarithm of the pulse area.

- (3) Cable errors: Because of their length and the fact that they attenuated the Pek lamp pulses by approximately 30%, the timing cables used on N_1 and N_2 were subject to errors of approximately 2 nsec (see Figure 3.6). It was possible to check for systematic errors in the cables by comparing

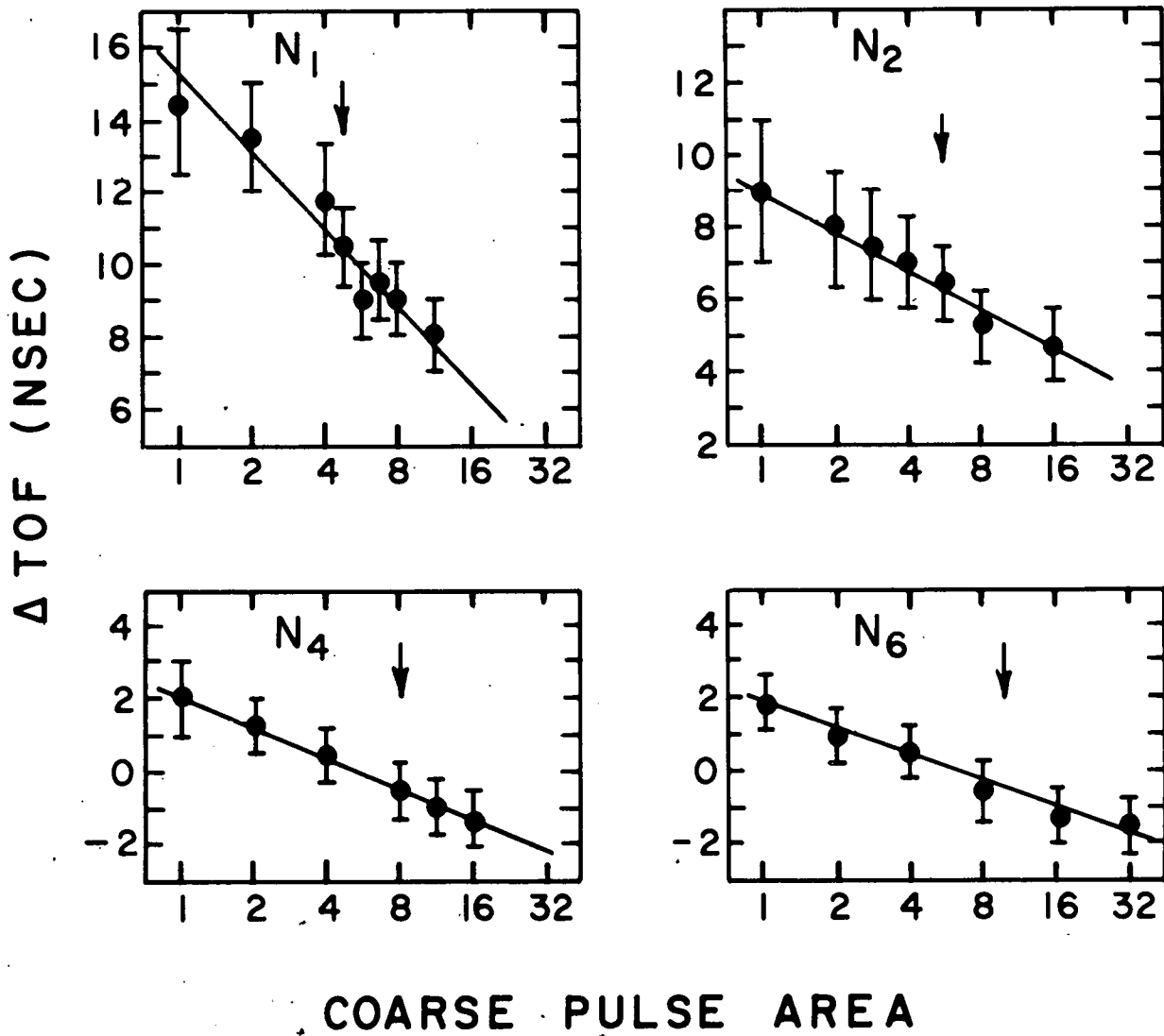


Figure 5.9

the measured times of flight in two adjacent counters for events with the same calculated times of flight (calculated from the proton information). It was found that counters N_1 and N_2 gave the same measured times of flight in their regions of overlap, while counter N_3 gave measured times of flight which were approximately 2 nsec shorter than those of N_2 (for the same calculated TOF). On the basis of this evidence, 2 nsec were subtracted from all the measured times of flight for counters N_1 and N_2 .

- (4) Spark chamber position errors. The runs with the spectrometer magnet turned off indicated that errors in the bending angle of the proton were negligible. However, due to surveying uncertainties, it was still possible for the chambers to be misaligned in such a way that there could be a systematic error in the scattering angle θ_p . Data from elastic n-p scattering events used to determine the size of the angular correction (if any) to be made to the proton trajectory in front of the magnet.

The correction to be made to θ_p was determined in the following way. A systematic error in θ_p will cause an error in TOF (calculated). This error in TOF (calculated) will increase as the incident neutron momentum increases, since, for a given neutron TOF, the proton scattering angle becomes smaller as p_{lab} increases. By examining the dependence of TOF (calculated) on p_{lab} , for fixed TOF (measured), it is possible to calculate the size of the systematic error in θ_p .

The dependence of TOF (calculated) on p_{lab} was examined for several values of TOF (measured) in counters N_1 and N_2 . The value of the correction to θ_p determined in this way was 0.2 mrad. When this correction and that of part (3) were applied to the data, the Δ TOF versus pulse area distributions for N_1 and N_2 were centered approximately

around zero and had the same slope as the distributions for counters $N_3 - N_{15}$. This correction, which is of approximately the same size as the angular resolution of the spectrometer, had a negligible effect on the shape of the angular distributions.

C. Monte Carlo

The acceptance of the apparatus as a function of the incident neutron momentum p_{lab} and the square of the four-momentum transfer t was calculated using a Monte Carlo computer program simulating the geometry of the apparatus. The target interaction point, the incident neutron momentum, the azimuthal angle of the interaction, and the four-momentum transfer squared were randomly chosen. The proton and neutron were then followed through the system, and those events were eliminated where one of the particles was outside the solid angle of the apparatus. A weight was assigned to each surviving event, depending on the efficiency of the neutron counter (this measurement is described in Appendix B). The probability that each recoil neutron would reach a neutron counter without interacting with the material between the liquid hydrogen target and the neutron counter was calculated using standard tables of neutron - nuclei total cross sections.⁽⁵⁶⁾ Each event was weighted by this probability, which was typically 90 to 99%, depending on the energy of the neutron. All important information on each surviving event was written on magnetic tape. The program made 1.3×10^6 attempts with the full magnetic field (18 KG) and 7×10^5 attempts with the reduced field (12 KG), of which approximately 25% survived.

The magnetic tape was then read and such effects as multiple coulomb scattering and measurement uncertainties were put in. The Monte Carlo output was divided into bins of p_{lab} and t , and the average acceptance in each bin was determined. The acceptance

was defined as

Acceptance (p , t) = (weighted number of surviving Monte Carlo events in a given p and t interval) / (number of attempts into that interval).

Typical values of the acceptance were 1 to 2%.

D. Normalization

The absolute normalization consisted of the following steps.

- (a) The total number of neutrons on the liquid hydrogen target as a function of the number of monitor counts was measured using a total absorption spectrometer, described in Appendix C.
- (b) The shape of the neutron spectrum was determined from a separate experiment, described in Appendix D. This information was combined with that of part (a) to get the number of neutrons per monitor count in each interval of incident neutron momentum.
- (c) The absolute cross sections were found by combining the neutron flux measurements, the Monte Carlo acceptance calculations, and the data on the number of events as a function of p_{lab} and t. Various kinds of corrections were made to the cross sections.

The differential cross sections are given by the following formula:

$$\frac{d\sigma}{dt}(p,t) = \frac{\text{Events}(p,t)}{\text{Acceptance}(p,t)} \times \frac{1}{\text{Protons} \cdot \text{Neutrons}(p)}$$

where

Events = the number of events in the t and p_{lab} interval

Acceptance = the average acceptance in the t and p_{lab} interval (described in Section C)

Neutrons = the number of neutrons incident on the liquid hydrogen target in the given p_{lab} interval

Protons = the number of protons in the target within
the limits of the neutron beam.

The following corrections were applied to the cross sections.
Most of these corrections have been described previously.

- (a) Background subtractions of 2.5% to 13% were made.
- (b) The cross sections were increased by 1.5% to correct for spark chamber inefficiencies.
- (c) A target empty subtraction of 1.5% was made.
- (d) Some good events were lost because there were extra neutron counters in the trigger which destroyed the timing and pulse height information. A correction of 3.3% was made for this rate effect.
- (e) Due to the high counting rates in the anticounters, approximately 5% of the good events were vetoed. A correction was made for this effect.

Cross sections were calculated separately for runs with the magnetic field at 18 KG and at 12 KG. The cross sections measured with the two different fields agreed very well. The final cross sections, presented in Chapter VI, are a weighted average of the two cross sections.

CHAPTER VI. PRESENTATION OF RESULTS

This chapter presents the results of the measurement of elastic neutron proton charge exchange cross sections. Part A presents the cross sections and discusses the errors; part B discusses the energy dependence of the cross sections; and part C compares the cross sections with the current models. Some concluding remarks are made in part D.

A. Cross Sections and Errors

The cross sections measured in this experiment are shown in Figures 6.1 through 6.9 and are tabulated in Tables 6.1 through 6.9. The data were divided into 9 regions of incident neutron momentum, with approximately the same number of events in each region. The errors shown include statistical errors and all systematic errors except uncertainties in the neutron flux.

The relative systematic errors are the following:

- (a) Uncertainties in the background subtraction: 0.5 to 1.5%.
- (b) Uncertainties in the position dependence of the spark chamber efficiencies: 1.5%.
- (c) Uncertainties in the measured neutron counter efficiencies: 5% over most of the t range (0.006 to 1.0 $(\text{GeV}/c)^2$); 10% from 0.004 to 0.006 $(\text{GeV}/c)^2$; 30% from 0.002 to 0.004 $(\text{GeV}/c)^2$.
- (d) Uncertainties in the corrections made to the neutron efficiencies for scattering of neutrons from one counter to another or from the walls of the counter into the counter (see Appendix B): 3%.

In addition to the relative errors shown in the figures, there are uncertainties which affect the absolute normalization of the cross sections but do not affect the shape of the cross sections as a function of t . The absolute systematic errors are the following:

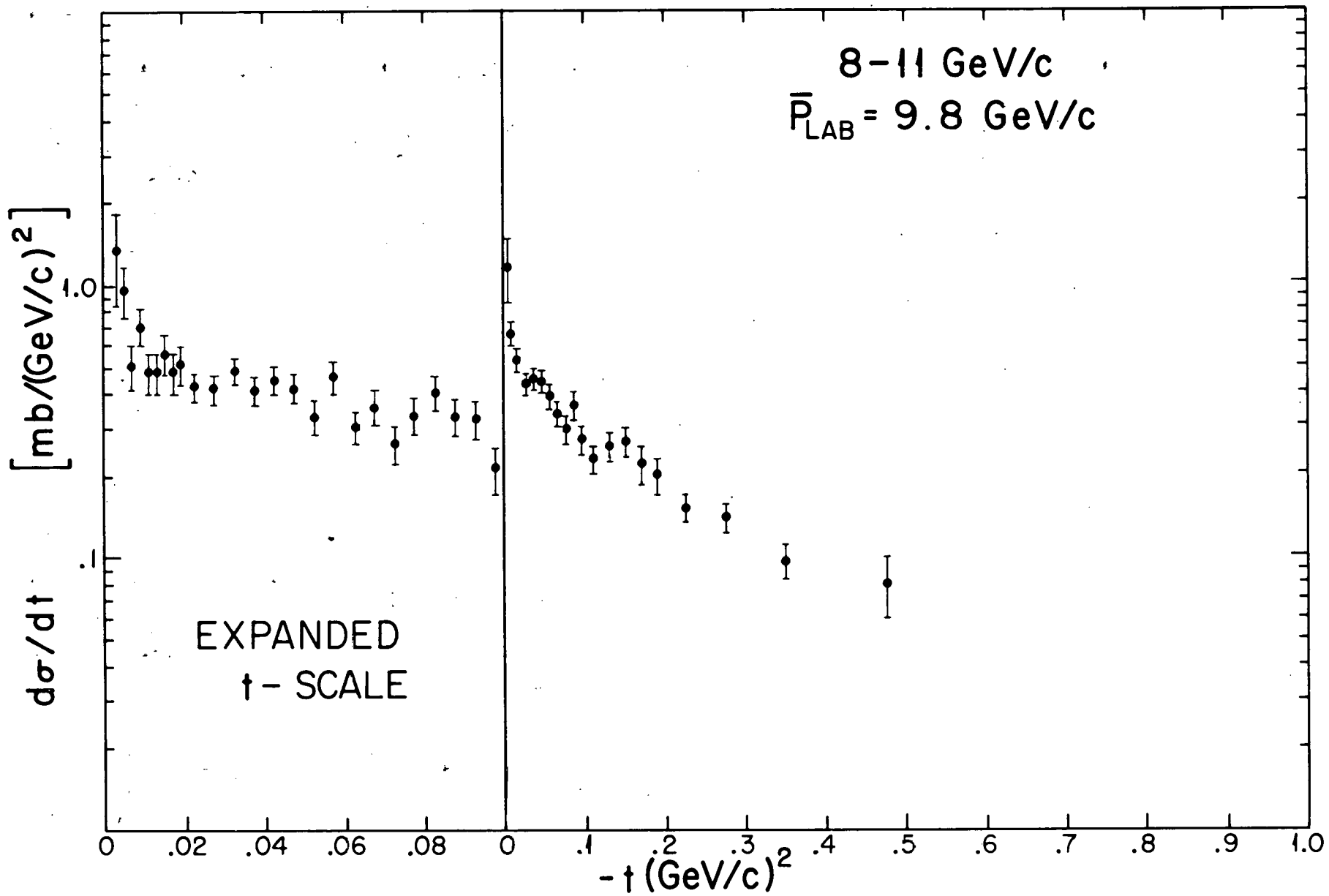


Figure 6.1

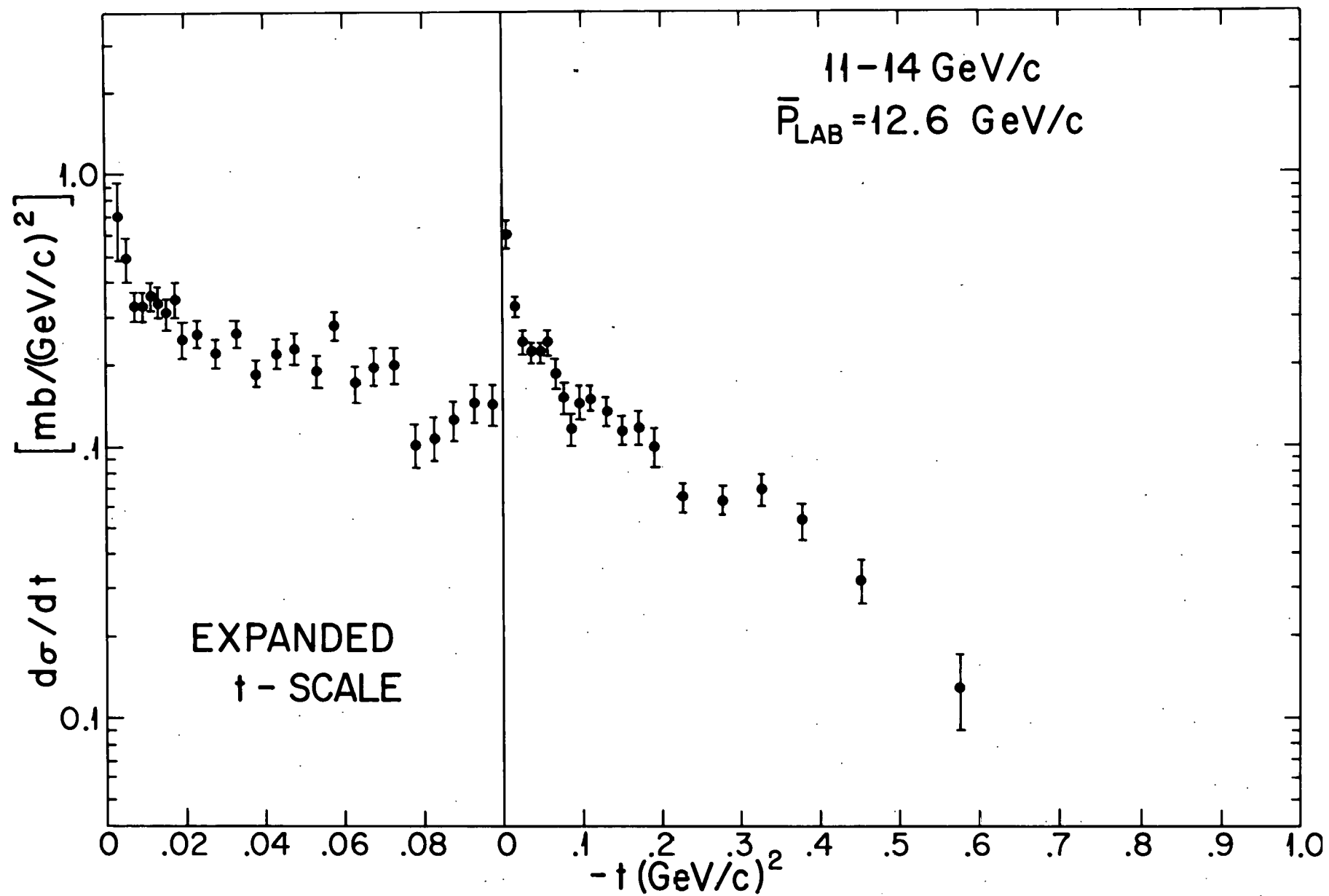


Figure 6.2

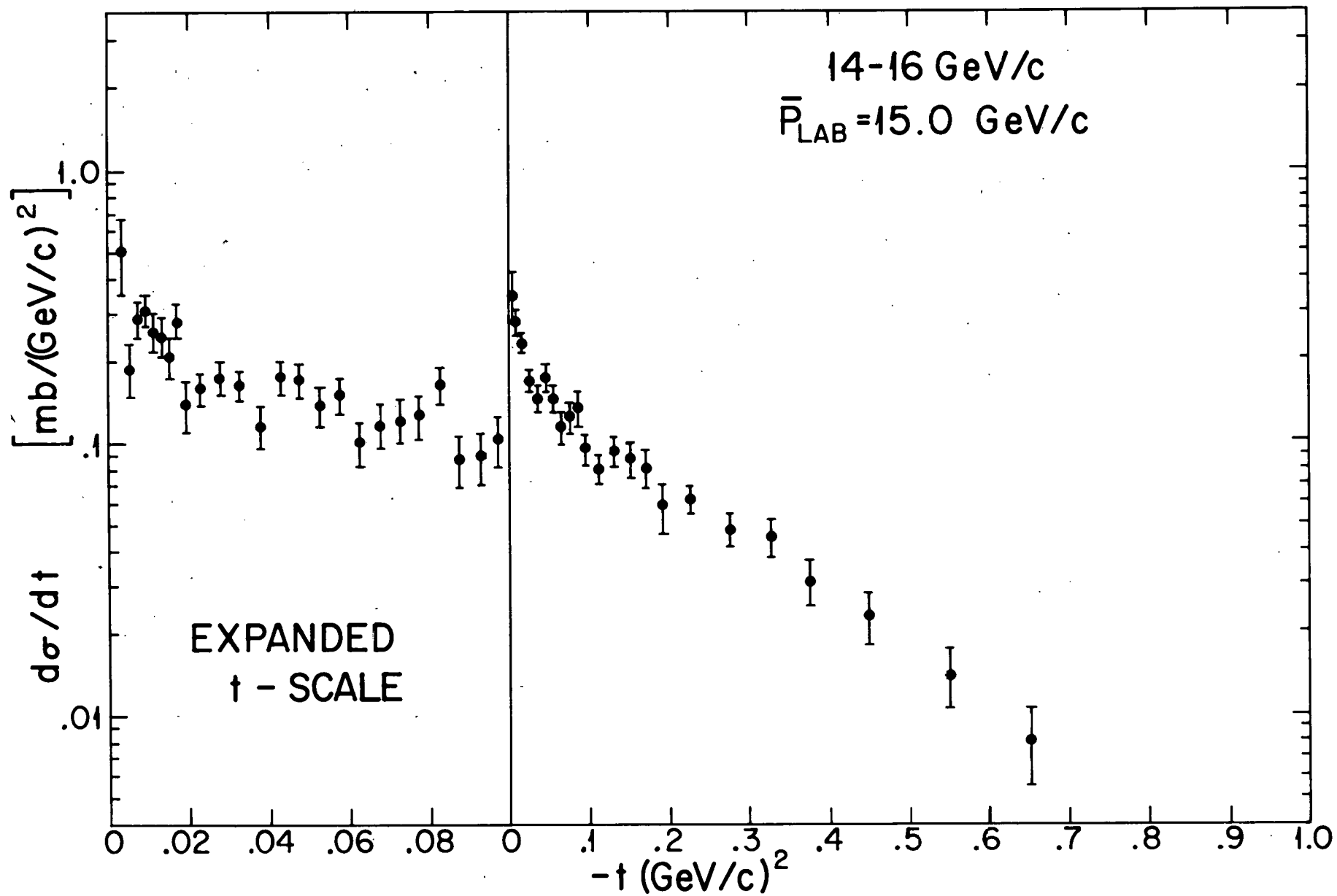


Figure 6.3

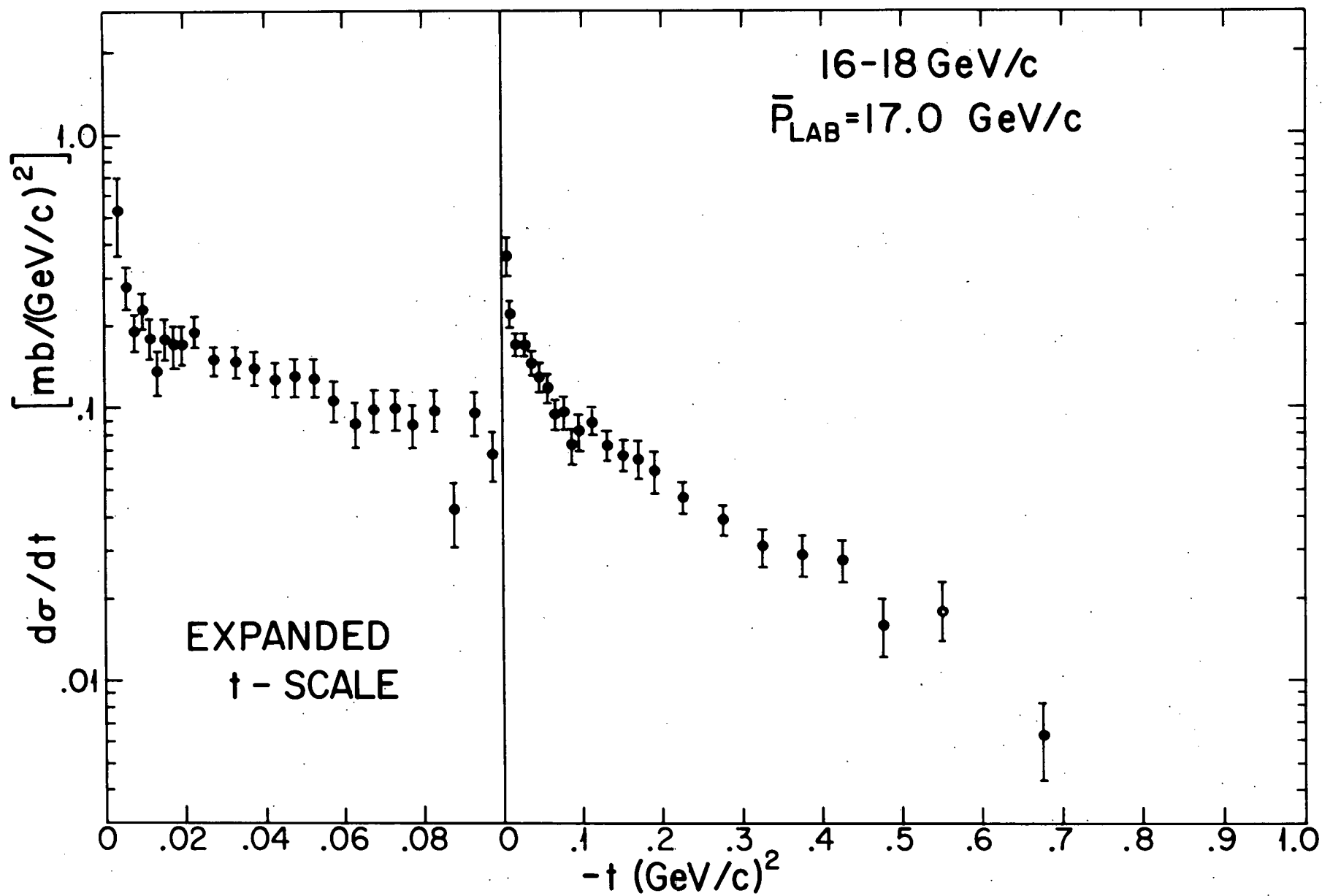


Figure 6.4

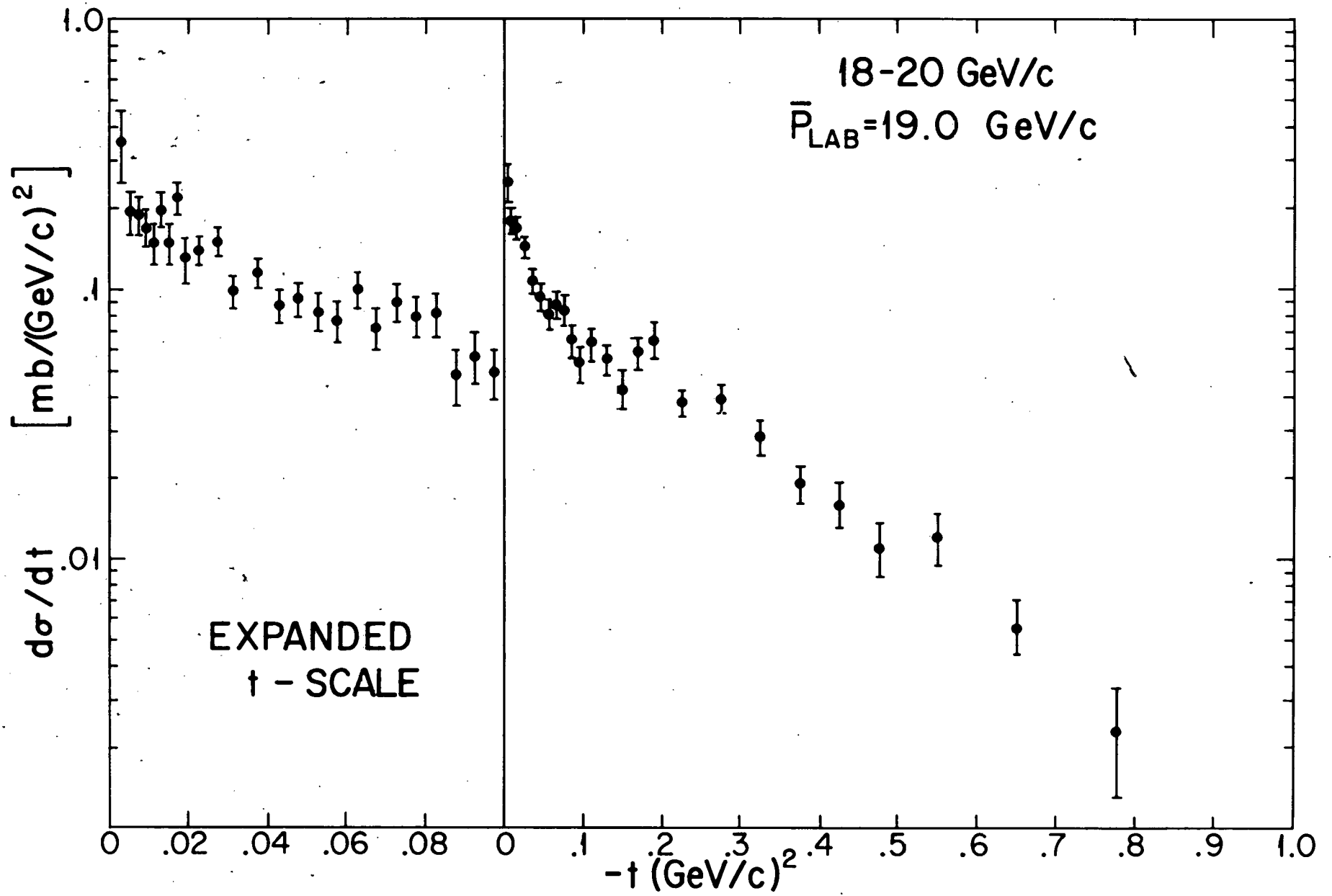


Figure 6.5

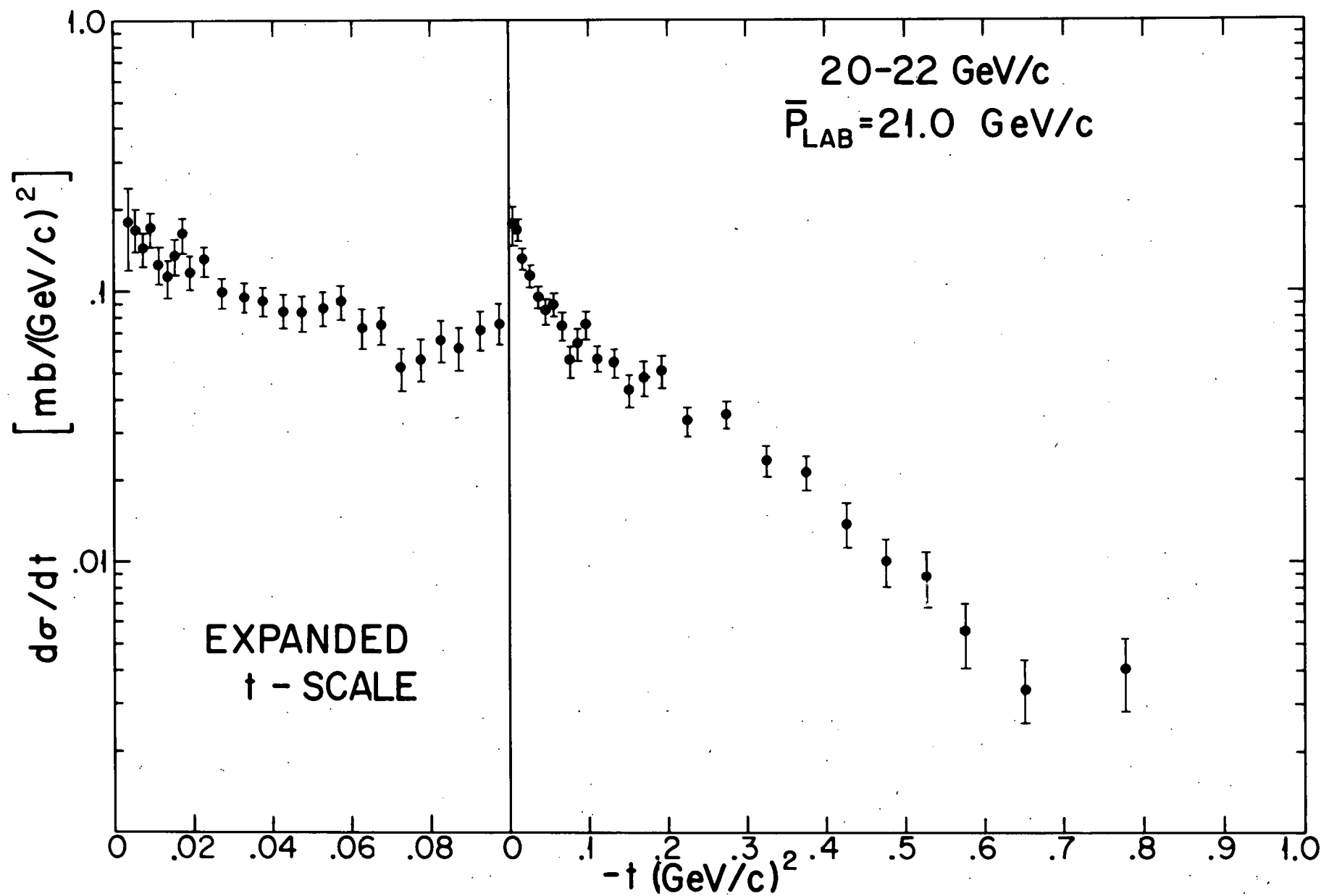


Figure 6.6

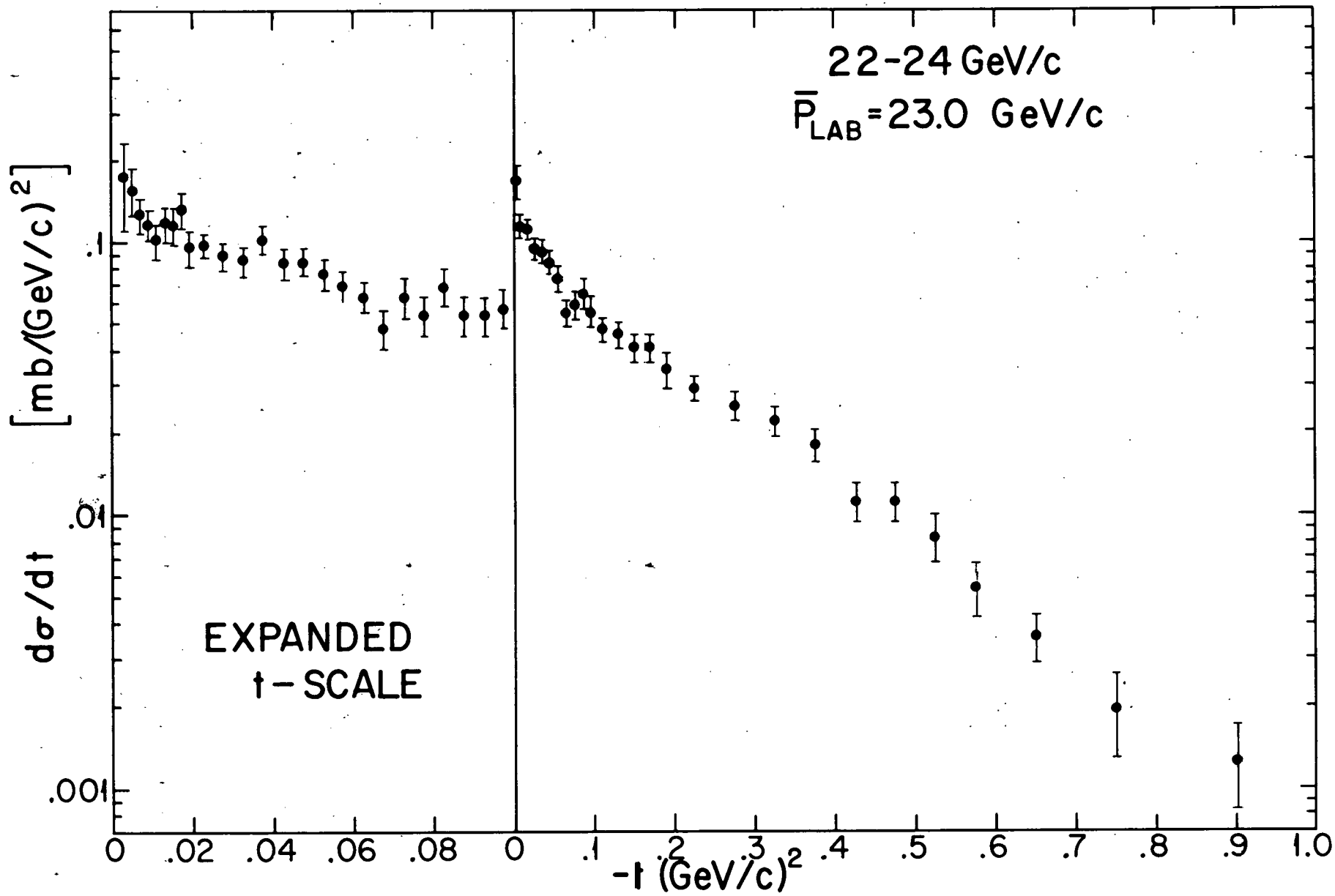


Figure 6.7

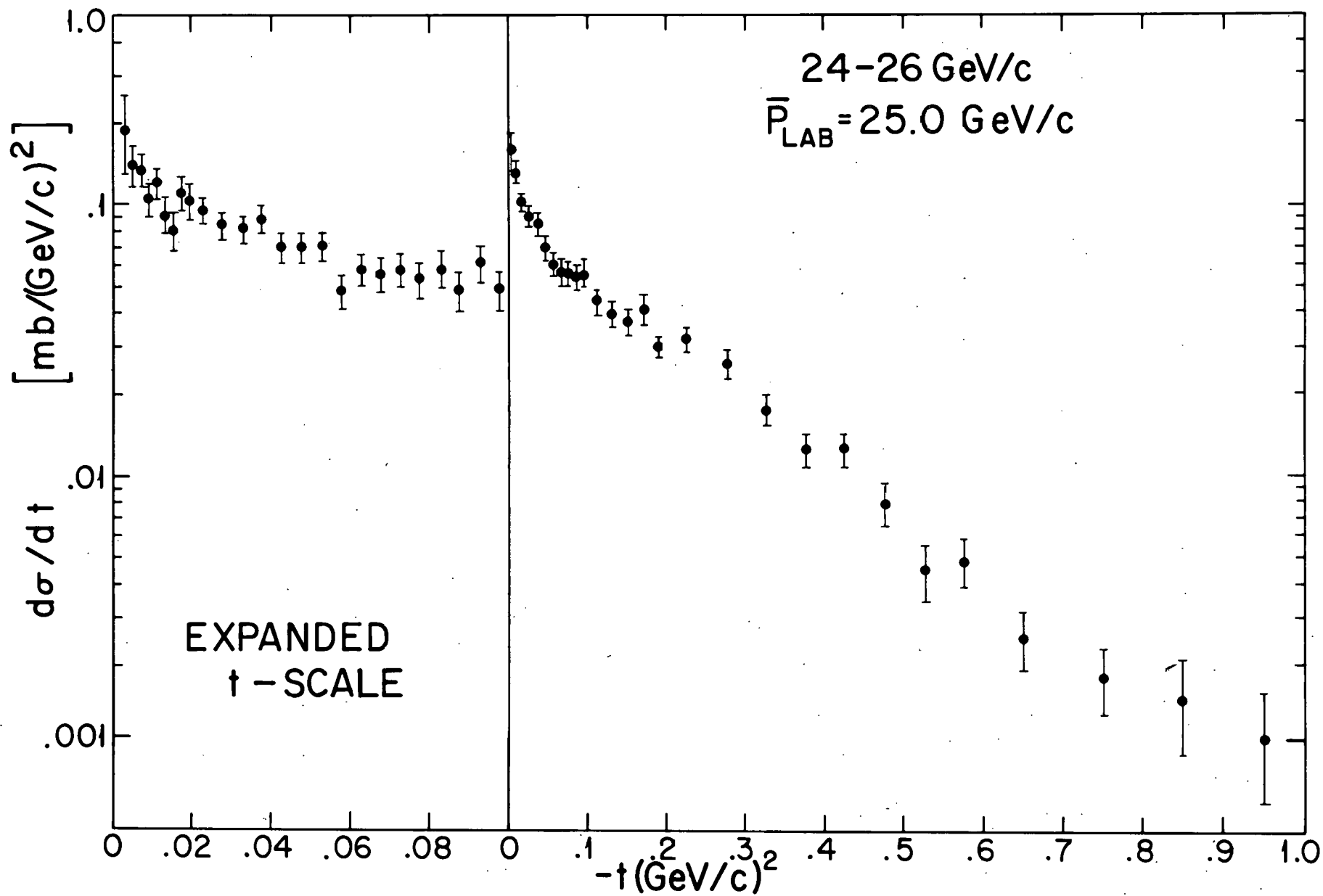


Figure 6.8

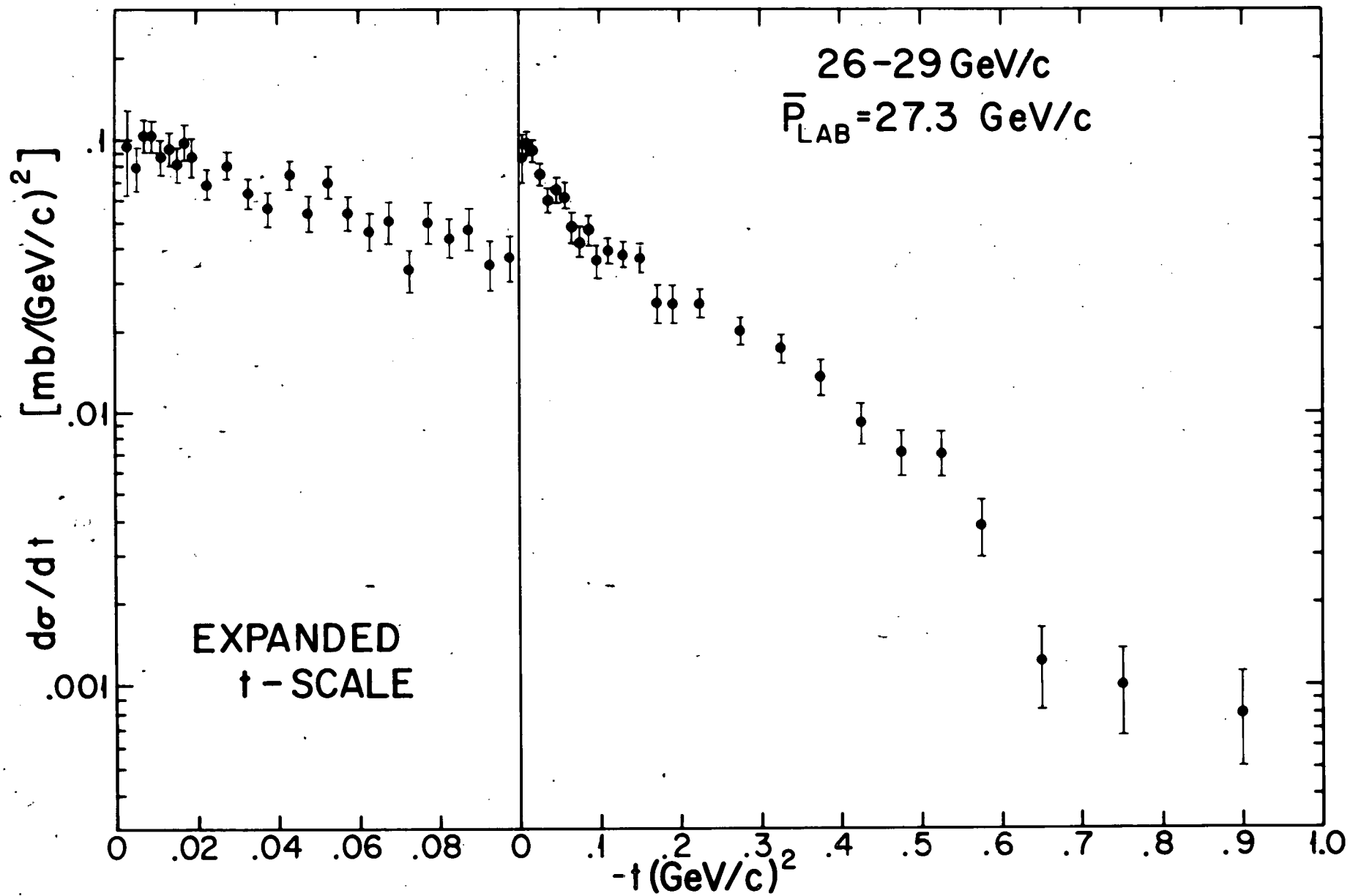


Figure 6.9

Table 6.1

DIFFERENTIAL CROSS SECTION



Incident neutron momentum = 8.0 to 11.0 GeV/c

Average incident neutron momentum = 9.8 GeV/c

Number of events = 2462

Absolute normalization uncertainty = 15.8 %

$ t $ [(GeV/c) ²]	$d\sigma/dt$ [mb/(GeV/c) ²]	Error	$ t $ [(GeV/c) ²]	$d\sigma/dt$ [mb/(GeV/c) ²]	Error
0.003	1.3400	0.4810	0.110	0.2330	0.0260
0.005	0.9740	0.2120	0.130	0.2540	0.0290
0.007	0.5080	0.0930	0.150	0.2660	0.0350
0.009	0.7020	0.1100	0.170	0.2210	0.0340
0.011	0.4790	0.0830	0.190	0.2010	0.0310
0.013	0.4800	0.0820	0.225	0.1510	0.0180
0.015	0.5650	0.0880	0.275	0.1400	0.0180
0.017	0.4780	0.0800	0.350	0.0969	0.0129
0.019	0.5190	0.0810	0.475	0.0789	0.0209
0.022	0.4310	0.0490			
0.027	0.4160	0.0480			
0.032	0.4870	0.0540			
0.037	0.4130	0.0490			
0.042	0.4490	0.0530			
0.047	0.4240	0.0520			
0.052	0.3270	0.0450			
0.057	0.4560	0.0560			
0.063	0.3010	0.0430			
0.067	0.3640	0.0500			
0.072	0.2580	0.0410			
0.077	0.3330	0.0490			
0.082	0.3970	0.0550			
0.087	0.3300	0.0490			
0.092	0.3200	0.0490			
0.097	0.2130	0.0390			

Table 6.2

DIFFERENTIAL CROSS SECTION



Incident neutron momentum = 11.0 to 14.0 GeV/c

Average incident neutron momentum = 12.6 GeV/c

Number of events = 2887

Absolute normalization uncertainty = 10.2 %

$ t $ [(GeV/c) ²]	$d\sigma/dt$ [mb/(GeV/c) ²]	Error	$ t $ [(GeV/c) ²]	$d\sigma/dt$ [mb/(GeV/c) ²]	Error
0.003	0.7150	0.2300	0.110	0.1490	0.0150
0.005	0.4890	0.0850	0.130	0.1340	0.0150
0.007	0.3280	0.0440	0.150	0.1140	0.0140
0.009	0.3290	0.0430	0.170	0.1160	0.0160
0.011	0.3610	0.0450	0.190	0.0983	0.0155
0.013	0.3400	0.0450	0.225	0.0651	0.0080
0.015	0.3060	0.0420	0.275	0.0630	0.0082
0.017	0.3510	0.0490	0.325	0.0698	0.0092
0.019	0.2490	0.0390	0.375	0.0533	0.0084
0.022	0.2610	0.0280	0.450	0.0319	0.0059
0.027	0.2230	0.0250	0.575	0.0129	0.0039
0.032	0.2620	0.0290			
0.037	0.1840	0.0230			
0.042	0.2160	0.0260			
0.047	0.2310	0.0280			
0.052	0.1930	0.0260			
0.057	0.2820	0.0340			
0.063	0.1720	0.0250			
0.067	0.1960	0.0270			
0.072	0.1970	0.0270			
0.077	0.1020	0.0190			
0.082	0.1070	0.0190			
0.087	0.1260	0.0210			
0.092	0.1460	0.0230			
0.097	0.1420	0.0240			

Table 6.3

DIFFERENTIAL CROSS SECTION



Incident neutron momentum = 14.0 to 16.0 GeV/c

Average incident neutron momentum = 15.0 GeV/c

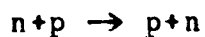
Number of events = 1966

Absolute normalization uncertainty = 8.7 %

$ t $ [(GeV/c) ²]	$d\sigma/dt$ [mb/(GeV/c) ²]	Error	$ t $ [(GeV/c) ²]	$d\sigma/dt$ [mb/(GeV/c) ²]	Error
0.003	0.5140	0.1690	0.110	0.0803	0.0105
0.005	0.1860	0.0400	0.130	0.0932	0.0118
0.007	0.2870	0.0450	0.150	0.0873	0.0122
0.009	0.3070	0.0430	0.170	0.0811	0.0131
0.011	0.2630	0.0390	0.190	0.0590	0.0116
0.013	0.2500	0.0390	0.225	0.0621	0.0077
0.015	0.2070	0.0340	0.275	0.0482	0.0069
0.017	0.2810	0.0440	0.325	0.0447	0.0069
0.019	0.1410	0.0200	0.375	0.0306	0.0057
0.022	0.1610	0.0210	0.450	0.0229	0.0049
0.027	0.1740	0.0220	0.550	0.0139	0.0034
0.032	0.1640	0.0220	0.650	0.0079	0.0026
0.037	0.1160	0.0180			
0.042	0.1740	0.0240			
0.047	0.1720	0.0250			
0.052	0.1370	0.0220			
0.057	0.1480	0.0230			
0.063	0.1010	0.0180			
0.067	0.1170	0.0210			
0.072	0.1220	0.0220			
0.077	0.1250	0.0220			
0.082	0.1630	0.0260			
0.087	0.0871	0.0187			
0.092	0.0903	0.0194			
0.097	0.1030	0.0210			

Table 6.4

DIFFERENTIAL CROSS SECTION



Incident neutron momentum = 16.0 to 18.0 GeV/c

Average incident neutron momentum = 17.0 GeV/c

Number of events = 2112

Absolute normalization uncertainty = 8.0 %

$ t $ [(GeV/c) ²]	$d\sigma/dt$ [mb/(GeV/c) ²]	Error	$ t $ [(GeV/c) ²]	$d\sigma/dt$ [mb/(GeV/c) ²]	Error
0.003	0.5320	0.1750	0.110	0.0893	0.0105
0.005	0.2790	0.0530	0.130	0.0734	0.0095
0.007	0.1930	0.0300	0.150	0.0668	0.0093
0.009	0.2340	0.0340	0.170	0.0656	0.0103
0.011	0.1810	0.0280	0.190	0.0590	0.0104
0.013	0.1360	0.0240	0.225	0.0468	0.0057
0.015	0.1770	0.0280	0.275	0.0393	0.0052
0.017	0.1690	0.0290	0.325	0.0313	0.0047
0.019	0.1680	0.0280	0.375	0.0293	0.0048
0.022	0.1890	0.0220	0.425	0.0277	0.0050
0.027	0.1510	0.0180	0.475	0.0157	0.0037
0.032	0.1480	0.0190	0.550	0.0179	0.0049
0.037	0.1400	0.0190	0.675	0.0063	0.0020
0.042	0.1270	0.0180			
0.047	0.1310	0.0190			
0.052	0.1280	0.0190			
0.057	0.1060	0.0170			
0.063	0.0880	0.0160			
0.067	0.0991	0.0175			
0.072	0.1000	0.0170			
0.077	0.0873	0.0164			
0.082	0.0998	0.0179			
0.087	0.0429	0.0115			
0.092	0.0962	0.0179			
0.097	0.0671	0.0146			

Table 6.5

DIFFERENTIAL CROSS SECTION



Incident neutron momentum = 18.0 to 20.0 GeV/c

Average incident neutron momentum = 19.0 GeV/c

Number of events = 2290

Absolute normalization uncertainty = 7.8 %

$ t $ [(GeV/c) ²]	$d\sigma/dt$ [mb/(GeV/c) ²]	Error	$ t $ [(GeV/c) ²]	$d\sigma/dt$ [mb/(GeV/c) ²]	Error
0.003	0.3550	0.1180	0.110	0.0637	0.0074
0.005	0.1930	0.0370	0.130	0.0554	0.0071
0.007	0.1870	0.0270	0.150	0.0416	0.0062
0.009	0.1670	0.0250	0.170	0.0577	0.0084
0.011	0.1470	0.0230	0.190	0.0655	0.0098
0.013	0.1960	0.0280	0.225	0.0383	0.0046
0.015	0.1490	0.0240	0.275	0.0393	0.0047
0.017	0.2180	0.0320	0.325	0.0285	0.0039
0.019	0.1320	0.0230	0.375	0.0192	0.0031
0.022	0.1380	0.0160	0.425	0.0157	0.0031
0.027	0.1490	0.0170	0.475	0.0110	0.0025
0.032	0.0982	0.0132	0.550	0.0119	0.0024
0.037	0.1160	0.0150	0.650	0.0055	0.0015
0.042	0.0873	0.0131	0.775	0.0023	0.0010
0.047	0.0926	0.0138			
0.052	0.0828	0.0135			
0.057	0.0771	0.0127			
0.063	0.1010	0.0150			
0.067	0.0721	0.0126			
0.072	0.0892	0.0151			
0.077	0.0796	0.0144			
0.082	0.0811	0.0147			
0.087	0.0480	0.0107			
0.092	0.0574	0.0120			
0.097	0.0494	0.0107			

Table 6.6

DIFFERENTIAL CROSS SECTION



Incident neutron momentum = 20.0 to 22.0 GeV/c

Average incident neutron momentum = 21.0 GeV/c

Number of events = 2629

Absolute normalization uncertainty = 7.6 %

$ t $ [(GeV/c) ²]	$d\sigma/dt$ [mb/(GeV/c) ²]	Error	$ t $ [(GeV/c) ²]	$d\sigma/dt$ [mb/(GeV/c) ²]	Error
0.003	0.1820	0.0630	0.110	0.0559	0.0063
0.005	0.1680	0.0320	0.130	0.0541	0.0064
0.007	0.1420	0.0210	0.150	0.0426	0.0056
0.009	0.1690	0.0240	0.170	0.0482	0.0069
0.011	0.1250	0.0190	0.190	0.0506	0.0074
0.013	0.1120	0.0170	0.225	0.0330	0.0038
0.015	0.1360	0.0200	0.275	0.0347	0.0039
0.017	0.1620	0.0230	0.325	0.0236	0.0031
0.019	0.1170	0.0180	0.375	0.0214	0.0030
0.022	0.1270	0.0140	0.425	0.0138	0.0025
0.027	0.0991	0.0121	0.475	0.0101	0.0020
0.032	0.0954	0.0119	0.525	0.0088	0.0020
0.037	0.0917	0.0119	0.575	0.0055	0.0015
0.042	0.0850	0.0118	0.650	0.0034	0.0009
0.047	0.0828	0.0120	0.775	0.0040	0.0012
0.052	0.0865	0.0124			
0.057	0.0909	0.0135			
0.063	0.0727	0.0117			
0.067	0.0747	0.0119			
0.072	0.0523	0.0099			
0.077	0.0561	0.0101			
0.082	0.0662	0.0114			
0.087	0.0620	0.0112			
0.092	0.0720	0.0120			
0.097	0.0762	0.0127			

Table 6.7

DIFFERENTIAL CROSS SECTION



Incident neutron momentum = 22.0 to 24.0 GeV/c

Average incident neutron momentum = 23.0 GeV/c

Number of events = 3190

Absolute normalization uncertainty = 7.6 %

$ t $ [(GeV/c) ²]	$d\sigma/dt$ [mb / (GeV/c) ²]	Error	$ t $ [(GeV/c) ²]	$d\sigma/dt$ [mb / (GeV/c) ²]	Error
0.003	0.1730	0.0590	0.110	0.0477	0.0052
0.005	0.1550	0.0270	0.130	0.0459	0.0052
0.007	0.1240	0.0170	0.150	0.0408	0.0049
0.009	0.1160	0.0150	0.170	0.0415	0.0055
0.011	0.1010	0.0140	0.190	0.0337	0.0051
0.013	0.1160	0.0160	0.225	0.0288	0.0031
0.015	0.1140	0.0160	0.275	0.0252	0.0028
0.017	0.1310	0.0190	0.325	0.0224	0.0026
0.019	0.0954	0.0142	0.375	0.0179	0.0023
0.022	0.0970	0.0104	0.425	0.0112	0.0018
0.027	0.0891	0.0101	0.475	0.0111	0.0018
0.032	0.0857	0.0101	0.525	0.0083	0.0016
0.037	0.1020	0.0120	0.575	0.0054	0.0012
0.042	0.0833	0.0102	0.650	0.0036	0.0007
0.047	0.0859	0.0105	0.750	0.0020	0.0006
0.052	0.0767	0.0101	0.900	0.0013	0.0004
0.057	0.0694	0.0096			
0.063	0.0636	0.0095			
0.067	0.0479	0.0078			
0.072	0.0636	0.0098			
0.077	0.0541	0.0089			
0.082	0.0698	0.0104			
0.087	0.0544	0.0089			
0.092	0.0543	0.0088			
0.097	0.0570	0.0093			

Table 6.8

DIFFERENTIAL CROSS SECTION



Incident neutron momentum = 24.0 to 26.0 GeV/c

Average incident neutron momentum = 25.0 GeV/c

Number of events = 3397

Absolute normalization uncertainty = 7.6 %

$ t $ [(GeV/c) ²]	$d\sigma/dt$ [mb/(GeV/c) ²]	Error	$ t $ [(GeV/c) ²]	$d\sigma/dt$ [mb/(GeV/c) ²]	Error
0.003	0.1900	0.0610	0.110	0.0441	0.0047
0.005	0.1420	0.0250	0.130	0.0391	0.0044
0.007	0.1350	0.0180	0.150	0.0374	0.0044
0.009	0.1050	0.0140	0.170	0.0408	0.0052
0.011	0.1210	0.0160	0.190	0.0300	0.0045
0.013	0.0914	0.0129	0.225	0.0320	0.0032
0.015	0.0815	0.0124	0.275	0.0263	0.0028
0.017	0.1110	0.0160	0.325	0.0175	0.0021
0.019	0.1040	0.0150	0.375	0.0123	0.0017
0.022	0.0959	0.0101	0.425	0.0125	0.0018
0.027	0.0844	0.0092	0.475	0.0080	0.0014
0.032	0.0828	0.0094	0.525	0.0044	0.0010
0.037	0.0892	0.0102	0.575	0.0048	0.0010
0.042	0.0699	0.0085	0.650	0.0025	0.0006
0.047	0.0692	0.0087	0.750	0.0018	0.0005
0.052	0.0719	0.0093	0.850	0.0015	0.0006
0.057	0.0478	0.0071	0.950	0.0011	0.0005
0.063	0.0580	0.0082			
0.067	0.0548	0.0081			
0.072	0.0577	0.0087			
0.077	0.0535	0.0083			
0.082	0.0582	0.0088			
0.087	0.0486	0.0078			
0.092	0.0615	0.0093			
0.097	0.0492	0.0080			

Table 6.9

DIFFERENTIAL CROSS SECTION



Incident neutron momentum = 26.0 to 29.0 GeV/c

Average incident neutron momentum = 27.3 GeV/c

Number of events = 2653

Absolute normalization uncertainty = 8.6 %

$ t $ [(GeV/c) ²]	$d\sigma/dt$ [mb / (GeV/c) ²]	Error	$ t $ [(GeV/c) ²]	$d\sigma/dt$ [mb / (GeV/c) ²]	Error
0.003	0.0957	0.0332	0.110	0.0395	0.0043
0.005	0.0790	0.0151	0.130	0.0379	0.0044
0.007	0.1030	0.0140	0.150	0.0369	0.0045
0.009	0.1030	0.0140	0.170	0.0247	0.0037
0.011	0.0870	0.0124	0.190	0.0248	0.0040
0.013	0.0932	0.0131	0.225	0.0251	0.0028
0.015	0.0820	0.0126	0.275	0.0200	0.0023
0.017	0.0995	0.0142	0.325	0.0172	0.0021
0.019	0.0877	0.0137	0.375	0.0135	0.0019
0.022	0.0686	0.0080	0.425	0.0092	0.0015
0.027	0.0809	0.0093	0.475	0.0070	0.0013
0.032	0.0640	0.0080	0.525	0.0071	0.0014
0.037	0.0558	0.0075	0.575	0.0038	0.0009
0.042	0.0747	0.0091	0.650	0.0012	0.0004
0.047	0.0542	0.0077	0.750	0.0010	0.0004
0.052	0.0699	0.0093	0.900	0.0008	0.0003
0.057	0.0541	0.0081			
0.063	0.0465	0.0073			
0.067	0.0499	0.0078			
0.072	0.0336	0.0063			
0.077	0.0496	0.0080			
0.082	0.0440	0.0073			
0.087	0.0471	0.0078			
0.092	0.0350	0.0066			
0.097	0.0374	0.0070			

- (a) Uncertainties in the measured spectral shape due to statistical errors and differences in spectra for different $m_{p\pi}$ intervals (see Appendix D): 3% to 10%.
- (b) Uncertainty in the spectral shape in assuming that the diffraction dissociation cross section was independent of incident neutron momentum: 1% at 24 GeV/c to 10% at 10 GeV/c.*
- (c) Uncertainty in the integrated beam flux (see Appendix C): 5%.

Uncertainties in the spark chamber efficiencies were included in the relative errors above.

The overall normalization errors are indicated on the tables. They vary from 16% at 10 GeV/c to 8% at 25 GeV/c.

We can make the following general observations about the cross sections:

- (a) The shape of the cross sections agrees very well with the measurements of Miller et al.⁽⁸⁾ and Engler et al.⁽⁹⁾
- (b) The absolute normalizations agree, within errors, with those of Miller et al. and Engler et al. (see Figure 6.13).
- (c) The shape of the cross sections appears to be independent of energy. In particular, the sharp forward peak persists to at least 29 GeV/c.
- (d) There appears to be some structure in the cross sections near $-t = 0.08 \text{ (GeV/c)}^2$.
- (e) There appears to be curvature in the t distributions for $-t > 0.4 \text{ (GeV/c)}^2$.

* We emphasize that even if there is a significant momentum dependence in the diffraction dissociation cross section, it will have very little effect on our absolute normalization between 18 and 26 GeV/c, near the peak in the neutron spectrum.

B. Energy Dependence of the Cross Sections

In order to study the energy dependence of the cross sections and to compare our results with those of other experiments, we have fit our cross sections to the standard two exponential form: $d\sigma/dt = Ae^{-B|t|} + Ce^{-D|t|}$. Since the data at large $|t|$ appear to be more complicated than this simple parameterization would imply, we have restricted the fits to $-t \leq 0.5$ (GeV/c)². Figure 6.10 shows the results of such a fit for two of our cross sections. Figure 6.11 shows the values of the parameters B, D and (C/A) for each region of incident neutron momentum. The values for these parameters appear to be essentially independent of momentum. The weighted average over the entire momentum interval yields

$$d\sigma/dt = f(p_{lab}) \times (e^{-(51 \pm 8)|t|} + (0.8 \pm 0.1)e^{-(4.50 \pm .15)|t|},$$

where $f(p_{lab})$ is a function of p_{lab} . The $t = 0$ cross sections extracted from this parameterization are shown in Figure 6.12 and demonstrate a $p_{lab}^{-(1.81 \pm 0.25)}$ dependence.*

Figure 6.13 shows the momentum dependence of the cross sections at fixed t . The cross sections of Miller et al.⁽⁸⁾ and Engler et al.⁽⁹⁾ are also plotted and agree within experimental errors with the measurements of this experiment. The cross sections at $-t = 0.05$ and $-t = 0.2$ show a momentum dependence of $p_{lab}^{-(1.75 \pm .25)}$ and $p_{lab}^{-(1.72 \pm 0.30)}$ respectively. When the data of Miller et al. and Engler et al. are included, the values of the exponent change to $-(1.97 \pm 0.15)$ and $-(1.89 \pm 0.20)$ respectively.

We have examined the momentum dependence of the cross sections at fixed t , fitting the data to the form $d\sigma/dt = F(t) p_{lab}^{-n}$. The results of these fits are shown in Figure 6.14. The average value of n assuming no t dependence is 1.75 ± 0.15 . The value of n is sensitive to the lowest momentum point, which has a normalization uncertainty of 16%. Varying the value of the 9.8 GeV/c cross

*These values differ slightly from those of reference 57. The differences are due to improvements in extrapolating the measured cross sections to $t=0$ and to improvements in the determination of the neutron spectrum.

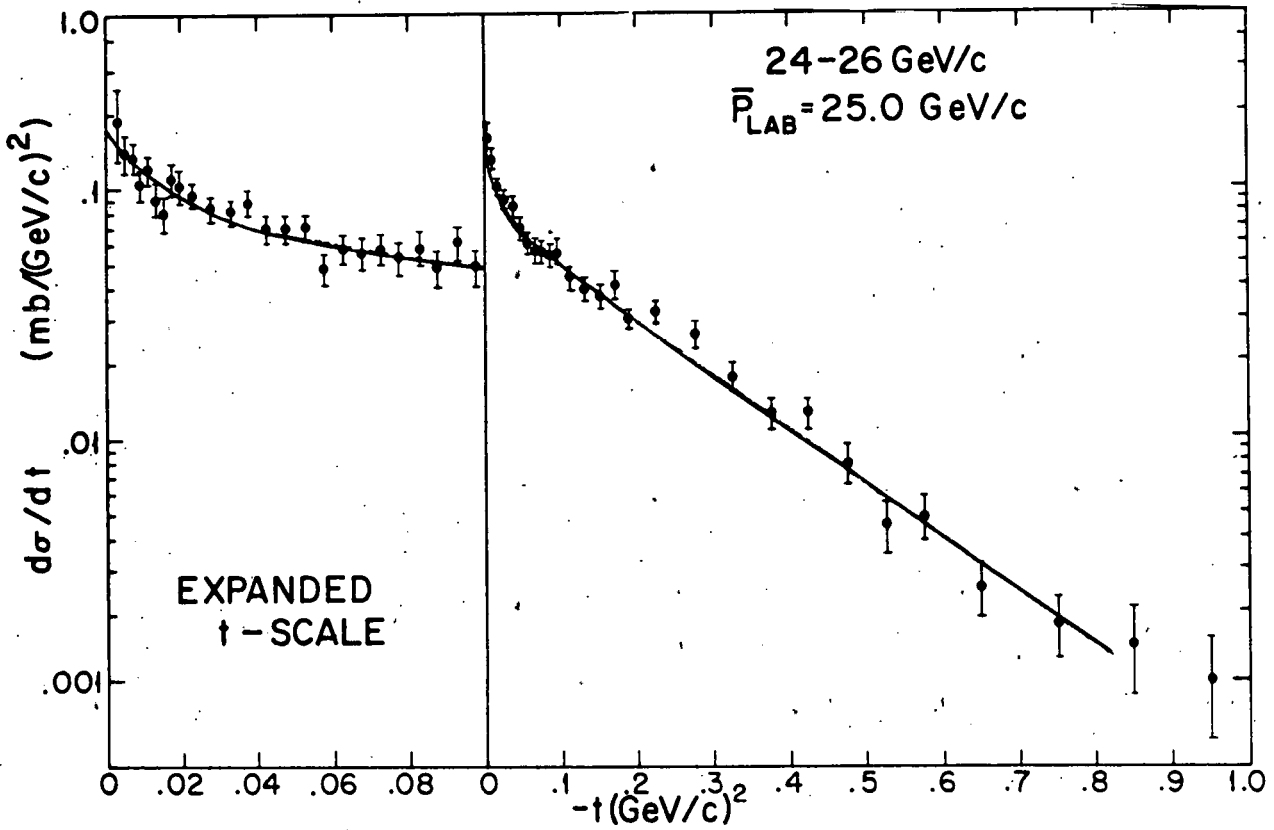
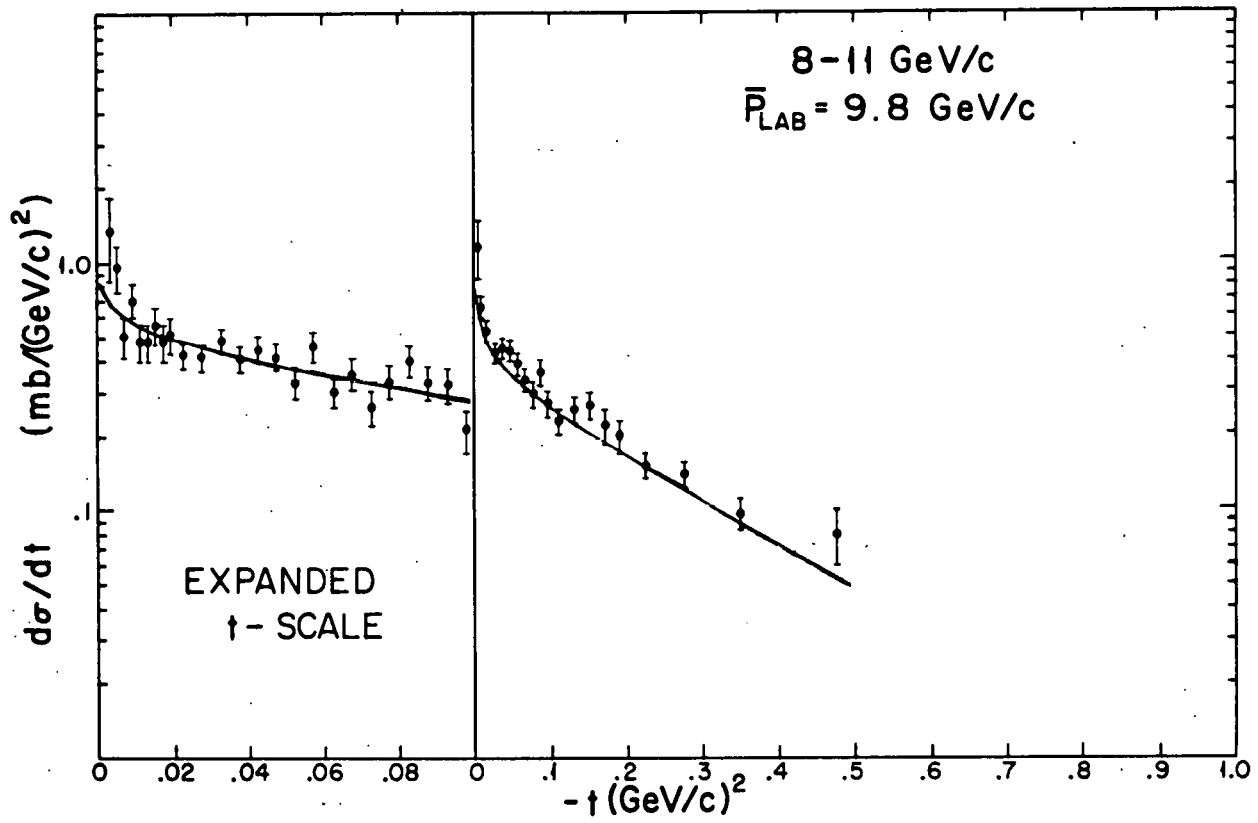


Figure 6.10

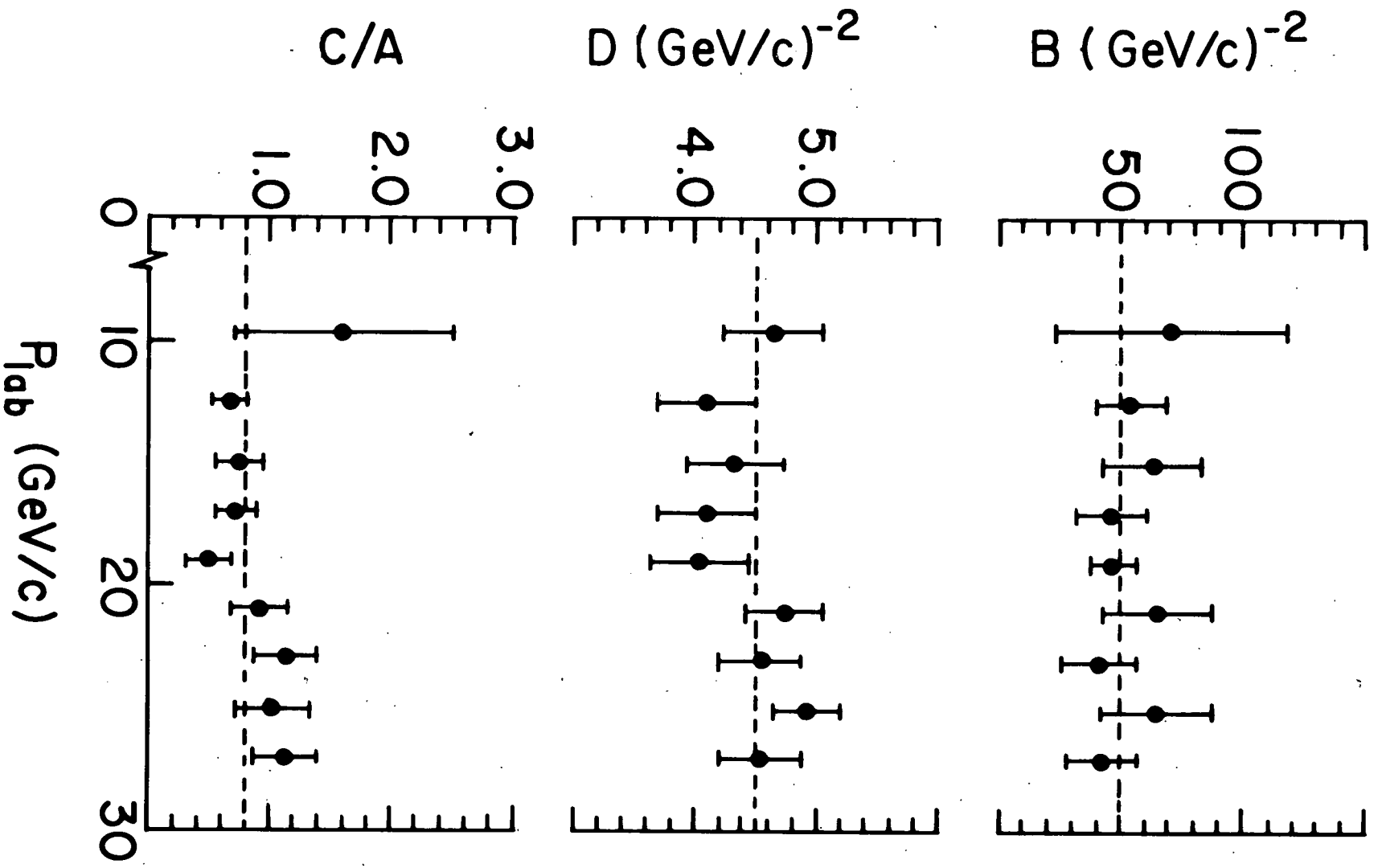


Figure 6.11

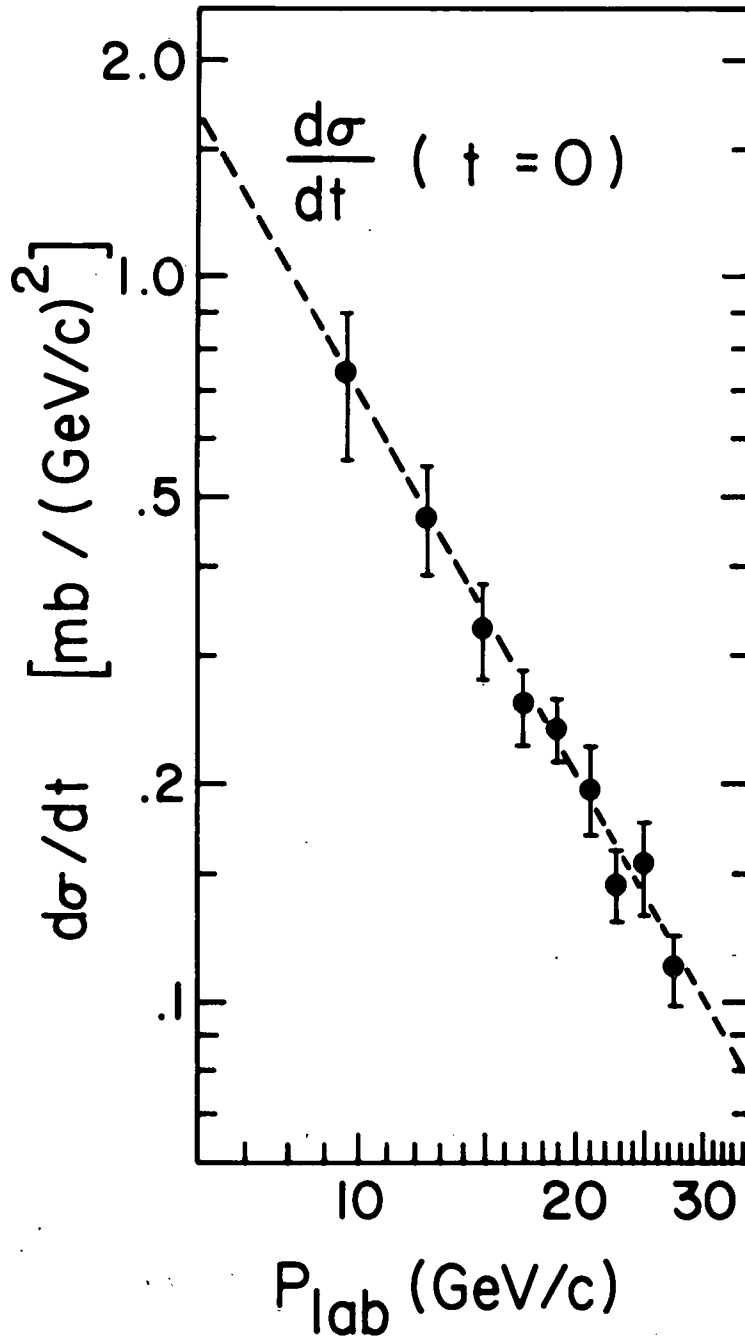


Figure 6.12

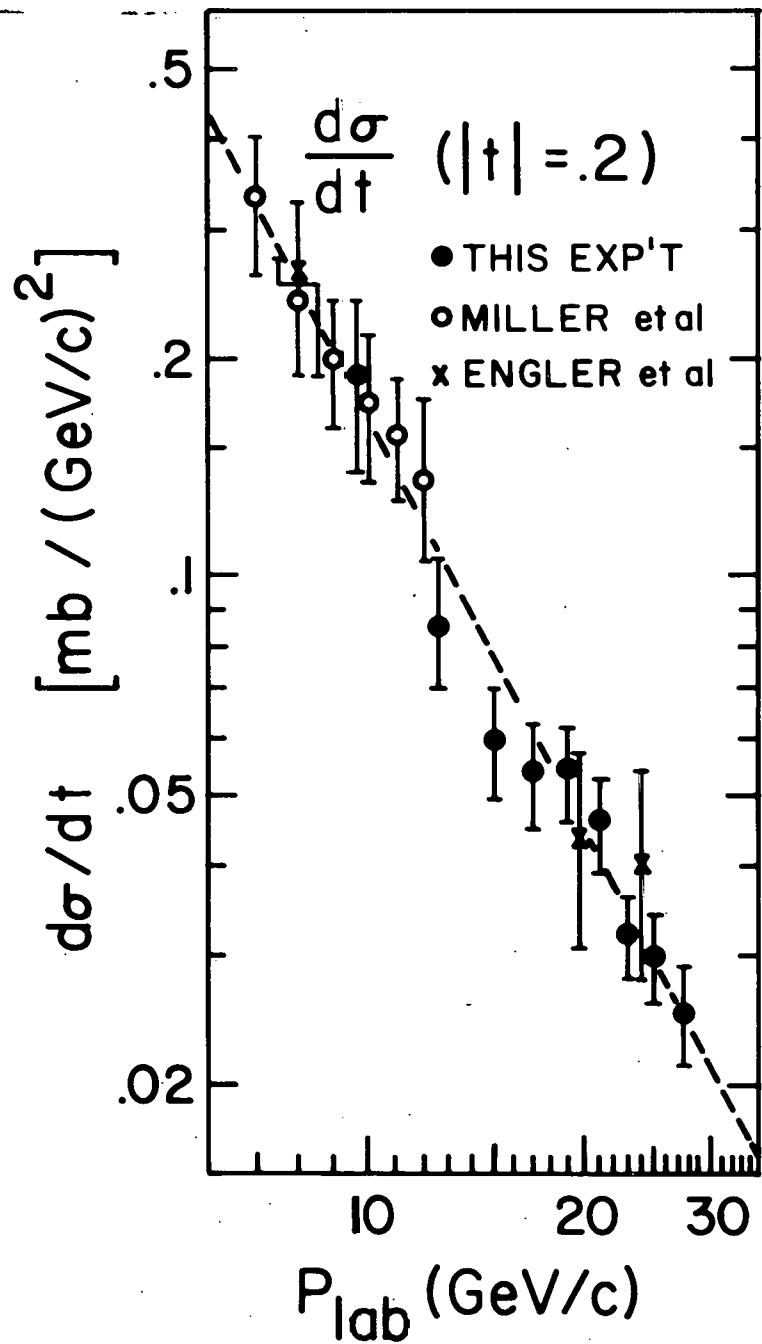
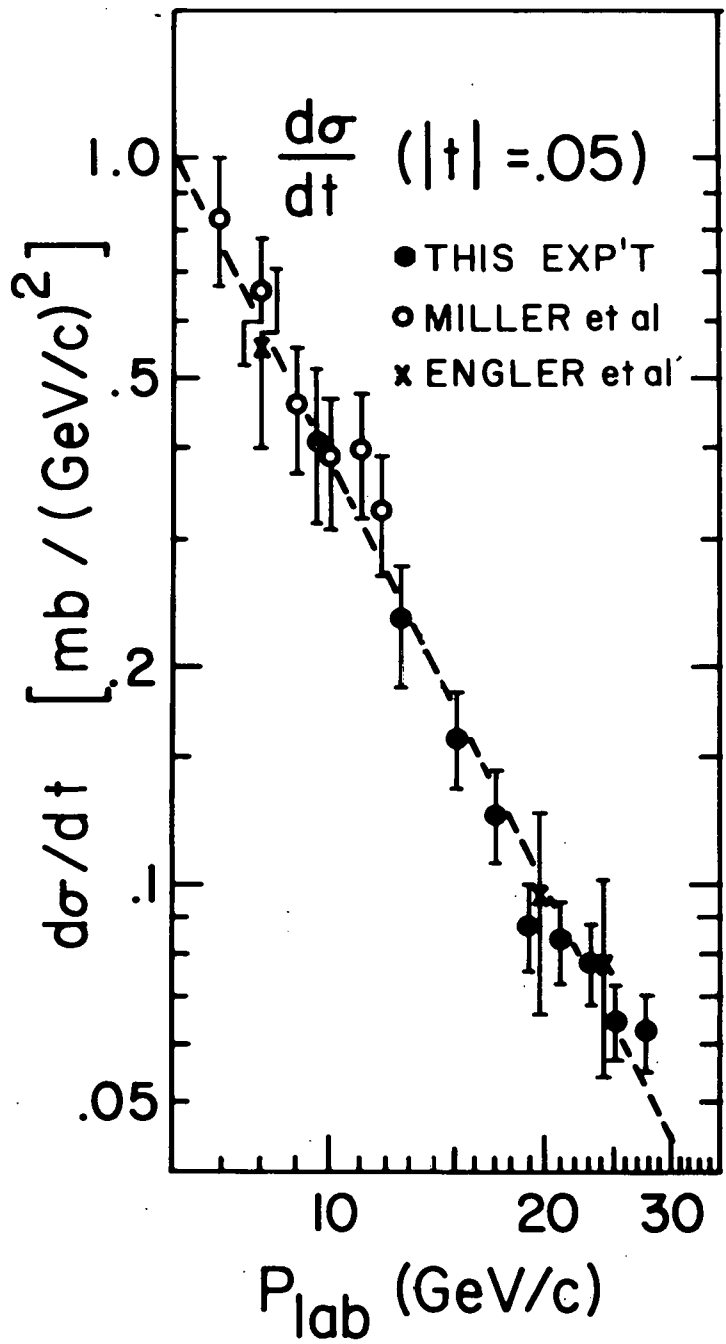


Figure 6.13

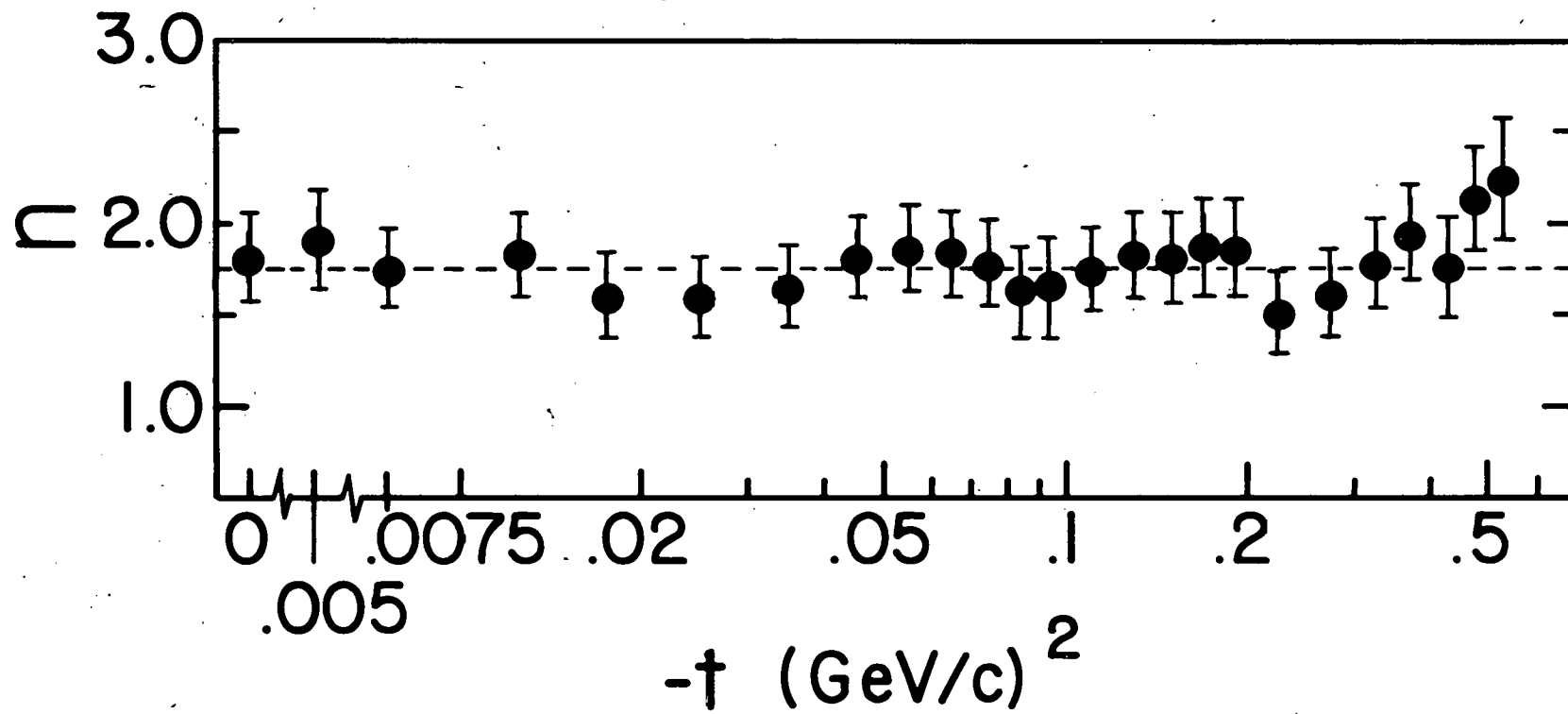


Figure 6.14

section by 16% changes the average value of n by 0.1. If the Miller data are included in the fit, the average n changes to 1.95 ± 0.10 .

C. Comparison with Theory

Our data indicate that the s dependence of the n-p charge exchange cross sections is approximately s^{-2*} , for values of $-t$ between 0.0 and 0.5 (GeV/c)^2 and for energies up to 29 GeV. In the one Regge exchange model (see Chapter II-B) this is the s dependence expected for an interaction dominated by the exchange of a single pion. There is no evidence for shrinkage of the angular distributions between 8 and 29 GeV/c.

In Figure 6.15 we have compared our cross sections for 22-24 GeV/c with two of the models described in Chapter II-B. The dashed line is the prediction of the SCRAM model of Richards et al.⁽⁴⁷⁾ The parameters in this model were determined by fitting data for several other reactions as well as lower energy n-p charge exchange data. This model is able to predict the magnitude and general shape of the cross sections.

The solid line in the figure is a fit to our data done by Gotsman and Maor⁽⁴⁸⁾, using their absorption model with suppression of the pion contribution for $-t \geq 0.2 \text{ (GeV/c)}^2$. They were able to fit our data rather well.

D. Final Remarks

The general dependence of n-p charge exchange scattering on four-momentum transfer and energy up to 29 GeV is now fairly well understood. However, there are still questions regarding details of the differential cross sections. None of the models has been

* $s(s-4m^2) = 4m^2 p_{\text{lab}}^2$; therefore if s is large compared with $4m^2$,
 $s^2 \propto p_{\text{lab}}^2$.

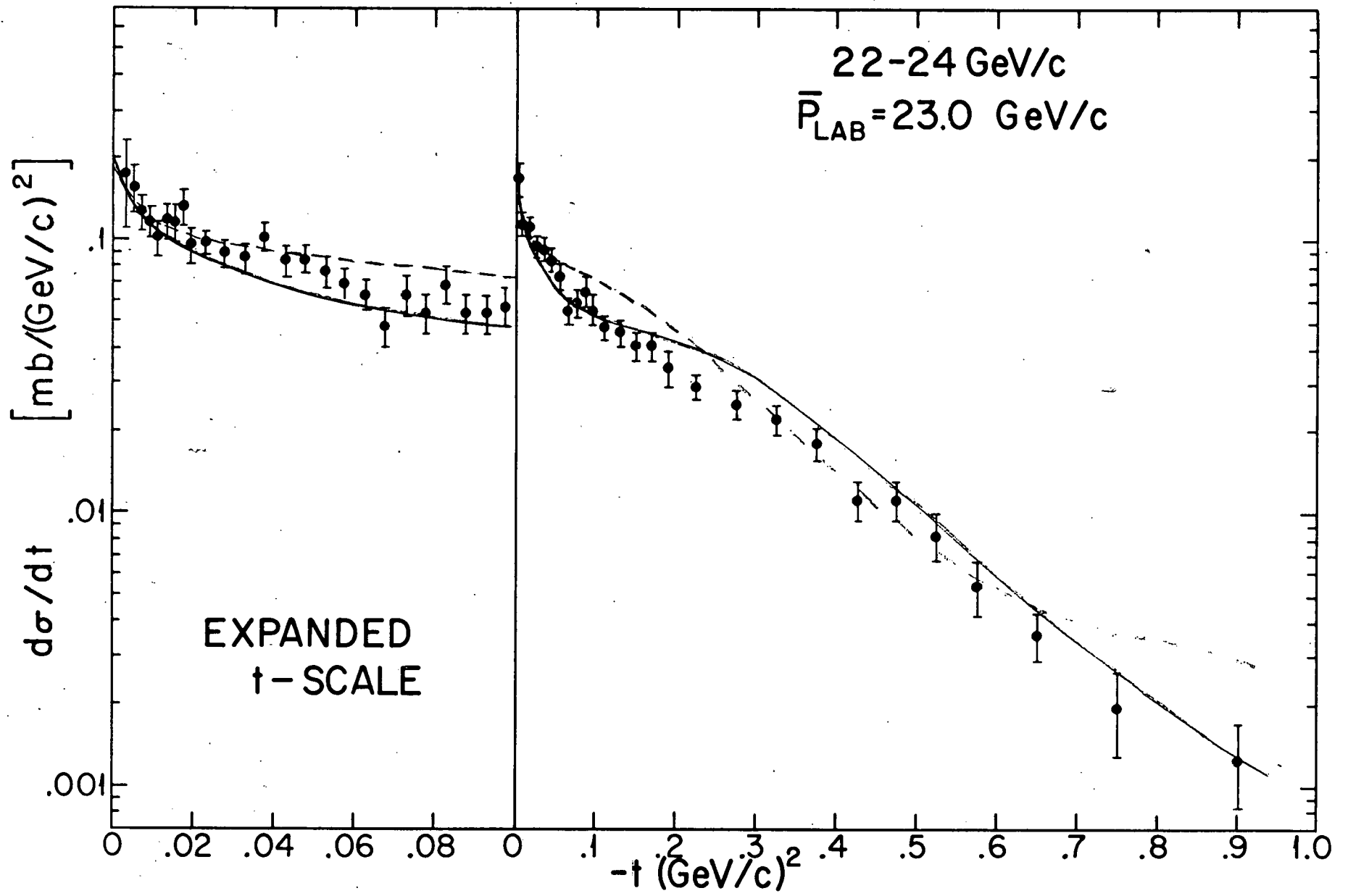


Figure 6.15

able to explain all the features of the measured cross sections, and most models are inadequate at large values of $|t|$.

Two groups are preparing to study n-p charge exchange scattering at higher energies. At Serpukhov, the CERN-Serpukhov collaboration of Engler et al. is preparing to take data at energies up to 70 GeV. The Michigan State-Ohio State collaboration of Abolins et al. has an experiment approved at NAL to study the reaction up to 400 GeV. Perhaps with the data from the present experiment and with future data from the two higher energy experiments, better models can be constructed.

APPENDIX A. KINEMATICS

In Figure A.1 the variables used to describe the kinematics of the n-p charge exchange reaction are defined. It is convenient to describe the reaction in terms of the three Lorentz invariant Mandelstam variables

$$s = (P_1 + P_2)^2 = (P_3 + P_4)^2$$

$$t = (P_1 - P_3)^2 = (P_2 - P_4)^2$$

$$u = (P_1 - P_4)^2 = (P_2 - P_3)^2$$

where the P_i are the four-momenta of the particles,

$$P_i = (E_i, \vec{p}_i)$$

$$P_i^2 = E_i^2 - \vec{p}_i^2 = m_i^2$$

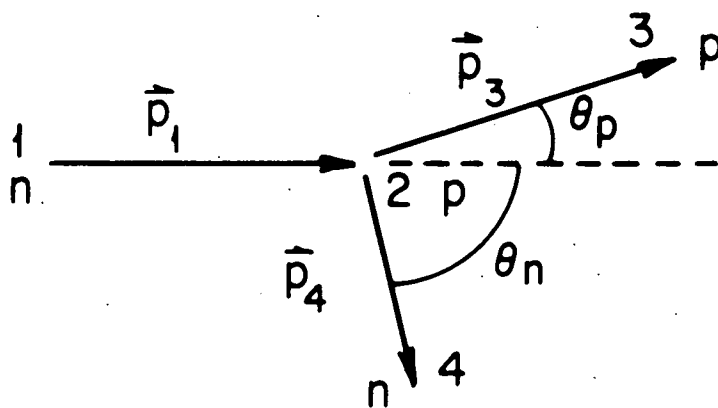
E_i , \vec{p}_i , and m_i are the energy, three-momentum, and mass, respectively, of particle i . A system of units with $\hbar = c = 1$ is used. In the reaction $1 + 2 \rightarrow 3 + 4$, the quantities s , t , and u represent, respectively, the center of mass energy squared, the four-momentum transfer squared between particles 1 and 3, and the four-momentum transfer squared between particles 1 and 4.

The conservation of energy and momentum,

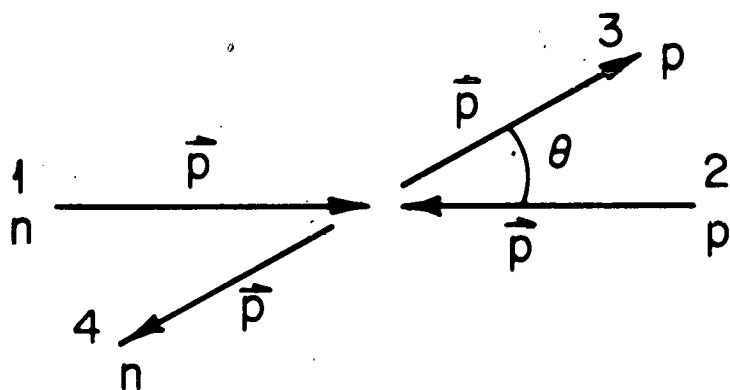
$$P_1 + P_2 = P_3 + P_4,$$

combined with the definitions of s , t , and u , leads to the relation

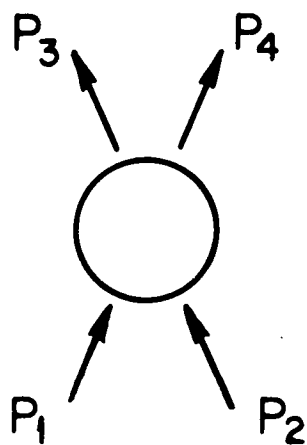
$$s + t + u = \sum_{i=1}^4 m_i^2.$$



(a) Laboratory System



(b) Center of Mass System



$$s = (P_1 + P_2)^2$$

$$t = (P_1 - P_3)^2$$

$$u = (P_1 - P_4)^2$$

(c) Mandelstam Variables

$$1 + 2 \longrightarrow 3 + 4$$

$$n + p \longrightarrow p + n$$

Figure A.1

Crossing symmetry implies that any particle on one side of a reaction can be replaced by its antiparticle with opposite four-momentum on the other side, and that both processes will be described by the same amplitude $A(s,t,u)$. Therefore a single function should describe the reactions

$$\begin{array}{l} n+p \rightarrow p+n \\ \bar{n}+\bar{p} \rightarrow \bar{p}+\bar{n} \end{array} \quad \left. \vphantom{\begin{array}{l} n+p \rightarrow p+n \\ \bar{n}+\bar{p} \rightarrow \bar{p}+\bar{n} \end{array}} \right\} \text{ s channel}$$

$$\begin{array}{l} n+\bar{p} \rightarrow \bar{p}+n \\ \bar{n}+p \rightarrow p+\bar{n} \end{array} \quad \left. \vphantom{\begin{array}{l} n+\bar{p} \rightarrow \bar{p}+n \\ \bar{n}+p \rightarrow p+\bar{n} \end{array}} \right\} \text{ t channel}$$

$$\begin{array}{l} n+\bar{n} \rightarrow p+\bar{p} \\ \bar{p}+p \rightarrow \bar{n}+n \end{array} \quad \left. \vphantom{\begin{array}{l} n+\bar{n} \rightarrow p+\bar{p} \\ \bar{p}+p \rightarrow \bar{n}+n \end{array}} \right\} \text{ u channel}$$

The channel is named after the variable which gives the center of mass energy squared.

The invariant scattering amplitude $A(s,t,u)$ is related to the familiar scattering amplitude $f(E,\cos\theta)$, where

$$\frac{d\sigma}{d\Omega} = |f(E,\cos\theta)|^2$$

by the relationship⁽⁵⁸⁾

$$A(s,t,u) = \sqrt{s} f(E,\cos\theta) ,$$

where E and θ are center-of-mass energy and scattering angle.

Neutron-proton charge exchange scattering can be looked upon either as a forward scattering process in which the neutron and proton exchange charge, or as elastic n-p scattering in the backward direction. If it is considered to be a charge exchange process with particles 1 and 4 neutrons and particles 2 and 3 protons, then, in the center of mass,

$$s = (E_n + E_p)^2$$

$$t = m_n^2 + m_p^2 - 2(E_n E_p + p^2 \cos\theta)$$

$$u = -2p^2 (1 + \cos\theta).$$

(The subscripts n and p refer to the neutron and proton respectively).

If the proton-neutron mass difference is neglected, t can be written

$$t = -2p^2(1 - \cos\theta)$$

If the process is considered to be a backward scattering process, $\theta \rightarrow \pi - \theta$, $\cos\theta \rightarrow -\cos\theta$, and the definitions of t and u are reversed.

In the laboratory system, neglecting the proton-neutron mass difference,

$$s = 2m^2 + 2mE_{\text{lab}}$$

$$t = -2mT_n \approx -p_{\text{lab}}^2 \theta_p^2 \quad (\text{for small angles})$$

where

p_{lab} = incident neutron momentum.

E_{lab} = incident neutron energy

θ_p = laboratory scattering angle of proton

T_n = final neutron kinetic energy.

It is useful to express cross sections in terms of invariant quantities. Since

$$dt = 2p^2 d(\cos\theta) = \frac{2p^2}{\pi} d\Omega,$$

an invariant form for the differential cross section is

$$\frac{d\sigma}{dt} = \frac{\pi}{p^2} \frac{d\sigma}{d\Omega},$$

where the quantities on the right are evaluated in the center of mass system. Expressed in terms of the invariant scattering amplitude $A(s,t,u)$ this becomes

$$\frac{d\sigma}{dt} = \frac{\pi}{p^2 s} |A(s,t,u)|^2 = \frac{4\pi}{s(s-4m^2)} |A(s,t,u)|^2,$$

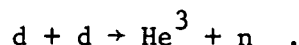
Evaluated in the laboratory, the quantity $s(s-4m^2)$ is

$$s(s-4m^2) = 4m^2 p_{\text{lab}}^2$$

if we neglect the proton-neutron mass difference. Therefore, in the absence of any s dependence of $A(s,t,u)$, the differential cross sections should vary as $1/p_{\text{lab}}^2$.

APPENDIX B. NEUTRON COUNTER EFFICIENCY MEASUREMENT

The efficiencies of the neutron counters were measured at the Princeton University Cyclotron using the reaction



A beam of "tagged" monoenergetic neutrons for calibrating the counters was produced by identifying the He^3 , as shown in Figure B.1. A detailed description of the calibration has been published elsewhere.⁽⁶⁹⁾ Only the results of the measurements will be given here.

Figures B.2, B.3, B.4 and B.5 show the measured efficiencies at four different thresholds, corresponding to the threshold settings of counters N_1 , N_2 , N_3 , and $N_4 - N_{15}$ respectively. The errors shown are statistical. The dashed lines are the results of fits to our data using a Monte Carlo program which simulates the neutron interactions in the scintillator.^{*(70)}

The actual efficiencies of the neutron counters during the n-p scattering experiment were slightly higher than the measured values because some neutrons were scattered into the counters from adjacent counters and from the 1/4 inch lucite walls on the sides of the counters. If we assume that half of the neutrons which enter the walls are scattered into the counter and that half are scattered out, the increase in counter efficiency will be approximately 10% of the measured value. A modification of the Monte Carlo program mentioned above was used to calculate more accurately the effect of the walls and the adjacent counters. Corrections to the efficiencies varied from 6% of the measured efficiency at small $|t|$ to 12% at large $|t|$, with uncertainties of approximately 3% of the measured efficiency.

*The threshold and β , the one-photo-electron level, are parameters in the Monte Carlo program. These parameters were adjusted to give the best fit to the data. (See reference 69)

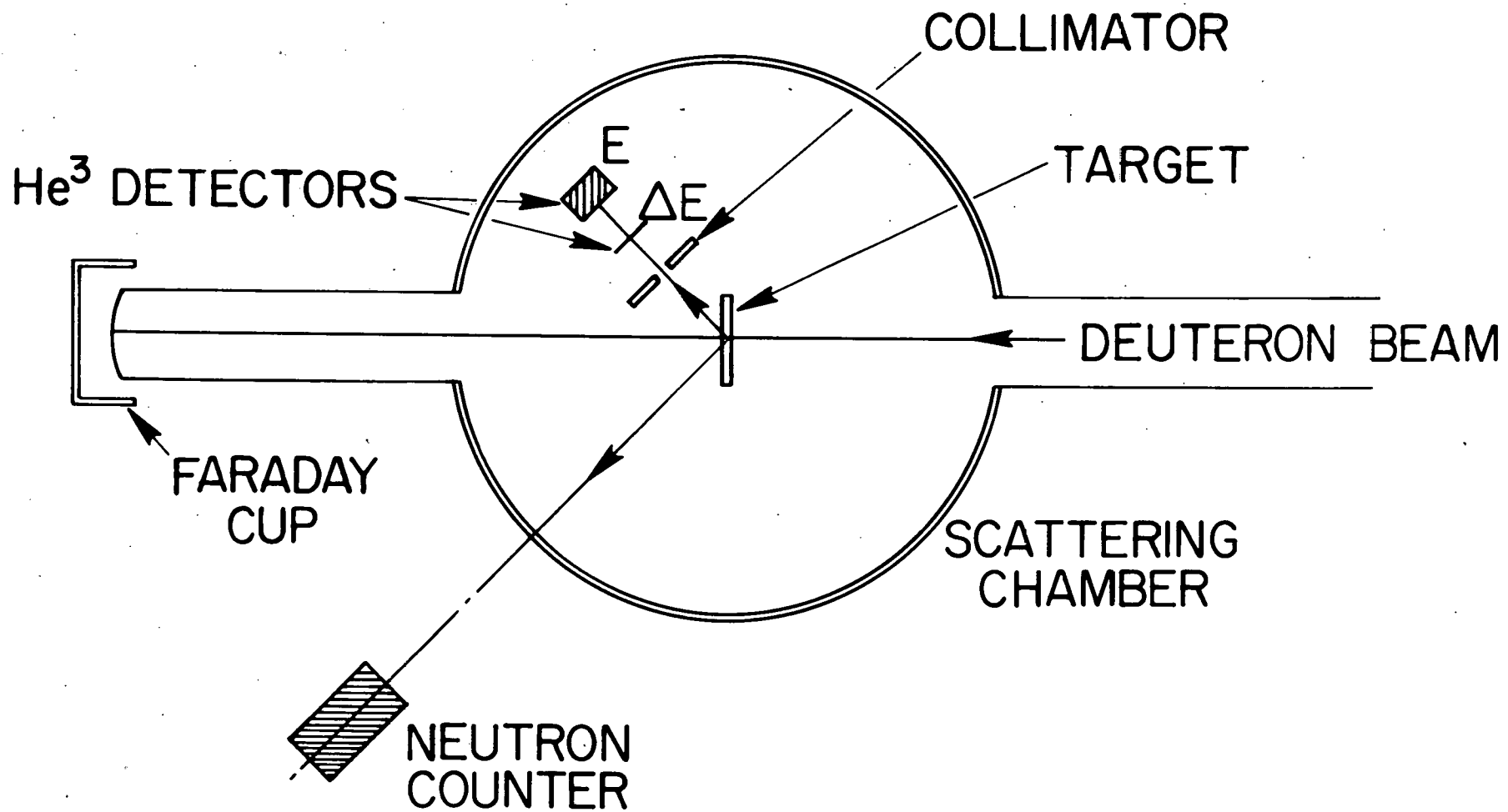


Figure B.1

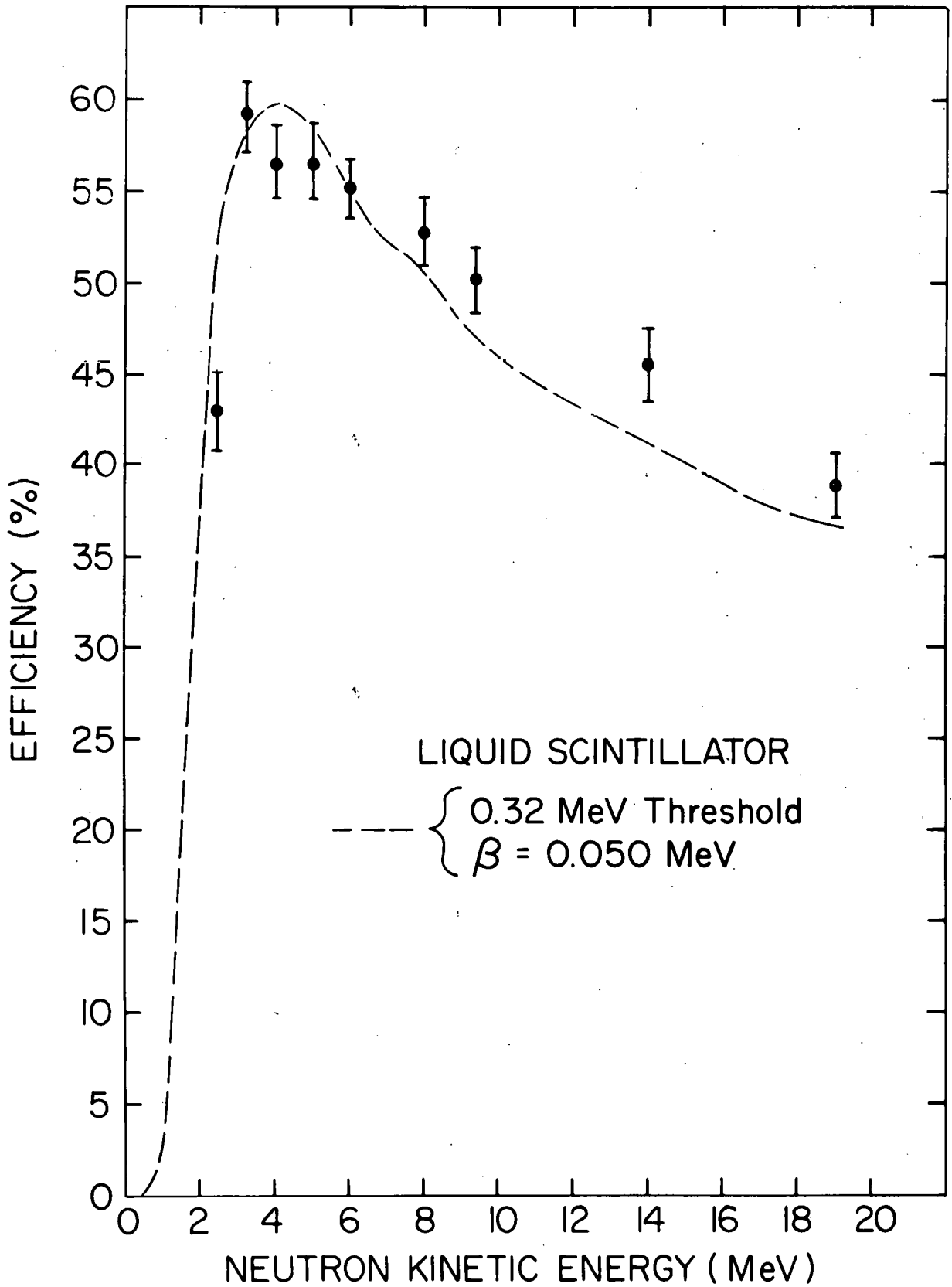


Figure B.2

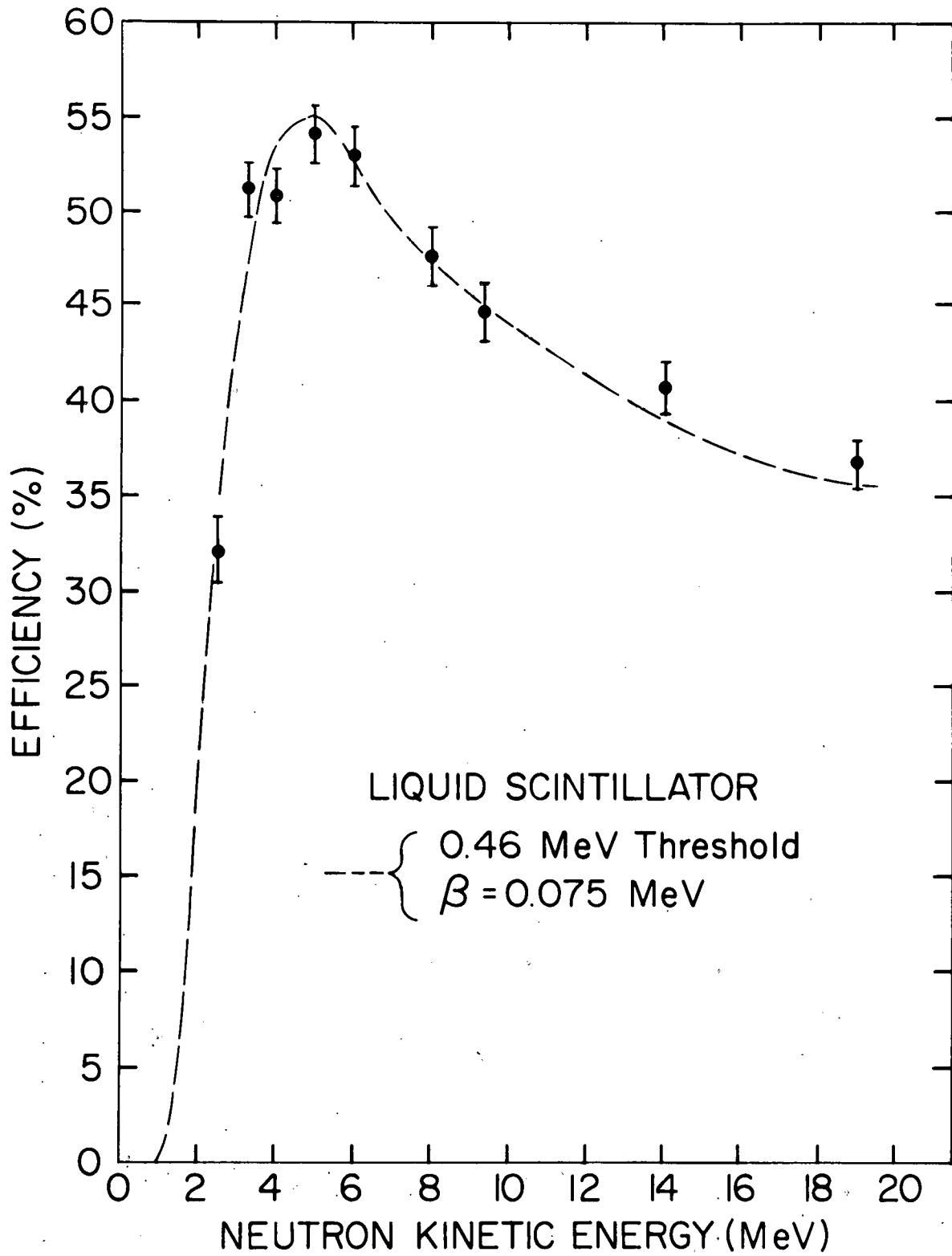


Figure B.3

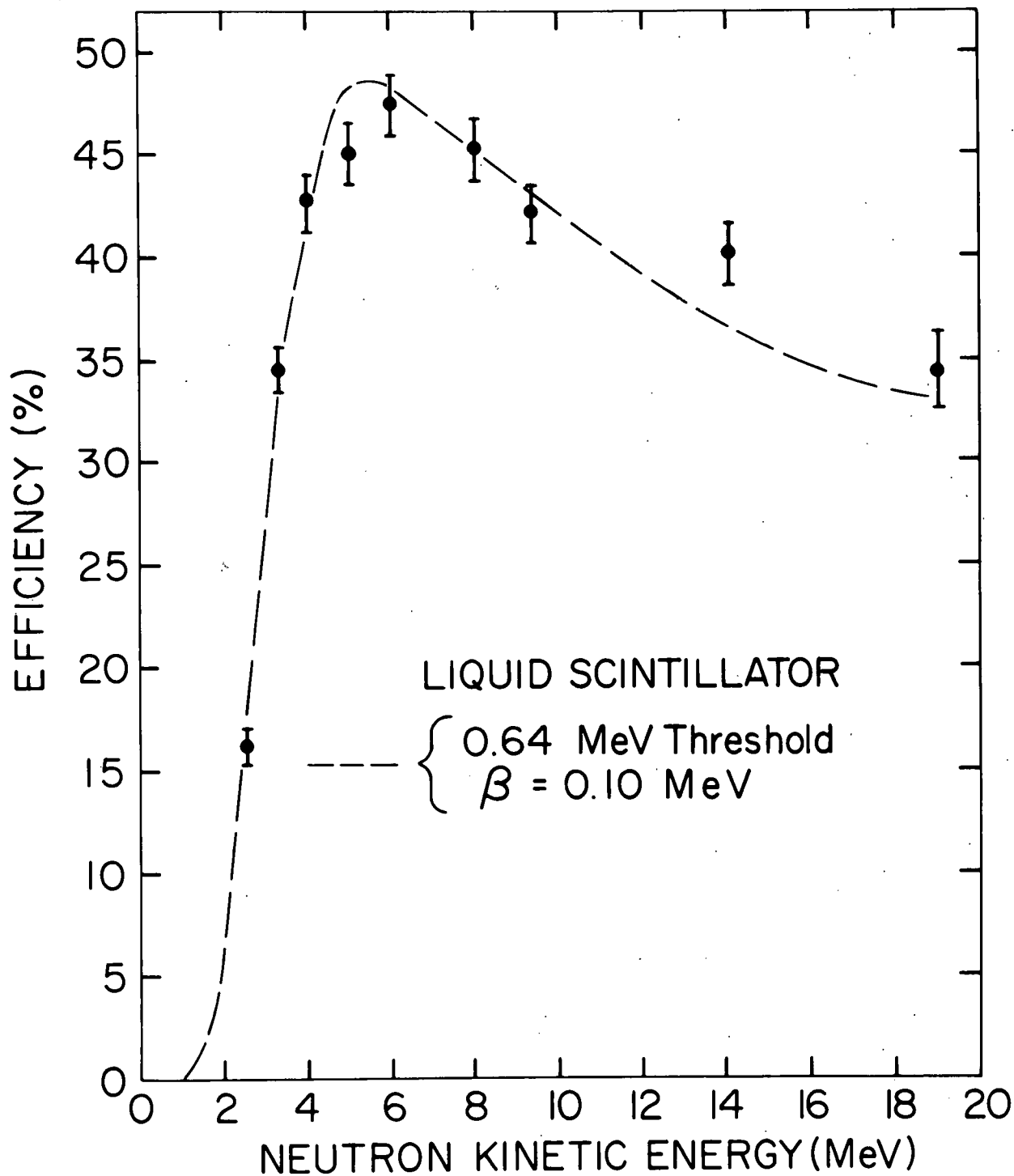


Figure B.4

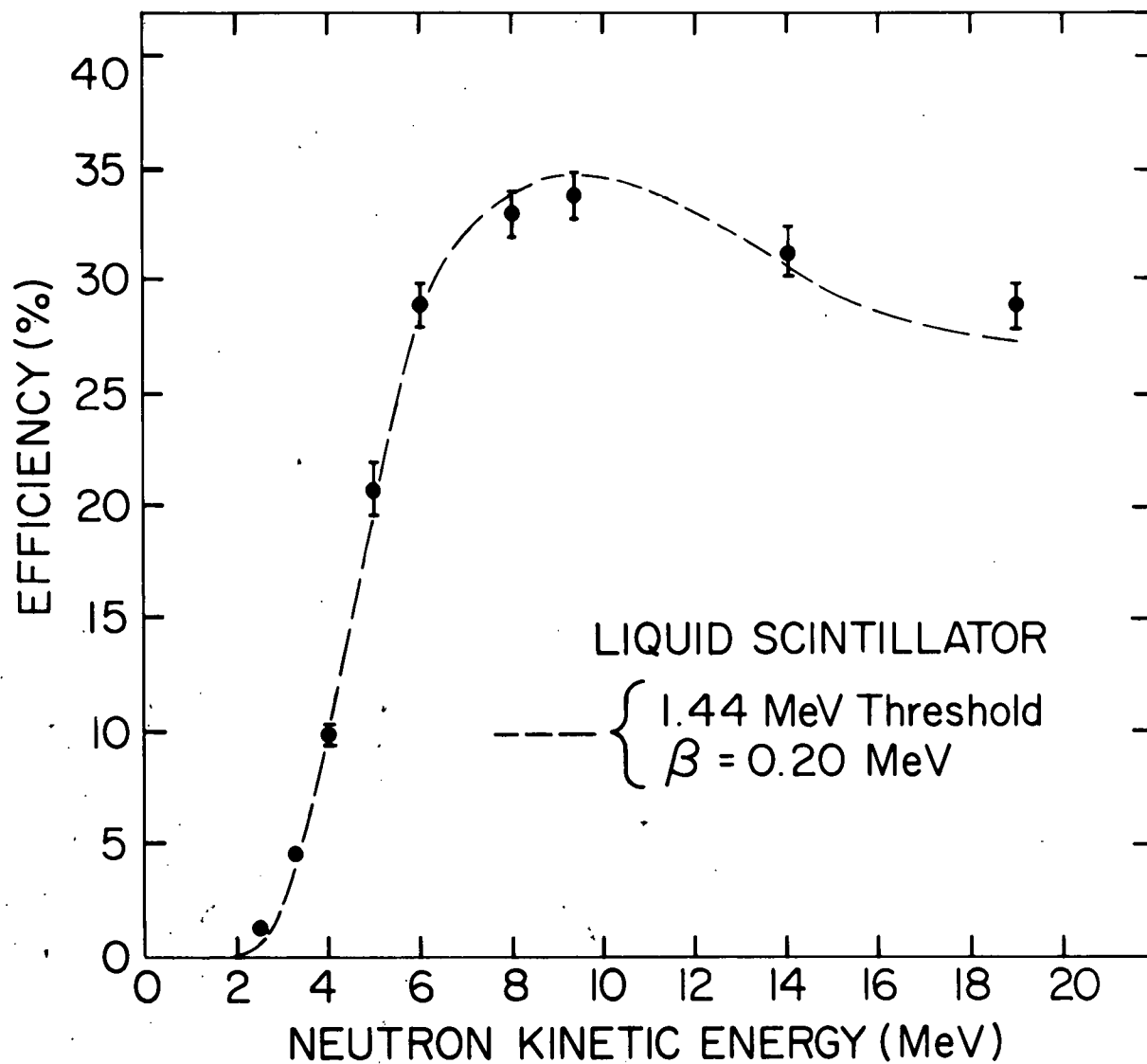


Figure B.5

APPENDIX C. TOTAL NEUTRON FLUX

This appendix describes the determination of the total number of neutrons per monitor count.

The integral neutron flux was measured using a total absorption spectrometer (TAS) located approximately 300 feet downstream of the liquid hydrogen target. A detailed description of the TAS and its use in the measurement of neutron-nucleus total cross sections from 10 to 30 GeV/c can be found elsewhere.⁽⁵⁹⁾

The total absorption spectrometer is shown in Figure C.1. It consisted of 13 iron plates, 56 cm x 82 cm x 3.8 cm, interleaved with 14 sheets of plastic scintillator, 56 cm x 82 cm x 0.65 cm. The scintillators were grouped into two sets of seven, each set viewed by a 56 AVP photomultiplier. The outputs of the two photomultipliers were added passively to give a pulse height which was roughly proportional to the energy of the neutron.

The fraction of the incident neutrons which interacted with matter in the TAS is

$$f = 1 - e^{-x}$$

where x is the number of collision lengths of material (scintillator and iron) in the TAS. x was calculated using measured values for the total cross section for neutrons on iron.⁽⁶⁰⁾

Since the cross sections varied by only a few percent (<3%) between 8 and 30 GeV/c, an average value of 1140 mb was used for the whole energy range.

If all the neutrons which interacted in the iron produced charged particles which entered the scintillator, the efficiency would be equal to f . However, about 1/3 of the total cross section is elastic at these energies, leading to no charged particles. Therefore, the efficiency was calculated to be

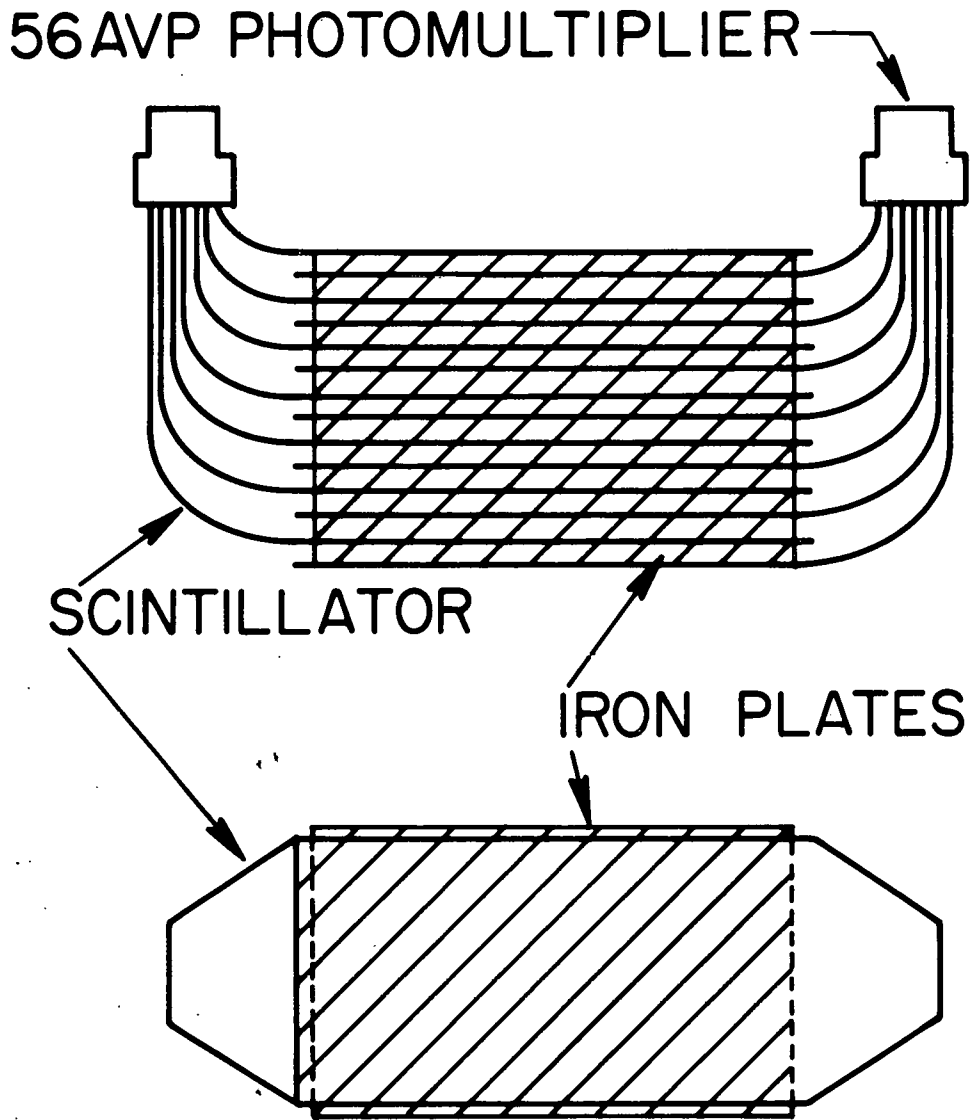


Figure C.1

$$E \approx 1 - e^{-kx} = 96\% \pm 3\%$$

where $k \approx 2/3$, and $x = 4.9$. The 3% error is due to the uncertainty in the value of k . The efficiency for detecting gammas was $\sim 100\%$.

The setup for a neutron flux measurement is shown in Figure C.2. M is the primary beam monitor, L is a secondary monitor and γ_1 and γ_2 are gamma filters. All extraneous material was removed from the beam line downstream of the liquid hydrogen target.

The instantaneous counting rate in the TAS was approximately 500 KHz. Accidentals were approximately 5 to 10%. It was necessary to correct the TAS readings for beam rate effects. In order to estimate this rate correction a series of measurements were made at different beam intensities (i.e., at different values of monitor counts per pulse = M/pulse). Figure C.3 shows the extrapolation to zero beam intensity. The value of TAS/M at zero beam intensity was 24.7 ± 0.3 .

The TAS detected gammas as well as neutrons. Therefore, it was necessary to make a correction for gamma contamination in the neutron beam. Since the monitor counter M also detected gammas, the ratio TAS/M was relatively insensitive to small gamma contaminations.

Assuming negligible gamma contamination, (measurements described in Appendix D found the gamma contamination to be less than 1%) we obtain

$$\frac{N}{M} = \frac{TAS}{M} \cdot \frac{e^L}{E} = 31.8$$

where N/M = number of neutrons at the hydrogen target per count in monitor M

TAS/M = number of counts in the TAS (extrapolated to zero beam intensity) per count in monitor M

E = efficiency of the TAS for detecting neutrons = 96%

L = number of collision lengths of material between the TAS and the liquid hydrogen target = 0.210.

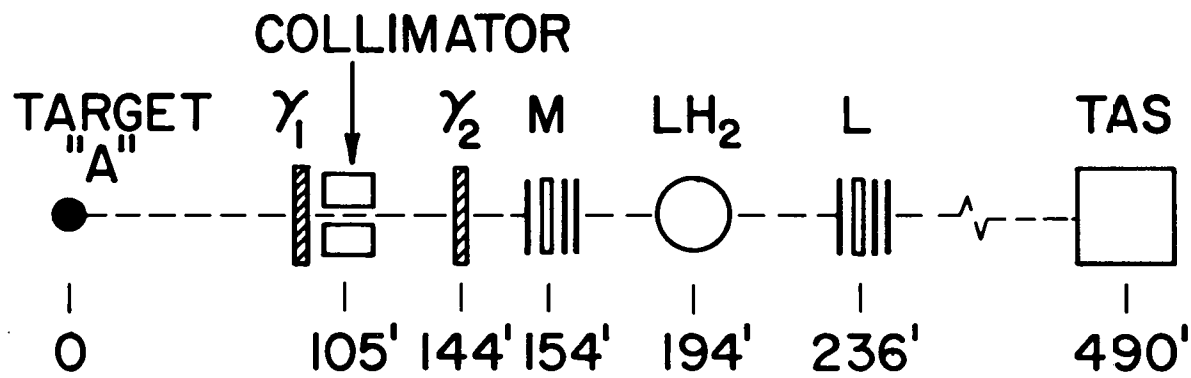


Figure C.2

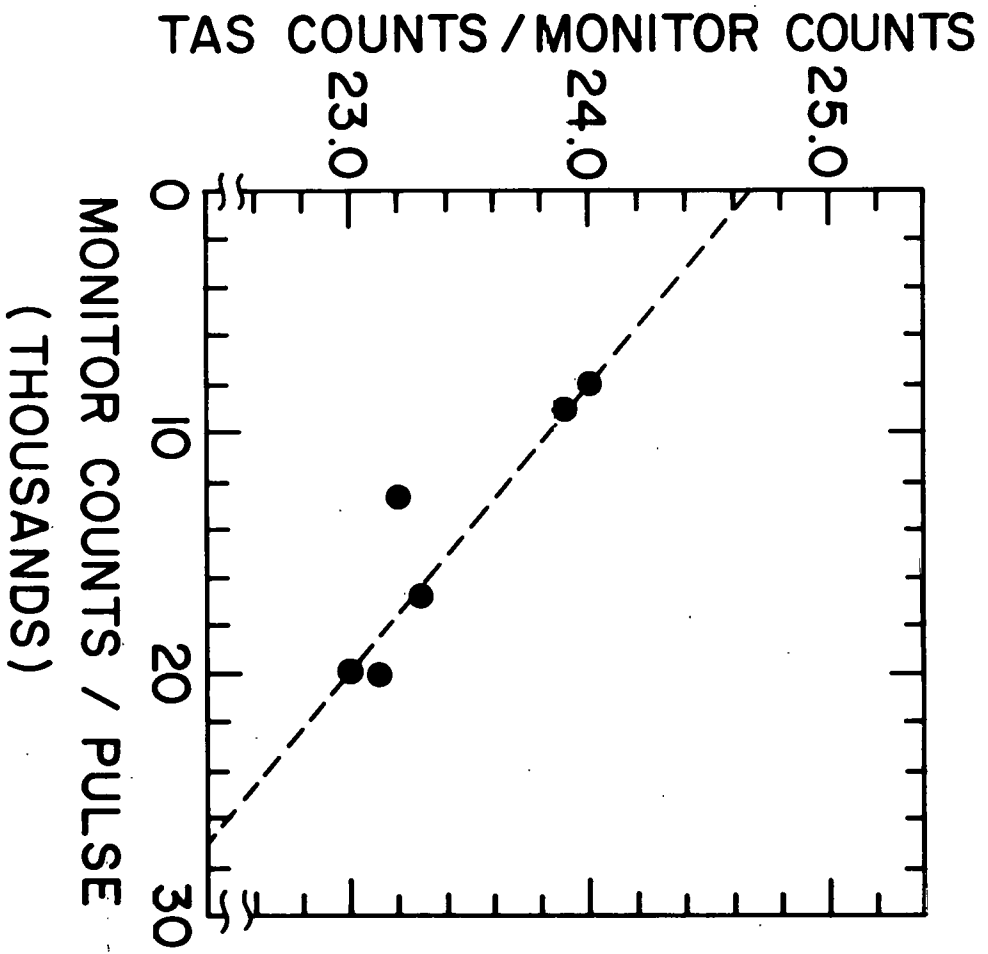


Figure C.3

An additional small correction of $2\% \pm 2\%$ was necessary as the gamma filter used for these calibration runs was inadvertently slightly thinner than in the main data runs.

The final value for the integral number of neutrons per monitor is

$$\frac{N}{M} = 32.6 \pm 1.8 \quad .$$

The uncertainty of approximately 5% comes from a 1% uncertainty in the value of TAS/M, a 4% uncertainty in gamma contamination during this measurement, and a 3% uncertainty in the efficiency of the TAS.

APPENDIX D. MEASUREMENT OF INCIDENT
NEUTRON MOMENTUM SPECTRUM

The momentum spectrum of incident neutrons was determined in a separate experiment, namely the diffraction dissociation of neutrons off carbon nuclei



This experiment was part of a larger experiment done to study the general properties of diffraction dissociation of neutrons from nuclei.⁽⁶¹⁾ Most of the analysis has been done at the University of Michigan, and only those results pertinent to the normalization of the n-p charge exchange cross sections are described here.

Reaction (1) is one of a class of two body reactions in which no changes in quantum number occur except for spin and parity. When spin and parity change, they must obey the relation⁽⁶⁶⁾

$$\Delta p = (-1)^{\Delta J}$$

These "quasi elastic" reactions can be assumed to proceed via the exchange of a particle with the quantum numbers of the vacuum (Pomeron exchange). In the Regge theory, $d\sigma/dt \propto s^{2\alpha(t)-2}$, or (since most of the cross section is concentrated near $t=0$) $\sigma \propto s^{2\alpha(0)-2}$. For Pomeron exchange, $\alpha(0) \approx 1$. We expect the cross section, therefore, to be approximately independent of energy.

A physical argument for the energy independence of the cross sections was made by Morrison⁽⁶²⁾. The reaction $n+C \rightarrow (p\pi^-) + C$ can be assumed to proceed as in Figure D.1. The neutron virtually dissociates into a $p\pi^-$ pair and the π^- scatters diffractively off the nucleus. The dissociation $n \rightarrow p\pi^-$ is independent of

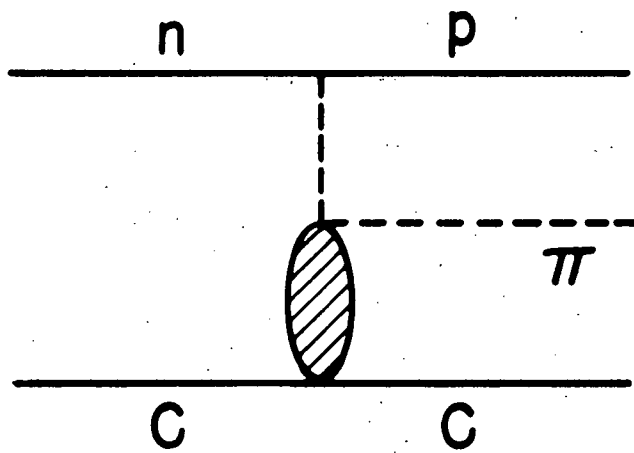


Figure D.1

the momentum of C, and the π -C scattering is a high energy elastic process, approximately independent of momentum. We therefore expect the diffraction dissociation cross section to be approximately independent of momentum.

There exists no previous data on diffraction dissociation of neutrons off nuclei. However, similar processes have been studied, for example $p+p \rightarrow p+N_{1/2}^*$ (63,64). Measurements indicate that these cross sections are essentially constant between 10 and 30 GeV/c*. Additional examples of "quasi-elastic" processes and references to other data can be found in the articles in references 65 and 66.

It was assumed that the cross section for $n+C \rightarrow (p\pi^-) + C$ is constant for incident neutron momenta between 8 and 29 GeV/c and for $p\pi^-$ masses less than 1.5 GeV. This assumption is consistent with current theoretical expectations and with measurements on related processes, as discussed above. With this assumption, the incident neutron spectrum was determined by measuring the number of events from reaction (1) as a function of neutron momentum.

The experimental layout is shown in Figure D.2. The 1" thick carbon target was surrounded by a set of anticounters, sensitive to gammas and charged particles. The momentum vectors of the pair of charged particles produced in reaction (1) were measured in a wire-spark-chamber magnet spectrometer (described in Chapter III-C). The trigger requirement was $P_1\bar{A}L_2R_2$ or $P_1\bar{A}L_3R_3$, where the scintillation counters A,P,L, and R are defined in Figure D.2. The resolution of the spectrometer in this configuration was approximately ± 1.2 mrad in opening angle and $\pm 1.5\%$ in momentum at 15 GeV/c. Further details of the experimental set-up can be found in reference 61.

*The momentum dependence is at most $P_{lab}^{-0.2}$ (71).

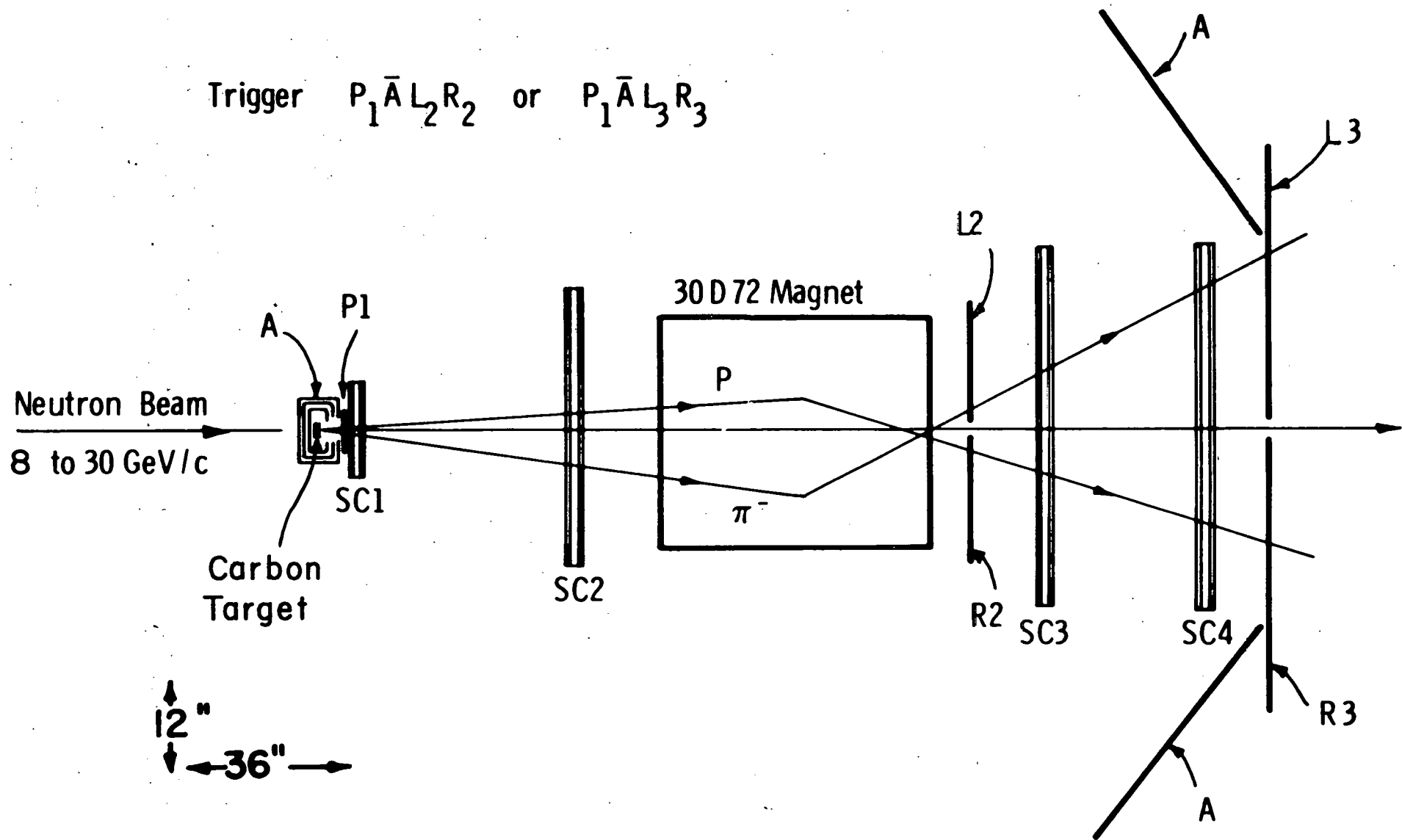


Figure D.2

W

Each two track event was fit to the hypothesis that it was $n+C \rightarrow (p\pi^-) + C$. Since the momenta of the recoil nucleus (or its fragments) and of the incident neutron were unknown, there was a zero constraint fit. There is additional information, however, which allows a selection of elastic events. In reaction (1), a diffraction peak is expected at small four-momentum transfer to the nucleus. The observation of a forward peak of proper width (with a diffraction radius characteristic of the nucleus) indicates that the nucleus acted coherently for a large fraction of the events and that reaction (1) actually occurred.

Figure D.3 shows the distribution of events in $t' = t - t_{\min}$, where $t' \approx -p_{\perp}^2$ and $t_{\min} = 1/4(m_{p\pi^-}^2 - m_n^2)^2/p_{\text{lab}}^2$. The logarithmic slope of the peak is approximately 60 (GeV/c)^{-2} . This is approximately equal to the value expected for carbon ($\sim 53 \text{ (GeV/c)}^2$). A straight line extrapolation indicates that incoherent backgrounds under the coherent peak are $\leq 20\%$.

The $p\pi^-$ mass distributions (uncorrected for the acceptance) for $|t'| < .01 \text{ (GeV/c)}^2$ are shown in Figure D.4. The "target out" backgrounds have been subtracted. The acceptance, determined by a Monte Carlo program, is indicated by the dashed line. The mass resolution of the apparatus was $\sim 10 \text{ MeV}$ at 1.2 GeV .

The mass distributions show little evidence for the presence of any of the well-known $I = 1/2$ nucleon isobars. The results are consistent with the idea that the diffraction dissociation is dominated by the mechanism of Figure D.1. A Monte Carlo calculation based on such a model has the same general shape as the observed mass spectrum. (61)

For each event falling under the diffraction peak ($|t'| < .02$), the incident neutron momentum was calculated, assuming that the reaction was $n+C \rightarrow (p\pi^-) + C$. The angular distributions in the $p\pi^-$ rest frame and the $p\pi^-$ mass distributions were found to be independent, within statistics, of the incident neutron momentum, consistent with the assumption that the cross section is independent of the incident momentum between 8 and 29 GeV/c. The neutron spectra for several intervals of $m_{p\pi^-}$ (mass of $p\pi^-$)

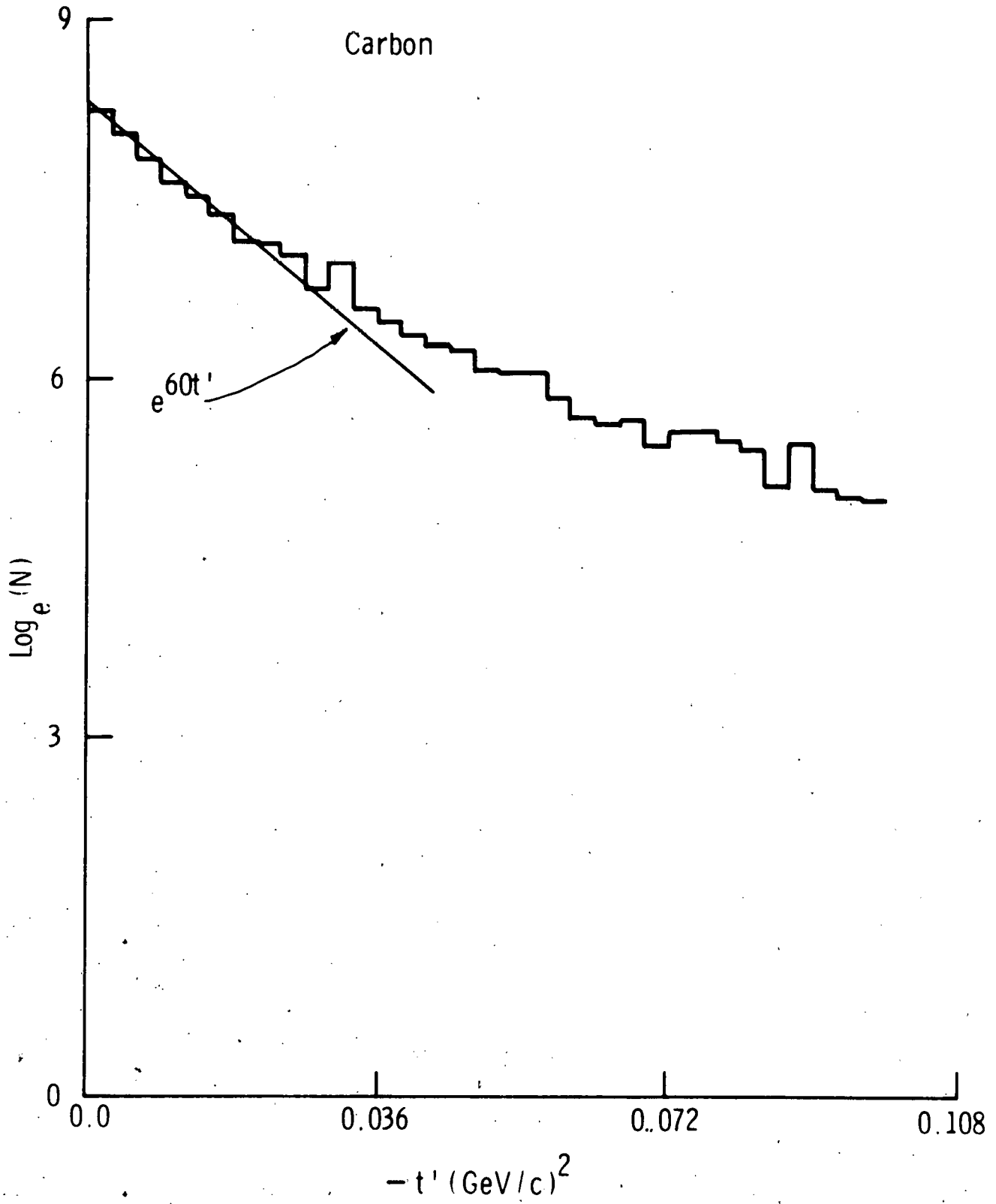


Figure D.3

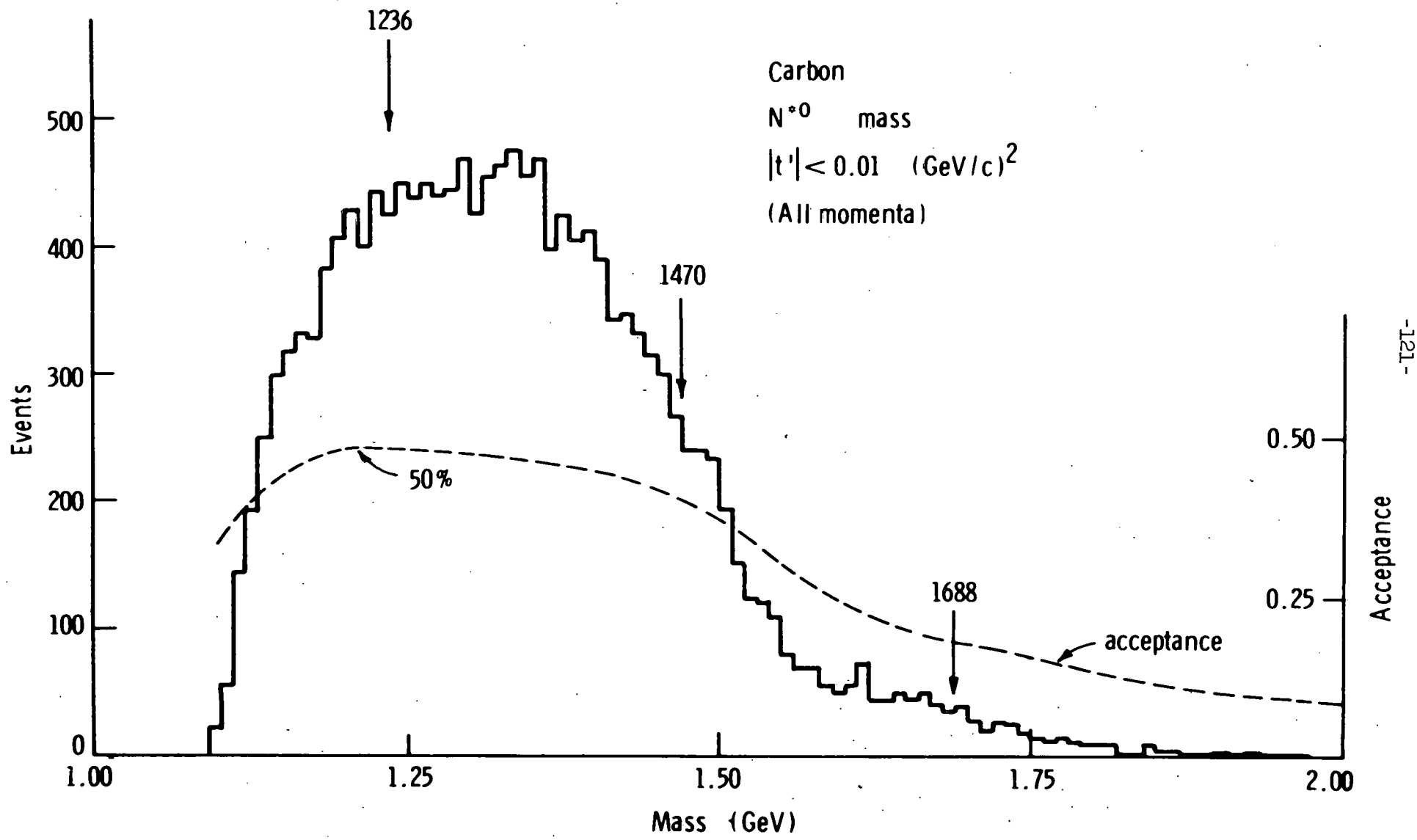


Figure D.4

were compared and found to be the same within experimental error. Gamma contamination was determined by fitting each event to the hypothesis that it was $\gamma + C \rightarrow (e^+e^-) + C$. No gamma contamination was found above 15 GeV/c, and below 15 GeV/c the gamma contamination was at most 3%. The total gamma contamination was less than 1%.

To normalize the spectrum properly above 20 GeV/c, the momentum resolution of the spectrometer was unfolded. The resolution was approximately ± 0.5 GeV/c at 20 GeV/c and ± 1 GeV/c at 30 GeV/c. The unfolded spectrum was determined by assuming a shape, folding in the resolution of the spectrometer, comparing this folded spectrum with the measured one, and adjusting the assumed spectrum by the difference. This process was iterated until the calculated spectral shape agreed with the measured one. The measured and unfolded spectra are essentially the same below 22 GeV/c. Uncertainties in the shape of the spectrum due to errors in unfolding are less than $\sim 3\%$.

Figure D.5 shows the unfolded neutron spectrum for $|t'| < 0.02$ (GeV/c)² and $m_{p\pi^-}$ between 1.1 GeV and 1.35 GeV, with the gamma contamination subtracted. Uncertainties in the measured spectral shape, based on statistics and on a comparison of spectra for different values of $m_{p\pi^-}$, range from 3% at 24 GeV/c to 10% at 10 GeV/c. Uncertainties in the measured spectral shape due to lack of knowledge of the exact p_{lab} dependence of the diffraction dissociation cross section are $\sim 10\%$ at 10 GeV/c and are negligible at 24 GeV/c, near the peak of the spectrum.

The broken line in Figure D.5 is the Trilling formula⁽⁶⁷⁾ for the production of protons in a target at 0° . The proton spectrum is expected to be similar in shape to the neutron spectrum far from the kinematic limit.⁽⁶⁸⁾

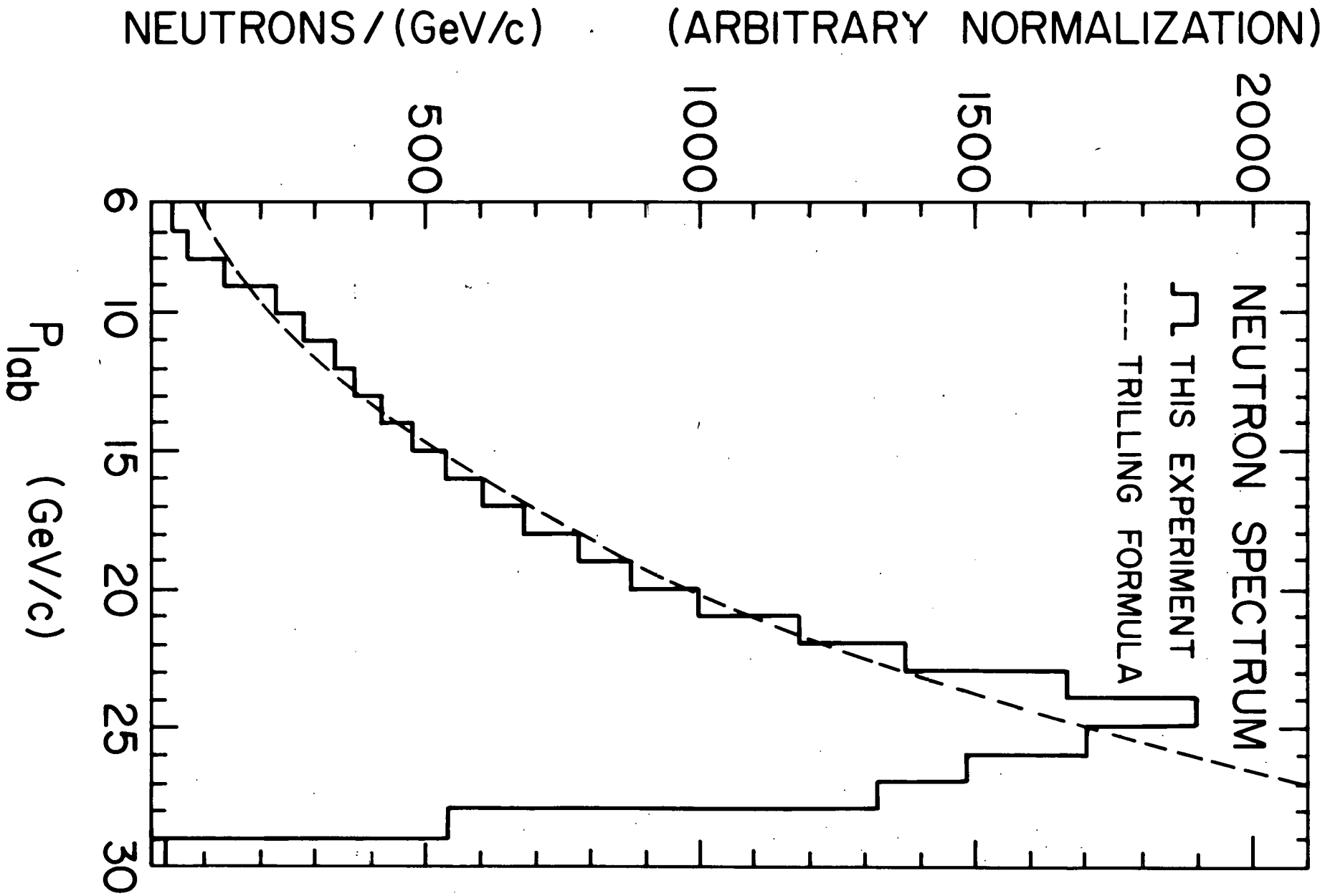


Figure D.5

REFERENCES

- (1) H. Palevsky, J. A. Moore, R. L. Stearns, H. R. Muether, R. J. Sutter, R. E. Chrien, A. P. Jain, and K. Otnes, *Physical Review Letters* 9, 509 (1962).
- (2) J. L. Friedes, H. Palevsky, R. L. Stearns, and R. J. Sutter, *Physical Review Letters* 15, 38 (1965).
- (3) G. Manning, A. G. Parham, J. D. Jafar, H. B. van der Raay, D. H. Reading, D. G. Ryan, B. D. Jones, J. Malos, and N. H. Lipman, *Nuovo Cimento* 41A, 167 (1966).
- (4) In addition to references 57, 59, and 61, see the following:
B. G. Gibbard, M. J. Longo, L. W. Jones, J. R. O'Fallon, M. N. Kreisler, and M. L. Perl, *Nuclear Physics* B30, 77 (1971);
M. L. Perl, J. Cox, M. J. Longo, and M. N. Kreisler, *Physical Review D* 1, 1857 (1970);
B. G. Gibbard, L. W. Jones, M. J. Longo, J. R. O'Fallon, J. Cox, M. L. Perl, W. T. Toner, and M. N. Kreisler, *Physical Review Letters* 24, 22 (1970);
J. Cox, M. L. Perl, M. N. Kreisler, M. J. Longo, and S. T. Powell, *Physical Review Letters* 21, 641 (1968);
J. Cox, M. L. Perl, M. N. Kreisler, and M. J. Longo, *Physical Review Letters* 21, 645 (1968);
M. N. Kreisler, L. W. Jones, M. J. Longo, and J. R. O'Fallon, *Physical Review Letters* 20, 468 (1968);
L. W. Jones, M. J. Longo, J. R. O'Fallon, and M. N. Kreisler, *Physics Letters* 27B, 328 (1968);
M. N. Kreisler, F. Martin, M. L. Perl, M. J. Longo, and S. T. Powell, *Physical Review Letters* 16, 1217 (1966).
- (5) R. Wilson, *Annals of Physics* 32, 193 (1965).
- (6) P. F. Shepard, T. J. Devlin, R. E. Mischke, and J. Solomon, *Princeton-Pennsylvania Accelerator Report No. PPAR-10* (1969).
- (7) R. E. Mischke, P. F. Shepard, and T. J. Devlin, *Physical Review Letters* 23, 542 (1969).

- (8) E. L. Miller, M. Elfield, N. W. Reay, N. R. Stanton, M. A. Abolins, M. T. Lin, and K. W. Edwards, Physical Review Letters 26, 984 (1971).
E. L. Miller, Ph.D. thesis, Ohio State University (1971).
- (9) J. Engler, K. Horn, F. Mönig, P. Schludecker, W. Schmidt-Parzefall, H. Schopper, P. Sievers, H. Ullrich, R. Hartung, K. Runge, and Yu. Galaktionov, Physics Letters 34B, 528 (1971).
- (10) G. F. Chew, Physical Review 112, 1380 (1958).
- (11) N. S. Amaglobeli and Yu. M. Kazarinov, Soviet Physics JETP 37, 1125 (1960).
- (12) R. R. Larsen, Nuovo Cimento 18, 1039 (1960).
- (13) A. Ashmore, W. H. Range, R. T. Taylor, B. M. Townes, L. Castillejo, and R. F. Peierls, Nuclear Physics 36, 258 (1962).
- (14) P. Cziffra and M. J. Moravcsik, Physical Review 116, 226 (1959).
- (15) See, for example, J. D. Bjorken and S. D. Drell, Relativistic Quantum Mechanics (McGraw-Hill, 1964).
- (16) M. Jacob and G. C. Wick, Annals of Physics 7, 404 (1959).
- (17) M. L. Goldberger, M. T. Grisaru, S. W. MacDowell, and D. Y. Wong, Physical Review 120, 2250 (1960).
- (18) I. J. Muzinich, Physical Review 130, 1571 (1963); and reference 32.
- (19) L. Bertocchi, "Theoretical Aspects of High Energy Phenomenology," Proceedings of the Heidelberg Conference on Elementary Particles (1967).
- (20) R. J. N. Phillips, Physics Letters 4, 19 (1963).
- (21) I. J. Muzinich, Physical Review Letters 11, 88 (1963).
- (22) M. M. Islam and T. W. Preist, Physical Review Letters 11, 444 (1963).
- (23) D. V. Bugg, Physics Letters 7, 365 (1963).
- (24) R. J. N. Phillips, Physical Review Letters 11, 442 (1963).
- (25) G. A. Ringland and R. J. N. Phillips, Physics Letters 12, 62 (1964).
- (26) E. M. Henley and I. J. Muzinich, Physical Review 136, B1783 (1964).
- (27) L. Durant and Y. T. Chiu, Physical Review 137, B1530 (1965);
Physical Review 139, B646 (1965).

- (28) K. Gottfried and J. D. Jackson, Nuovo Cimento 34, 735 (1964).
- (29) G. L. Kane (private communication to S. T. Powell).
- (30) B. T. Feld, Models of Elementary Particles (Blaisdell, 1969).
- (31) N. Byers and C. N. Yang, Physical Review 142, 976 (1966);
N. Byers, Physical Review 156, 1703 (1967).
- (32) R. J. N. Phillips, Nuclear Physics B2, 394 (1967).
- (33) V. D. Barger and D. B. Cline, Phenomenological Theories of
High Energy Scattering (Benjamin, 1969).
- (34) F. Arbab and J. W. Dash, Physical Review 163, 1603 (1967).
- (35) A. Ahmadzadeh, Physical Review 134, B633 (1964).
- (36) V. Flores-Maldonado, Physical Review Letters 17, 113 (1966);
Physical Review 155, 1773 (1967).
- (37) D. V. Volkov and V. N. Gribov, Soviet Physics JETP 17, 720 (1963).
- (38) For a discussion of conspiracy see references 19, 32, and 34.
- (39) J. Geicke and K. H. Mütter, Physical Review 184, 1551 (1969).
- (40) P. Finkler, Physical Review D 1, 1172 (1970).
- (41) B. K. Pal, Physical Review D 1, 1405 (1970).
- (42) M. LeBellac, Physics Letters 25B, 524 (1967).
- (43) K. Huang and I. J. Muzinich, Physical Review 164, 1726 (1967).
- (44) A. B. Kaidalov and B. M. Karnakov, Physics Letters 29B, 372 (1969).
- (45) F. Henyey, G. L. Kane, J. Pumplin, and M. H. Ross, Physical
Review 182, 1579 (1969).
- (46) M. Ross, F. S. Henyey, and G. L. Kane, Nuclear Physics B23,
269 (1970).
- (47) G. L. Kane, F. Henyey, D. R. Richards, M. Ross, and G. Williamson,
Physical Review Letters 25, 1519 (1970);
D. R. Richards, Ph.D. thesis, University of Michigan (1971).
- (48) E. Gotsman and U. Maor, Tel-Aviv University, TAUP 285-72 (1972).
- (49) S. Chia, University of Illinois, ILL-(TH)-71-13 (1971).
- (50) H. Schopper, "The Charge Exchange Reactions $np \rightarrow pn$ and $\bar{p}p \rightarrow \bar{n}n$,"
International Seminar on Binary Reactions of Hadrons at High
Energies, Dubna, June 1971.
- (51) M. Lusignoli and Y. Srivastava, University of Rome, Internal Report
No. 342 (1971).

- (52) Princeton-Pennsylvania Accelerator, Princeton, New Jersey.
- (53) Science Accessories Corporation, Southport, Connecticut.
- (54) M. Buttram, Ph.D thesis, Princeton University (1970).
- (55) Pek Labs, Inc., Sunnyvale, California.
- (56) Neutron Cross Sections, BNL 325, Supplement No. 2 (1964).
- (57) M. B. Davis, B. G. Gibbard, M. N. Kreisler, T. Dobrowolski, M. J. Longo, D. D. O'Brien, and T. Toohig, Physical Review Letters 29, 139 (1972).
- (58) R. Omnès and M. Froissart, Mandelstam Theory and Regge Poles (Benjamin, 1963).
- (59) T. P. McCorriston, Ph.D thesis, University of Michigan (1972); L. W. Jones, M. J. Longo, T. P. McCorriston, E. F. Parker, S. T. Powell, and M. N. Kreisler, Physics Letters 36B, 509 (1971).
- (60) The measured cross sections from reference 59 were extrapolated to iron.
- (61) M. J. Longo, L. W. Jones, D. D. O'Brien, J. C. VanderVelde, M. B. Davis, B. G. Gibbard, and M. N. Kreisler, Physics Letters 36B, 560 (1971); J. C. VanderVelde, L. W. Jones, M. J. Longo, D. D. O'Brien, M. B. Davis, B. G. Gibbard, and M. N. Kreisler, accepted for publication in Nuclear Physics B.
- (62) D. R. O. Morrison, Physics Letters 22, 226 (1966).
- (63) G. Cocconi, E. Lillethun, J. P. Scanlon, C. A. Stahlbrandt, C. C. Ting, J. Walters, and A. M. Wetherell, Physics Letters 8, 134 (1964).
- (64) E. W. Anderson, E. J. Bleser, G. B. Collins, T. Fujii, J. Menes, F. Turkot, R. A. Carrigan, R. M. Edelstein, N. C. Hien, T. J. McMahon, and I. Nadelhaft, Physical Review Letters 16, 855 (1966).
- (65) H. H. Bingham, CERN/D.Ph.II/PHYS/70-60 (1970).
- (66) D. R. Morrison, Physical Review 165, 1699 (1968); Physics Letters 22, 528 (1966).

- (67) "200 Bev Accelerator Design Study," Vol. 1, Section XIII-1.3, page XIII-6, Lawrence Radiation Laboratory, University of California (1965).
- (68) J. Engler, W. Flauger, B. Gibbard, F. Mönig, K. Pack, K. Runge, and H. Schopper, IV. International Conference on High Energy Collisions, Oxford, April 1972.
- (69) A. Chastel, M. B. Davis, C. M. Hoffman, M. N. Kreisler, and A. J. S. Smith, Nuclear Instruments and Methods 94, 493 (1971).
- (70) The Monte Carlo routine was supplied by Dr. R. Stanton, Physics Department, Ohio State University; adjustments were made for the properties of the liquid scintillator, M. G. Hauser (private communication).
- (71) References 64 and 66; and F. Turkot (private communication).
- (72) S. C. Curran, Luminescence and the Scintillation Counter (Butterworths Scientific Publications, London, 1953);
J. B. Birks, The Theory and Practice of Scintillation Counting (Permagon Press, 1964).